Nicolò Borghi

Developing a Target Imaging System for the European Spallation Source

Ph.D. Thesis

Risø, August 2019

DTU Nutech
Center for Nuclear Technologies

Developing a Target Imaging System for the European Spallation Source

Author
Nicolò Borghi

Supervisors
Lauritzen, Dr. Bent
Zanini, Dr. Luca

Center for Nuclear Technologies
Risø Campus
Technical University of Denmark
Frederiksborgvej 399, Building 201
DK-4000 Roskilde
Denmark

www.nutech.dtu.dk
Tel: (+45) 46 77 49 00
Fax: (+45) 45 77 49 59

To my wife.
To my dad.
To my mom.

Abstract

This PhD project is the result of a joint research collaboration between the Technical University of Denmark (DTU) and the European Spallation Source (ESS). The objective was to conduct a feasibility study for the development of a diagnostic instrument intended to monitor the ESS spallation target material over the course of its lifetime.

The ESS will be the most powerful spallation neutron source in the world. Neutrons will be extracted from 7000 tungsten bricks arranged in a grid layout and encased in a steel rotating wheel.

The ESS target technology is largely untested, hence several diagnostic instruments will continuously assess its structural and operational condition to ensure consistent neutronic performance as well as prompt response in case of failures.

The proposed Target Imaging System (TIS) is intended to perform online imaging of the inner structure of the target wheel to ensure that its geometry is preserved over the course of the expected 5 years of target lifetime.

The TIS consists of a 1D scintillator array detecting collimated decay γ radiation originating from the activated tungsten bricks. Modifications in the grid layout due to accumulation of debris or to cloven bricks will result in a localized increase of γ-ray emission. The TIS will be capable of multi-scale imaging: coarse spatial resolutions will allow fast detection of such increases, whereas the full 1 mm resolution will provide the precise (r, θ) location of the detected anomaly.

A prototype instrument has been designed, built and commissioned at DTU to investigate the basic functionalities of the proposed TIS.

Reconstructed images obtained from a specialized rotating resolution target wheel demonstrate the feasibility of the TIS principle.

The prototype development allowed to formulate design and manufacturing recommendations, to identify suitable materials for the structural and optical TIS components, to develop software for instrument control and to outline the principles for the TIS image reconstruction and anomaly detection.

This PhD project is providing a baseline for the TIS development and will provide guidelines to benchmark the forthcoming design choices.

Resumé (Danish)

Dette ph.d.-projekt er resultatet af et fælles samarbejde mellem Danmarks Tekniske Universitet (DTU) og den Europæiske Spallationskilde (ESS). Målet er at undersøge muligheden for at udvikle et dianogstisk instrument til at monitorere spallationsmålet på ESS.

ESS bliver verdens mest intense neutronspredningsfacilitet, hvor neutroner vil blive udtrukket fra 7000 wolframsten opsat i et gittersystem og indkapslet i et roterende stålhjul. En del af teknologien til ESS er generelt uprøvet og adskillige diagnostiske instrumenter vil løbende kontrollere både de strukturelle og operationelle forhold for at sikre en stabil neutronleverance og muliggøre en hurtig reaktion i tilfælde af fejl.

Systemet til at monitorere spallationsmålet (TIS) er beregnet til at give løbende billeder af den indre struktur for at sikre at geometrien er uændret i løbet af den forventede levetid på fem år. Selve TIS består af en række af endimensionelle scintillatorer, der kan detektere kollimerede γ-emissioner fra de aktiverede wolframsten: ændringer i opsætningen grundet ophopning af rester eller ødelagte sten vil resultere i en højere γ-emission. En grov rumlig opløsning muliggør en hurtig detektion af forhøjede γ-emissioner mens en måling med millimeterpræcision kan detektere hvor anomalien er.

En prototype af instrumentet er blevet designet, bygget og kommisioneret på DTU for at undersøge funktionaliteterne af TIS. Rekonstruerede billeder fra et specialkonstrueret roterende hjul dokumenterer, at TIS-designet virker.

Udviklingen af prototypen muliggør forslag til design- og fremstillingsprocessen samt at udpege relevante materialer for både de strukturelle og optiske TIS-komponenter. Ydermere blev software udviklet, der kan styre instrumenterne og i hovedtræk rekonstruere TIS-billederne og detektere anomalierne i målet.

Dette ph.d.-projekt giver således et udgangspunkt for TIS-udviklingen og et sammenligningsgrundlag for de kommende valg af design.

Acknowledgements

Over the past three years I have had the opportunity to work with a large number of experts who, in so many different ways, made this work possible.

First of all, thank you to my supervisors, Bent Lauritzen and Luca Zanini, who mentored, helped, supported and encouraged me throughout this challenging journey.

This project was made possible thanks to the commitment of the Technical University of Denmark (DTU) and the European Spallation Source (ESS). In particular, I would like to thank Eric Pitcher for supporting the earliest phase of this PhD, both scientifically and financially. A great acknowledgement is also reserved to the ESS Technical Advisory Committee (TAC) who promoted the project and gave huge boost to the experimental activities that followed thereafter.

I would like to express my gratitude to Nigel Poolton, whose tireless dedication and huge experience have been the key to our success. His contribution to this PhD project has been priceless and greatly furthered my scientific and professional growth.

Thank you also to *The Team*: scientists, engineers, technicians from DTU and ESS who made their greatest efforts to help me in every possible way. Thank you Esben, Claus, Lars, Arne, Pia, Merete, Jørgen, Søren, Finn, Per, Bo, Minqiang, Myung Ho, Mayank, Johnny and all the colleagues at the DTU Mechanical Workshop; thank you Rikard, Ulf, Jens, Reinhard, a gentle colleague who left us too early, Alan, Konstantin, Kristoffer, Yongjoong, Valentina, Günter and Mark Anthony.

My friends, either in Denmark, Sweden or Italy. They deserve a huge thank you for supporting me day after day: Alessandro, Simone, Amit, Jeppe, Martin, Claire, Ashkhen, Raju, Jakob, Jimmy and Mostafa.

And, finally, my family: my wife Caterina, my *Papà* and *Mamma*, my grandparents. Thank you for your love, endless patience and support. We have been through very rough seas, but together we managed to weather the storm.

List of Publications

Paper 1: Journal article published in *IOP Journal of Physics: Conference Series.* Proceedings of the ICANS XXII Conference (March 2017).

- N. Borghi, E. Klinkby, B. Lauritzen, E. Pitcher, N. Poolton and L. Zanini. *Development of a target imaging system for the European Spallation Source.* IOP Journal of Physics: Conf. Series 1021 (2018) 012020 DOI: 10.1088/1742-6596/1021/1/012020R.

Paper 2: Proceeding article published for the *13th International Topical Meeting on Nuclear Applications of Accelerators (AccApp'17)* (July - August 2017).

- N. Borghi, E. Klinkby, B. Lauritzen and L. Zanini. *Detection efficiency of the ESS target imaging system: Monte Carlo simulations.* Proceedings of the 13th International Topical Meeting on Nuclear Applications of Accelerators (AccApp'17) Available: http://accapp17.org/wp-content/2017/data/pdfs/162-22932.pdf.

Paper 3: Journal article submitted to *Elsevier Radiation Measurements.*

- N. Borghi, B. Lauritzen, L. Lindvold and N. Poolton. *Characterization of optical components for the ESS Target Imaging System.* Submitted to Radiation Measurements on 29th July, 2019.

List of Acronyms

AccApp	International Topical Meeting on Nuclear Applications of Accelerators
ANL	Argonne National Laboratory
BGO	Bismuth Germanium Oxide (Bismuth Germanate)
CAD	Computer-Aided Design
CH	Switzerland
CMOS	Complementary Metal-Oxide Semiconductor
CN	China
CSNS	China Spallation Neutron Source
CW	Continuous Wave
DTU	Technical University of Denmark
EDM	Electrical Discharge Machining
ESS	European Spallation Source
FOM	Figure of Merit
FOV	Field Of View
FWHM	Full Width at Half Maximum
ICANS	International Collaboration on Advanced Neutron Sources
ILL	Institut Laue-Langevin
IPNS	Intense Pulsed Neutron Source
IR	Infrared Radiation
I-sCMOS	Intensified sCMOS
ISIS	ISIS Neutron and Muon Source (RAL, UK)
ISIS-TS1	ISIS - Target Station 1
JP	Japan
KEK	High Energy Accelerator Research Organization
KENS	KEK Neutron Science Division
LANL	Los Alamos National Laboratory

LANSCE	Los Alamos Neutron Science Center
LINAC	LINear ACcelerator
LPSS	Long Pulse Spallation Source
LuAG:Ce	LUtetium Aluminum Garnet - Cerium doped
MCNPX	Monte Carlo N-Particle eXtended
MLF-NNRI	Materials and Life Science Experimental Facility - Neutron-Nucleus Reaction Instrument
MLNSC	LANSCE Manuel Lujan Jr. Neutron Scattering Center
n_TOF	neutron Time Of Flight
OECD	Organization for Economic Co-operation and Development
PEEK	Poly(aryl Ether Ether Ketone)
PMMA	Poly(Methyl MethAcrylate)
PMT	Photo-Multiplier Tube
PSI	Paul Scherrer Institut
PSNS	Pulsed Spallation Neutron Source
PWM	Pulse Width Modulation
QA	Quality Assurance
QC	Quality Control
RAL	Rutherford Appleton Laboratory
sCMOS	scientific CMOS
SDK	Software Development Kit
SE	Sweden
SINQ	Swiss Institute for Nuclear Research (Schweizerisches Institut fur Nuklearforschung Quelle)
SMA	SubMiniature connector version A
SNR	Signal-to-Noise Ratio
SNS	Spallation Neutron Source
SPECT	Single-Photon Emission Computed Tomography
SPSS	Short Pulse Spallation Source
TDR	Technical Design Report
TIS	Target Imaging System
TMP	Target Monitoring Plug
TMR	Target Moderator Reflector
TMS	Target Monitoring System
TTL	Transistor-Transistor Logic
UK	United Kingdom
US	United States of America
USA	United States of America

WNR	LANSCE Weapons Neutron Research Facility
YAG:Ce	Yttrium Aluminum Garnet - Cerium doped

Contents

CHAPTER 1

Introduction

This PhD thesis is the result of a joint research collaboration between the Technical University of Denmark (DTU) and the European Spallation Source (ESS). The objective is to conduct a feasibility study for the development of a diagnostic instrument intended to monitor the spallation target material over the course of its lifetime.

The ESS will produce neutrons by means of a new spallation target technology, a solid rotating tungsten wheel, which will be operated at the unprecedented power of 5 MW. Under this conditions, the behaviour of the spallation target material has never been studied. Although tests, simulations and calculations have been carried out at ESS to predict the likely points of failure, condition monitoring during operation is an important source of knowledge for future target developments.

The instrument proposed is intended to monitor the stability of the target during operation. Visual or other monitoring techniques are not viable options due to the target design and to the demanding operation conditions.

This PhD project started from a minimum requirement imposed by the ESS during the early design stages and was structured as follows:

1. Instrument concept definition: the imaging system is based on the detection of decay radiation originating from the activated tungsten wheel.

2. Neutronic simulations and activation calculations to support the instrument concept and study the properties of the signal to be detected.

3. Design and construction of an experimental setup to test and optimize the components and techniques for the final instrument.

4. Collection and analysis of data acquired with the prototype instrument to confirm the expected functionalities and provide a baseline for future instrument development.

The prototype operations provided successful results supporting the feasibility of the imaging system. The achieved milestones will be shared with the ESS to contribute to the final instrument design.

The structure of this thesis reflects the milestones of the project:

Chapter 2 Physics background about neutron sources and applications is provided. The ESS is presented to provide the required context for the PhD project. Attention is focused on the ESS target station, where the target and the proposed system will be located.

Chapter 3 The target imaging system proposal is discussed. Basic design details are provided and supported with Monte Carlo simulations. The operation modes envisaged for the system are described. The image reconstruction principle, from the anomaly detection perspective, is introduced. Two publications, included at the end of the chapter, have been issued describing the basic system features.

Chapter 4 Highlights of the prototype construction are discussed and the optical components are characterized and benchmarked. A publication has been issued to provide a baseline for the instrument design.

Chapter 5 The experimental results are presented and the reconstructed images from the test instrument are analyzed and discussed. Additional considerations about the instrument calibration and operation are presented.

Chapter 6 The design of the final system for the ESS should be based on the experience acquired with this project. Recommendations for such implementation and new investigations are discussed.

Chapter 7 The project outcome is summarized and an outlook on future development steps is given.

CHAPTER 2

Neutrons at the European Spallation Source

The neutron is an important tool for nuclear and material science. Immediately after its discovery in 1932, it allowed to solve the puzzling problem of the nuclear structure [1]; soon after, the possibility of using neutrons as nuclear probes became clear thanks to their magnetic moment, electrical neutrality and high penetration power [2].

Generally, neutrons either undergo absorption or scattering reactions with matter and these processes provide information about its inner structure [3]. High-energy neutrons, being neutral particles, cannot be guided or focused onto a target. Moreover, most neutron reactions only occur within a narrow energy range ($\lesssim 25$ meV). This makes scattering an intensity-limited technique, increasing the demand for intense neutron sources [4].

This chapter introduces the basic properties of neutrons. The main production reactions are mentioned and the attention is then focused on the ESS, which will become the most intense neutron source in the world.

2.1 Neutrons in science

2.1.1 Fundamental properties of the neutron

In 1930, while studying the reactions between Be and α-particles, Frédéric Joliot and Irène Curie observed a new, very penetrating radiation, even capable of freeing protons from hydrogenous materials with energies up to a few MeV [5]. In 1932, after additional observations, James Chadwick interpreted the results naming the newly discovered particle *neutron* (n) [6].

Later investigations on the fundamental properties of the neutron led to the conclusion that it is a baryon composed of three quarks (udd) and with the properties summarized in Tab. 2.1 [7].

Table 2.1: Neutron physical properties [7].

Property	**Value**
Mass	$939.565379 \pm 2.1 \times 10^{-5}$ MeV/c^2
Spin	$\frac{1}{2}\hbar$
Average lifetime	880.3 ± 1.1 s
Magnetic moment	$-1.91304272 \pm 4.5 \times 10^{-7}\ \mu_\mathrm{N}$
Electric dipole moment	$< 0.29 \times 10^{-25}\ e \cdot \mathrm{cm}$
Charge	$(-0.2 \pm 0.8) \times 10^{-21}\ e$

The neutron is the only long-lived massive particle with quasi-zero charge, hence it cannot undergo Coulomb interactions. The main drawback of the neutron's neutrality, however, is the fact that it cannot be directly accelerated neither easily guided, focused or detected. In fact, given the typically large interaction cross sections with matter for low-energy neutrons, the only available direct detection techniques are destructive measurements [8].

Despite all the difficulties it is in fact the neutron's elusiveness the key to its importance in a broad variety of applications, ranging from physical, chemical and biological sciences to nuclear medicine and material technology [9].

Neutrons, like other particles, exhibit both particle and wave properties. The corresponding de Broglie wavelength is:

$$\lambda = \frac{h}{\sqrt{2m_nE_n}} \tag{2.1}$$

where $h = 4.136 \times 10^{-21}$ MeV $\cdot$ s is the Planck constant and E_n the energy of the neutron.

Tab. 2.2 shows the classification of neutrons according to their energy and the corresponding wavelengths used in neutron experiments are also indicated [10].

The typical wavelength of thermal neutrons (25 meV) is in the Ångstrom range, thus matching the atomic distances. Hence, neutrons can serve as an excellent probe for providing information about atomic structures and dynamics, also due to the high interaction cross-sections for low-energy neutrons [10].

2.1.2 Neutron production methods

Neutrons can only exist as unbound particles for a relatively short time (15 min), then they undergo a β^- decay into a proton, an electron and an antineutrino.

Table 2.2: Neutron classification and energy spectrum [10].

Type	**Energy**	**Speed (m/s)**	**Wavelength (Å)**
ultracold	$< 0.2\ \mu\text{eV}$	< 6	> 640
very cold	$0.2\ \mu\text{eV} \leq E < 50\ \mu\text{eV}$	$6 \leq v < 100$	$40 < \lambda \leq 640$
cold	$0.05\ \text{meV} < E \leq 25\ \text{meV}$	$100 < v \leq 2200$	$1.8 \leq \lambda < 40$
thermal	25 meV	2200	1.8
epithermal	$25\ \text{meV} < E \leq 500\ \text{keV}$	$2200 < v \leq 10^7$	
fast	$> 500\ \text{keV}$	$> 10^7$	

The 15 min lifetime makes the neutron unlikely to exist as a free particle in nature, hence the need for artificial neutron sources. Terrestrial cosmic rays may in fact be considered a natural source of neutrons, but the flux is too low to be experimentally useful. Several other reactions can instead be exploited to artificially produce neutrons [3]:

i. **nuclear reactions**: they allow to separate the neutrons from nuclei in which they are particularly weakly bound. Protons, deuterons, α-particles or γ-rays are commonly chosen as projectiles and they can form excited compound nuclei. If their excitation energy is larger than the binding energy of the least-bound neutron, the neutron might be emitted. The residual excitation energy is then released in the form of γ-rays. ${}^{9}\text{Be}(\alpha, n)^{12}\text{C}$, ${}^{7}\text{Li}(d, n)^{8}\text{Be}$, ${}^{7}\text{Li}(p, n)^{7}\text{Be}$, ${}^{9}\text{Be}(\gamma, n)^{8}\text{Be}$ are some examples of nuclear reactions [11];

ii. **radioactive $(\alpha, \mathbf{n})$ sources**: combining, for example, the strong α-activity of natural radium with beryllium, it is possible to exploit the ${}^{9}\text{Be}(\alpha, n)^{12}\text{C}$ nuclear reaction to produce weak isotropic neutron sources, particularly suited for laboratory environments requiring almost point-like sources, with constant emission. These sources are usually characterized by the presence of a significant γ-ray background [11];

iii. **radioactive $(\gamma, \mathbf{n})$ sources**: these sources are capable of providing a quasi-monoenergetic neutron spectrum by means of monochromatic photons. However, it is very difficult to exploit them, since they have very small neutron yields and the γ-emitters are usually short-lived;

iv. **fission neutron sources**: although some heavy nuclei are unstable against spontaneous fission, the neutron yields are too small for experimental purposes. Artificially induced fission at nuclear reactors, instead, can provide neutron fluxes near the reactor core of the order of 10^{14} n/cm^2/s. The spectrum ranges from thermal energies up to about $5 - 7$ MeV [11];

v. **spallation neutron sources**: the term *spallation* refers to inelastic nuclear reactions occurring when energetic particles, such as protons, with energies of the order of hundreds of MeV, interact with a nucleus. The verb “to spall” means to chip with a hammer [12] and suggests that, after the high-energy projectile has interacted with the target nucleus, several products are emitted, such as protons, pions, neutrons, photons and other minor residuals [13].

2.1.2.1 The spallation reaction

Spallation is an inelastic interaction between a high-energy ($E > 120$ MeV) subatomic particle, such as p, d, n, π, μ, etc, and an atomic nucleus, referred to as *target* nucleus [13]. Unlike fission, spallation is not an exothermal process: no self-sustaining chain reactions are taking place, but a constant supply of energetic particles is required instead.

The de Broglie wavelength (see Eq. 2.1) for a $100 - 150$ MeV proton is $\lambda = (2.3 - 2.8) \times 10^{-13}$ cm: a proton hitting a target can therefore interact directly with the individual nucleons.

A schematic representation of the spallation process is shown in Fig. 2.1.

It is possible to define two stages in a spallation reaction [13]:

i. during the ***cascade/pre-equilibrium*** phase, the incident particle undergoes several direct reactions with the neutrons and protons in the target, starting the so-called *intranuclear cascade*. In this process, secondary particles, such as protons, neutrons and pions with energies ranging from about 20 MeV up to the energy of the incoming projectile are created. If the incident particle has an energy of the order of one GeV, nucleon fragmentation might occur as well and some of the produced high-energy hadrons might actually escape from the target nucleus. Low-energy ($\simeq$ MeV) particles can also be ejected during the pre-equilibrium stage, leaving the target in a highly-excited state;

ii. when this excited nucleus decays via the emission of mainly low-energy (< 20 MeV) neutrons (along with protons, α-particles, ions and other residuals), the second phase, called ***evaporation***, occurs. As a final stage, radioactive products from the evaporation phase usually decay via γ-emission. In presence of very heavy target nuclei, the evaporation process is in competition with the so-called ***high-energy fission***.

As mentioned above, high-energy hadrons can escape during the intranuclear cascade and, due to the relativistic Lorentz-boost, they are mainly emitted in the same direction as that of the incident particles. They proceed to collide with other nuclei in the target, starting a series of secondary spallation reactions, which in turn generate a larger number of neutrons. Being external to the initial nucleus, these secondary reactions are referred to as *internuclear cascade* [13].

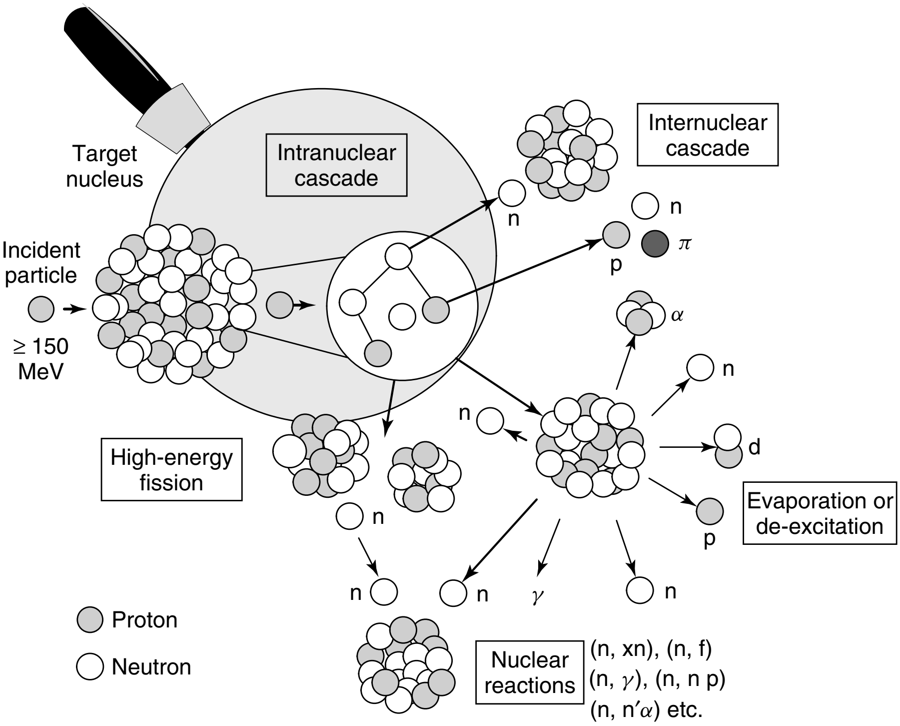

Figure 2.1: Schematics of the spallation process [13].

A more detailed scheme of the spallation process is presented in fig. 2.2: important information is provided about the sequence of the particle production stages. The intranuclear cascade, occurring within 10^{-22} s, is four orders of magnitude faster than the evaporation process, which takes place about 10^{-18} s after the initial reaction [13].

At this stage, fission and spallation might appear as similar processes: in both reactions, heavy nuclei are split to form lighter fragments and neutrons, and energy is released in each interaction. However, fission and spallation are deeply different in several aspects:

i. **nuclear debris**: in spallation, after the evaporation phase, the nuclei are about 15 a.m.u. lighter than the original target nucleus and do not exhibit the usual double-peaked mass distribution of fission products. Hence, the so-called *spallation residuals* have a mass distributed close to that of the target material. High-energy fission, though, is a competing process with standard evaporation. Fission occurring at high energies results in a symmetric distribution of the products. Therefore, the overall mass distribution,

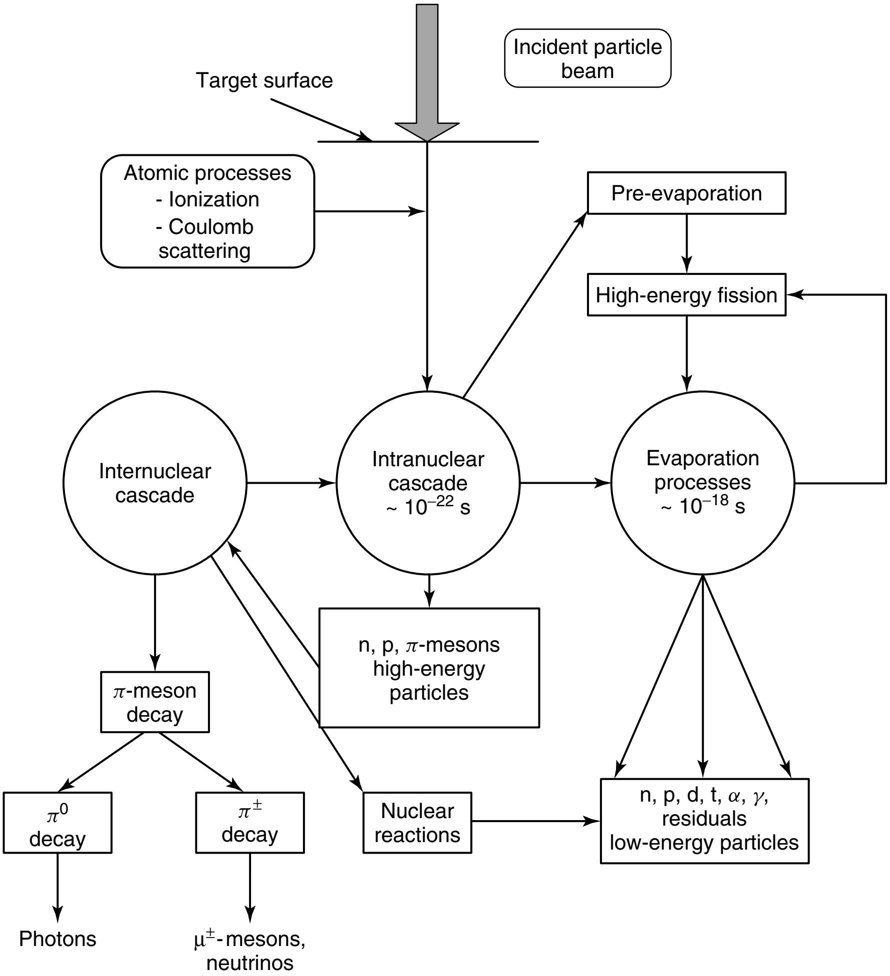

Figure 2.2: Logical scheme of the spallation reaction showing the stages of particle production [13].

presented in Fig. 2.3 for a Pb target, shows a broad peak at about $A = 90$, due to the high-energy fission, and a large abundance of spallation products for atomic masses up to the original $A = 208$ of Pb [13];

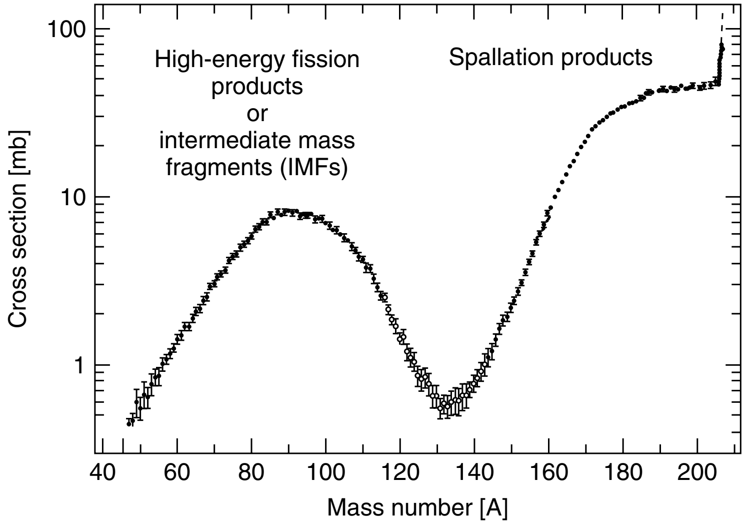

Figure 2.3: Spallation residual mass distribution for a 1 GeV $^{208}\mathrm{Pb} + \mathrm{p}$ reaction [13].

ii. **energy deposit per neutron**: a fission event produces approximately 200 MeV of energy, in the form of neutron and fragments kinetic energy, β-radiation, γ-rays, all of which appearing as heat in the reactor, and neutrino energy, which escapes. Conversely, spallation deposits a much smaller energy per neutron and, depending on the target material, it ranges from 30 to about 60 MeV. However, even though the energy per neutron generated by the spallation process is small, about 60% of the incident beam energy appears as heat in the target and this leads to serious cooling problems in the target systems [14];

iii. **neutron energy and angular distributions**: similarly to fission, the neutrons produced by spallation come from the evaporation phase of the fragments and have typical energies of about 2 MeV, as for fission neutrons. However, a small fraction of the produced neutrons emerge directly from *billiard-ball*-like collisions, therefore they have energies up to several hundreds MeV. As shown in Fig. 2.4, the spallation spectrum presents a high-energy tail reaching the GeV region, i.e. the typical incoming proton energy [13]. Besides the energy distribution, also the angular distribution of the neutrons shows an energy-dependent behaviour. Indeed, as Fig. 2.5 suggests, for high-energy neutrons, the emission is clearly peaked around the incident directions (within 0 to 15 deg): at 1 GeV, forward emitted neutrons are three orders of magnitude more abundant than neutrons emitted between 60 and 90 deg [14].

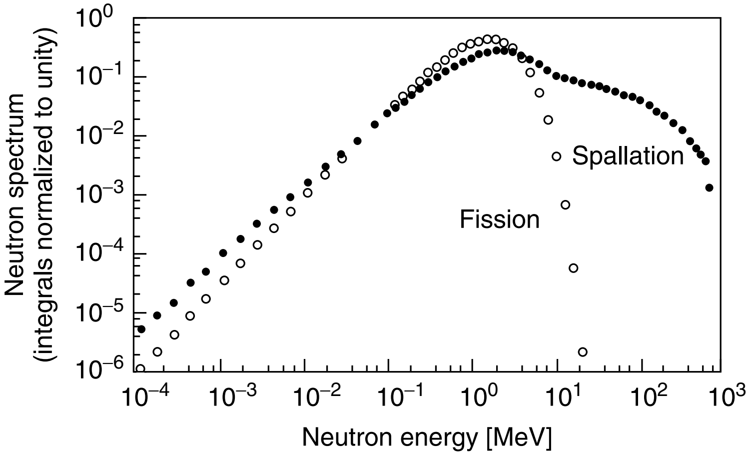

Figure 2.4: Spallation neutron spectrum compared to a typical neutron spectrum from the thermal fission of ^{235}U [13].

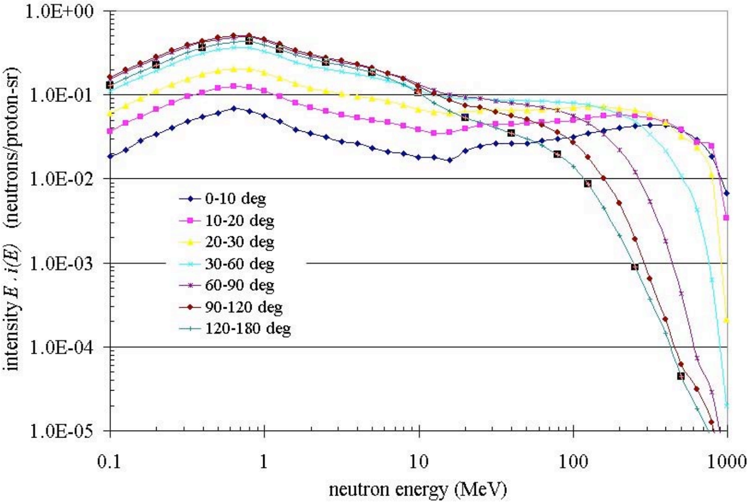

Figure 2.5: Energy distributions of spallation neutrons at different emission angles (1 GeV protons on a tantalum target) [14].

Lastly, it must be noted that the neutron yield of a spallation reaction does not only depend on the atomic mass number of the target, as it is for fission. Indeed, as Eq. 2.2 shows, the neutron yield Y is approximately a linear function of both the atomic mass A and the incident energy E [14]:

$$Y(E, A) = \begin{cases} 0.1(E_{\mathrm{GeV}} - 0.120)(A + 20) \\ 50(E_{\mathrm{GeV}} - 0.120) \end{cases} \tag{2.2}$$

The first expression of Eq. (2.2) holds for non-fissionable materials, whereas the second formula is valid for ^{238}U. A yield proportional to the incident proton energy implies a constant neutron production rate per unit time and average proton beam power [14].

In the following sections, an in-depth review of today spallation sources will be presented, with particular focus on the existing diagnostic systems. Accident cases will be shortly discussed. Attention will then be focused on the European Spallation Source, to provide the context to this PhD research work.

2.1.3 Spallation neutron sources

For about 30 years, until the late 1970s, fission-based reactors have played a dominant role as sources of neutrons (see Fig. 2.6). However, with the advent of the high-flux reactor at Institut Laue-Langevin (ILL) in Grenoble, the time averaged neutron flux achievable reached the point of saturation; the technological difficulties of dissipating heat loads of about 200 MeV per useful neutron together with the shortening of the reactor cores' lifetimes for the high power densities made reactors an unviable approach for neutron sources of the future [13].

Spallation as a source of neutrons, with an average deposit of about 30 MeV per neutron, is now the standard solution in neutron research since the late 1970s.

A first classification of spallation sources is based on the time characteristics of their operation:

i. **continuous sources**, which are fed directly from accelerators with no macro-time structure, such as cyclotrons or Continuous Wave (CW) linear accelerators (LINACs). The goal of these sources is to produce a large average neutron flux, thus low-absorption materials should be used in the target station to reduce the capture of moderated neutrons and obtain a large thermal flux. The only existing continuous source is the 1 MW SINQ spallation source at Paul Scherrer Institut (PSI), Switzerland [13];

ii. **pulsed sources** (PSNS), which are characterized by non-continuous neutron emission. The primary particles impinge on the target at regular intervals, with a repetition rate varying between 10 and 60 Hz and a duty-cycle of a few percent. Unlike continuous sources, where an increase in the neutron flux requires an overall increase of the steady-state neutron emission, pulsed sources are designed to deliver large fluxes for a limited time, thus reducing

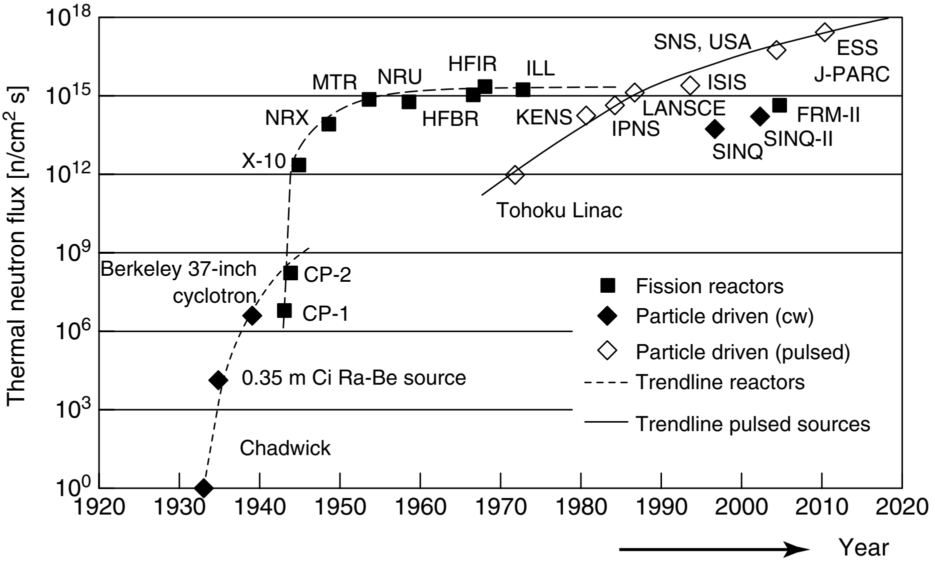

Figure 2.6: Evolution of the thermal neutron flux for reactor- and spallation-based sources [13].

the overall impact on the components of the entire target station [13]. The neutron spectrum from the moderator is characterized by a Maxwellian energy distribution. The main advantage of pulsed over CW sources is the ability to avoid overlapping of multiple Maxwellian distributions, thus increasing the extraction efficiency. Energy selection in CW sources can only be achieved by mechanical neutron choppers, which only allow a small fraction of the produced neutrons to reach the instruments without being discarded [3]. In pulsed sources, up to the entire white spectrum produced by a single pulse can instead be exploited, as the neutron energies reach the instruments well ordered. As shown in Fig. 2.7, it is possible to clearly define an initial (final) time at which the neutrons with the highest (lowest) energy reach the instrument [15, 16].

Depending on the time structure of the primary particle beam, two types of PSNS can be defined (Fig. 2.8):

a) **Short-pulse spallation neutron sources (SPSS)** can generate short neutron pulses, with a large neutron peak flux and a short pulse duration (FWHM $\approx$ 100 μs). The optimization criterion for these sources is the pulse length with small losses in the peak intensity. SPSS are usually fed by a compressor ring, in which a LINAC stores the primary particles until the desired current is reached and a high-density bunch

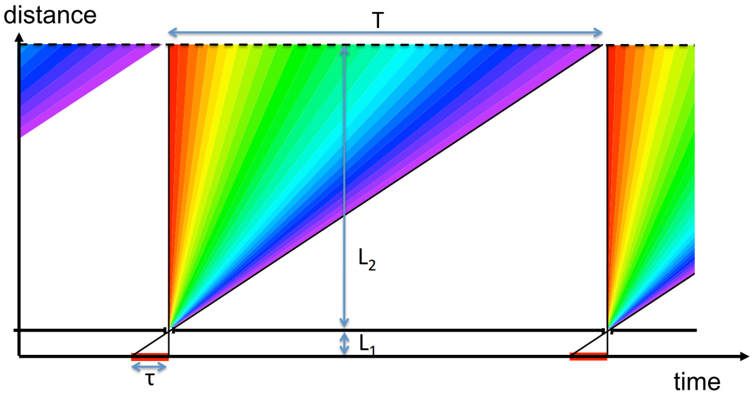

Figure 2.7: Time-distance diagram for white-beam instruments at a pulsed spallation source (τ is the source pulse width and T the repetition period). The separation between two consecutive pulses allows to define an initial (final) time at which the neutrons with the highest (lowest) energy reach the instrument. L_1 is the distance from source to the pulse-shaping chopper; L_2 is the distance from chopper to instrument [16].

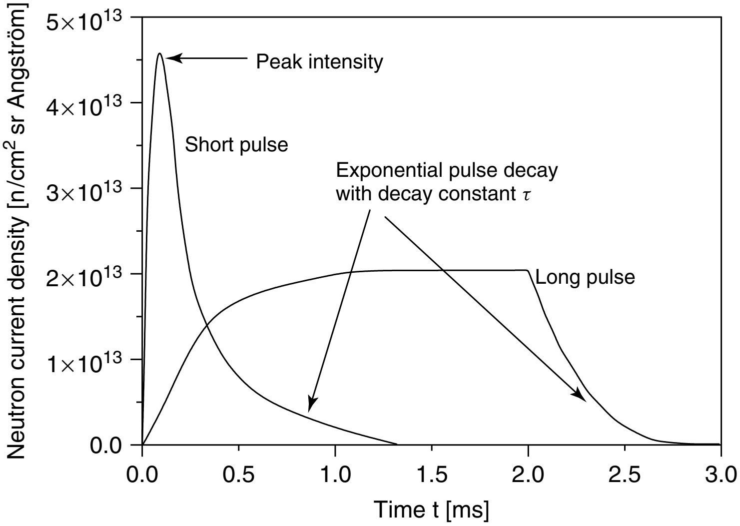

Figure 2.8: Typical pulse shapes of SPSS and LPSS target stations [13].

of particles is formed. Then these particles are quickly extracted and directed towards the target. Rapid cycling synchrotrons can be employed instead of compressor rings [13]. Typical pulse lengths are of the order of μs or smaller and the pulse width presented in Fig. 2.8 is determined by the neutron thermalization time [17].

b) **Long-pulse spallation neutron sources (LPSS)** are capable of providing a high-intensity time averaged neutron flux, with a flat top pulse shape, as shown in Fig. 2.8 [13]. The pulse length, in this case of the order of a few ms, is determined directly by the duty cycle of the primary beam. When no beam is impinging on the target, i.e. no spallation reactions are occurring, the pulse shows an exponential decay, whose characteristic time τ depends directly on the neutron lifetime inside the target station, especially in the moderator [17]. A fundamental advantage of LPSS over SPSS is the capability of the former to provide any desired pulse length for a specific optimization of any individual experiment [15]. Moreover, for scattering experiments, LPSS can provide time-integrated fluxes larger by a factor 2 or 3 than SPSS with smaller repetition rates. This fact, together with the absence of a high-intensity short peak, significantly reduces the mechanical stresses suffered by the target due to the intense pressure waves [18]. From a theoretical point of view, however, LPSS can be treated as SPSS and the obtained results can then be convoluted with the desired LPSS pulse duration [17].

Among the first spallation sources, it is worth mentioning KENS (KEK, Japan), IPNS (ANL, USA), TRIUMF (Canada), WNR and LANSCE (LANL, USA) [13]. In Tab. 2.3, an overview of the key parameters of some neutron facilities is given; some of them are operating, whereas others, like the ESS, are still under construction [19].

Table 2.3: Operating parameters of some neutron sources [19].

Facility	**Location**	**Beam particle**	**Energy (MeV)**	**Target material**	**Pulse width (ns)**	**Beam power (kW)**	**Rep. rate (Hz)**
LANSCE-MLNSC	Los Alamos, US	p	800	W	135	800	20
LANSCE-WNR	Los Alamos, US	p	800	W	0.2	1.44	13900
n_TOF	Geneva, CH	p	20000	Pb	6	10	0.4
MLF-NNRI	Tokai, JP	p	3000	Hg	1000	1000	25
SINQ	Villigen, CH	p	590	Pb	Cont.	1000	CW
SNS	Oak Ridge, US	p	1000	Hg	700	1400	60
ISIS-TS1	Oxfordshire, UK	p	800	W	100	240	50
CSNS	Dongguan, CN	p	1600	W		100	25
ESS	Lund, SE	p	2000	W	2860	5000	14

2.2 The European Spallation Source (ESS)

The ESS will be a slow neutron source of unprecedented and unparalleled power and scientific performance. The first protons are expected to be delivered to the target in 2022, thus producing the first neutron beams necessary to feed the initial neutron scattering instruments. The full operation regime is instead planned for 2025, when the suite of 16 experimental stations will be completed [16].

2.2.1 The role of the ESS

The independent research conducted by Shull, Wollan, Brockhouse and River showed how neutrons allow to produce indirect images of molecular structures. This paved the way for the application of neutrons to material science. It wasn't too long before the first neutrons for imaging were produced in 1971 at ILL, giving birth to the European community of neutron scientists [20].

Neutrons enable to retrieve information on structural patterns down to 10^{-10} m scales and on dynamic events down to 10^{-12} s scales. Their neutral nature and the opposite attenuation/transmission behaviour with respect to photons, make neutron radiography the natural complement for conventional X-ray-based techniques [21].

Neutrons have a magnetic moment and represent an invaluable instrument for studies on magnetism. If their interactions with matter are opposite to the photons', neutrons share with them the same optical behaviour: all the scattering interactions can be calculated exactly, allowing advanced studies in quantum mechanics [21].

As indicated in Fig. 2.6, several sources exist and have been operational for years [22, 23]. The ESS will outperform all its predecessors with an unprecedented neutron intensity available to the instrument suite. However, the ESS will be the first source of its kind, with the ~ 3 ms long proton pulse. This makes the ESS its own prototype and workbench for its own development.

The ESS mission to provide the best resolution and the highest intensity possible will allow to exploit the neutron opportunities for the high-profile fundamental and applied research currently driving the industrial and scientific evolution of society [21].

2.2.2 ESS historical milestones

The interest in building a megawatt-class spallation neutron source in Europe started in 1998, when the OECD research ministers recommended that such a powerful facility be built in each of the three developed regions of the world. In 2003, this initial decision became the concrete concept of the ESS, comprising a 5 MW proton linear accelerator delivering a $2-3$ ms-long pulses to a single target station, surrounded by a suite of 20 to 25 neutron instruments. After a competitive process, Lund (Southern Sweden) was chosen in 2009 as the final location for the ESS construction and, in 2013, the facility entered the construction phase (the layout of the ESS site is shown in Fig. 2.9). Currently, the ESS Steering Committee includes more than 17 European countries which participate to the ESS project both through financial and in-kind (materials, equipment and scientists) contributions [16].

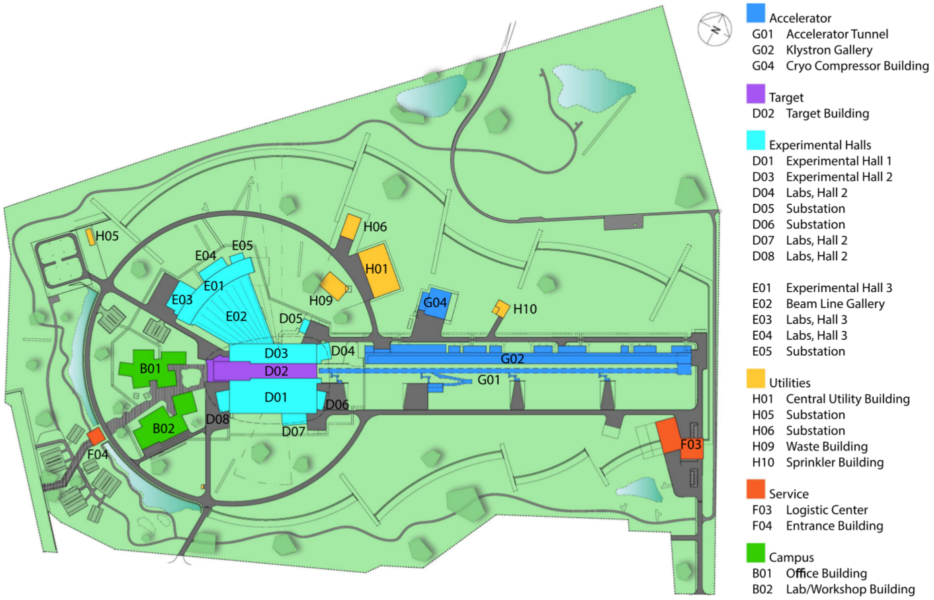

Figure 2.9: Layout of the ESS research facility [24].

2.2.3 The linear accelerator

The ESS is an accelerator-driven spallation source and it will be equipped with a 600 m-long linear accelerator, whose block diagram is shown in Fig. 2.10.

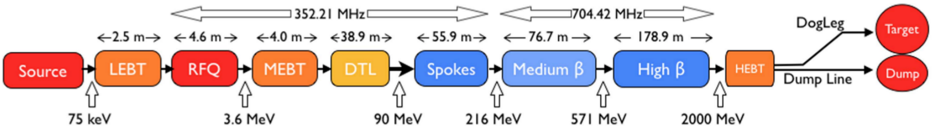

Figure 2.10: Block diagram of the ESS linear accelerator. The orange items are normal conducting, whereas the blue ones are superconducting [24].

Protons have been chosen as the primary particles for the ESS and the LINAC will accelerate them to an energy of 2 GeV, which is considered a cost-effective solution.

The ESS will operate as a LPSS neutron source, with a 2.86 ms pulse duration and a 14 Hz repetition rate. It will therefore exhibit a pulse shape similar to the one relative to long pulse sources shown in Fig. 2.8. The proton beam current will be 2.5 mA, which, given the final proton energy of 2 GeV, results in an average power delivered to the target of 5 MW. The proton beam will be characterized by a quasi-rectangular profile and the viewed target area on which the beam impinges will be covered with a rastering technique [24].

2.2.4 The target station

Despite the complexity of a spallation neutron source, for the scope of this PhD work, it is appropriate to identify it with the *target station*, where the neutron production takes place. The target station is composed of four blocks:

i. the **primary beam**: to produce neutrons, incident particles must undergo nuclear collisions before they reach the end of their range within the target material. The probability for such reactions is [17]:

$$P_n = 1 - \exp\left(-\frac{R}{\lambda}\right) \tag{2.3}$$

where R is the particle range expressed in g/cm^2 and λ the nuclear collision mean free path. To maximize the efficiency, $P_n \geq 0.95$, which implies $R > 3\lambda$ ($\lambda = 33\text{A}^3$ for $E_p \geq 100$ MeV). According to Fig. 2.11, deuterons may provide the best neutron yield, but they require additional costs and efforts in the acceleration process [13]. Therefore, protons are the favored primary particle for the ESS.

As shown in Fig. 2.12, P_n saturates for energies of the order of a few GeV, hence the choice of a 2 GeV proton beam for the ESS.

ii. a high-Z ***target***, where the spallation process takes place. The main criterion to classify a target material is its neutron yield (see Eq. 2.2). Then, engineering constraints must be fulfilled, such as the ability to withstand MW-class beam powers, a high thermal conductivity to allow cooling and a good resistance to mechanical stresses [13, 25]. Fig. 2.13 shows a comparison of several potential target materials in terms of neutron yield as a function of proton energy [17]. As it will be discussed later, despite the good performance of uranium and the cooling advantages of liquid targets, tungsten has been chosen at the ESS due to its high density, ensuring larger peak intensities in the neutron flux.

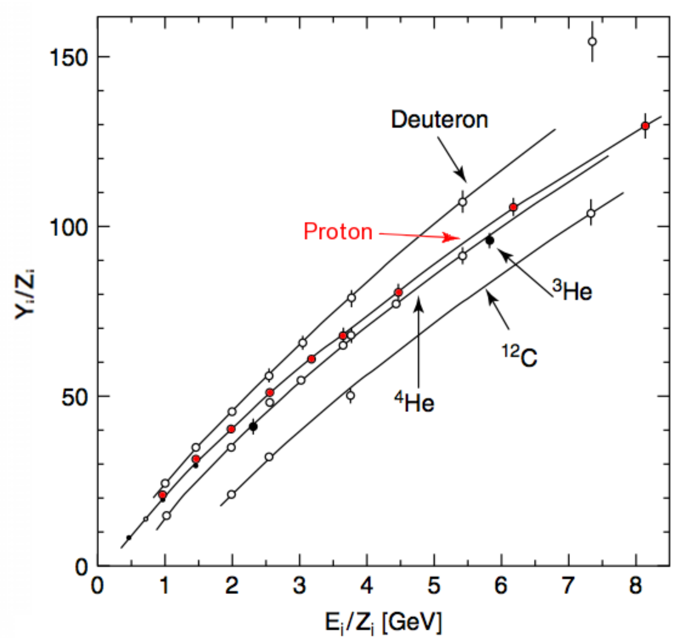

Figure 2.11: Measured neutron yield per charge, Y_i/Z_i, from a Pb target, bombarded by several light ions as a function of the incident ion energy per ion charge, E_i/Z_i [13].

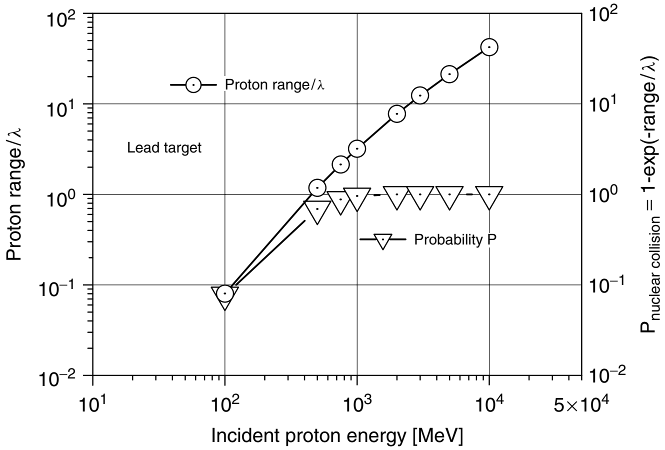

Figure 2.12: Range and interaction probability as a function of the incident proton energy [13].

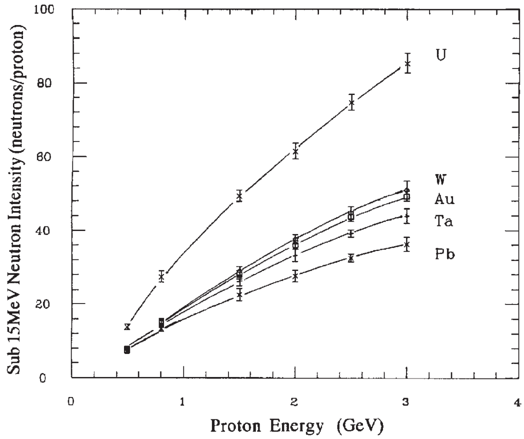

Figure 2.13: Calculated values of the total neutron intensity as a function of the proton energy for different target materials [17].

iii. the **moderator**, **premoderator** and **reflector** assembly. Fast neutrons leaking from the target enter a volume of hydrogenous material to undergo *moderation* and reach thermal or cold energies. The ESS will feature a so-called *butterfly* moderator, a quasi-two-dimensional volume (Fig. 2.14(a)) capable of providing a bi-spectral (thermal and cold) neutron beam to all the experimental beam ports [26]. The thermal volume, containing light water, is physically separated from the cold moderator, filled with 20 K pure para-hydrogen [26].

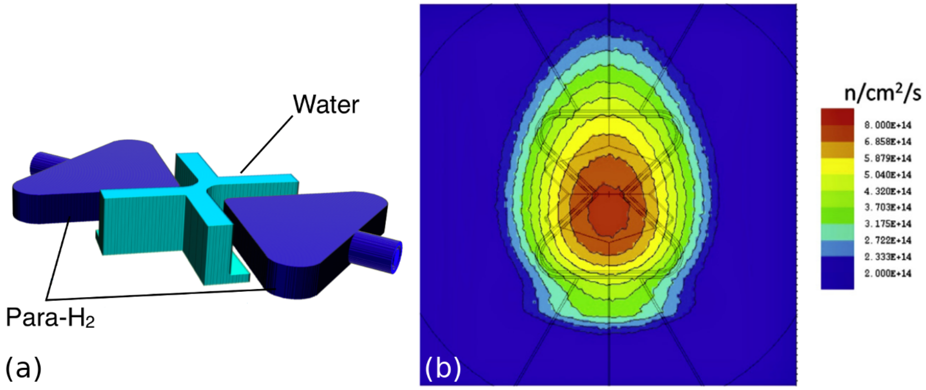

Figure 2.14: The ESS butterfly moderator: (a) three dimensional representation (ver. 2) [27]; (b) moderator coupling to the neutron hotspot [26].

As shown in Fig. 2.14(b), due to the high density of the tungsten in the target, the hotspot of neutron production (mainly evaporation neutrons) is relatively small ($\sim 15 \times 20$ cm^2) and the moderator will be precisely coupled to it [26].

The moderator will be surrounded by an intermediate volume filled with light water, the *premoderator*, with the purpose of increasing the moderator's efficiency. The target and the premoderator will be surrounded by a Be volume, the *reflector*, intended to bounce leaking un-moderated neutrons back into the moderator to further enhance the thermal and cold fluxes (Fig. 2.15).

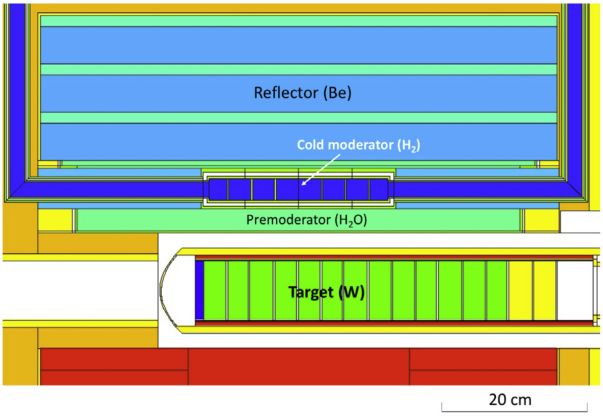

Figure 2.15: Schematic representation of the Target Moderator Reflector (TMR) assembly [26].

iv. the entire TMR unit will be finally encased in a large shielding monolith. The monolith will contain technical instrumentation, including several diagnostic systems that will be outlined in the following sections. Among these, the instrument proposed with this PhD project will monitor the health condition of the target during its expected lifetime.

2.2.4.1 The ESS rotating target

As anticipated, the ESS will produce neutrons by means of 2 GeV protons (2.5 mA, 125 MW peak and 5 MW average power) impinging on a solid tungsten target. The ESS will be the first high-power accelerator driven LPSS, with a 2.86 ms long pulse at 14 Hz repetition rate [26].

To achieve the unprecedented power of the ESS, new technological challenges had to be faced, starting from the design of the target. Provided that tungsten is the most suitable material for a spallation target, the solution adopted for coping with the high power of the beam is a He-cooled rotating wheel. As shown in Fig. 2.16(a), the wheel will be suspended on a 6 m long shaft, completely surrounded by shielding; the positioning of the TMR assembly with respect to the wheel is presented in Fig. 2.16(b)

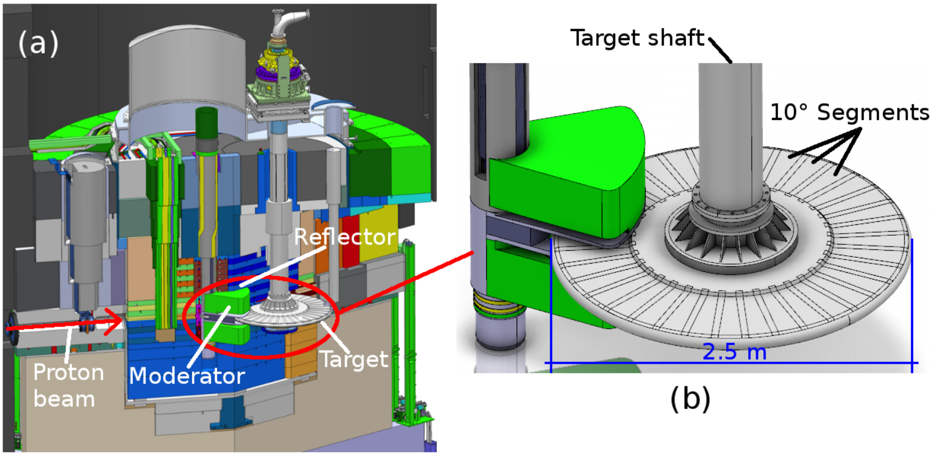

Figure 2.16: ESS target station: (a) cross-section of the ESS target monolith; (b) detail of the target-moderator relative coupling [28].

The ESS target will be a 2.5 m diameter wheel, subdivided into 36 sectors (10° each) encompassing each a total of about 180 $1 \times 3 \times 8$ cm^3 tungsten bricks (Fig. 2.17).

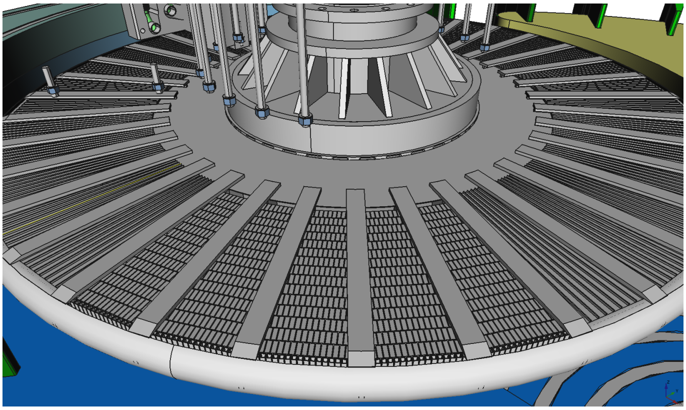

Figure 2.17: Detail of the ESS target internal structure. The segments are encased in a steel shroud to contain the cooling helium. In the five sectors in the foreground, the shroud has been hidden to show the brick layout [27].

The ESS target will be helium cooled and the grid layout of the bricks with 2 mm gaps (Fig. 2.18(a)) will expose the largest possible surface of the tungsten to enhance the heat removal. The helium will flow as shown in Fig. 2.18(b) and it be supplied to and removed from the target via the target shaft [29, 30]. The coolant to tungsten fraction (only 75% in the approved target design) has been subject to studies to ensure an adequate filling fraction of the target [31].

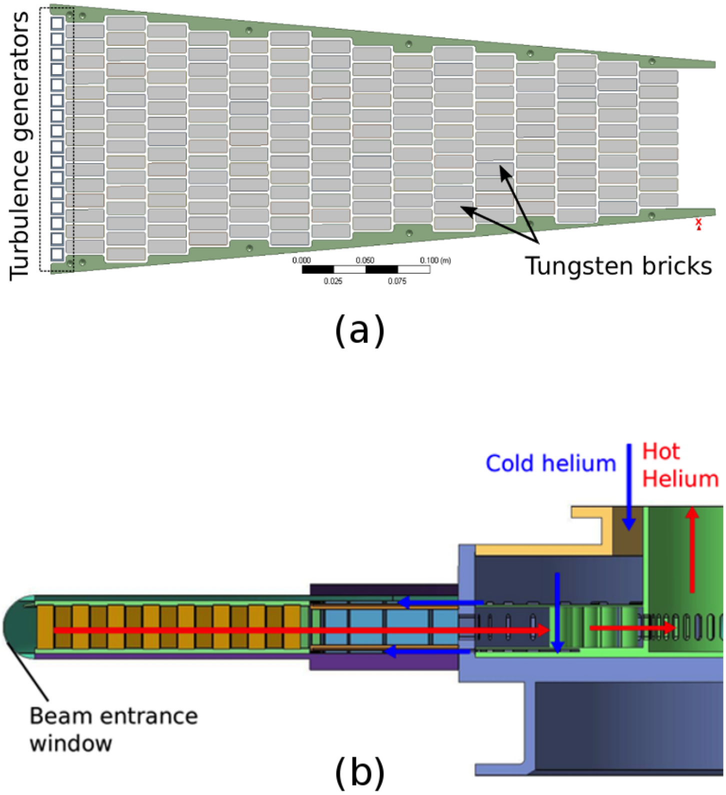

Figure 2.18: Detail of the ESS target internal structure. The grid layout of the tungsten bricks is shown in (a); the schematic representation of the cooling helium flow is given in (b). [27].

The beam-target interaction is such that each angular segment will be hit only once per revolution and this sets the wheel rotation period:

- repetition rate: 14 Hz;
- sector-to-sector transition time: 71.4 ms;
- rotation period: 71.4 ms × 36 = 2.57 s.

The adoption of a rotating target is intended to achieve a uniform heat deposit distribution over the target volume and to give time to the helium flow to remove the residual heat [30]. Moreover, the exposed surface area of the tungsten together with the stagnant helium heat conductivity should be sufficient to ensure proper passive cooling even in the event of an accidental loss of the active cooling systems [29]. As shown in Fig. 2.18(a), in order to ensure proper cooling at the edge of the wheel, where the incoming helium reverts its flow direction into the narrow grid, square blocks have been inserted as turbulence generators [30].

CHAPTER 3

Developing a target imaging system

3.1 The need for a Target Imaging System

The rotating ESS spallation target will be unique and no operating experience with such a technology is available yet. Target cooling, material resistance to high-power-induced stresses, lifetime of target materials, degradation of tungsten's mechanical and thermal properties; these represent only a few of the technological challenges that have been undertaken at the ESS.

Apart from the simulations and the experimental investigations supporting the effectiveness of the rotating target design, a lot of effort has been devoted to the study of failure events. A clear understanding of this is crucial in terms of maintenance planning, early accident identification and prevention and, more importantly, in terms of safety of the ESS operations, for the personnel as well as for the environment.

3.1.1 Examples of spallation target failures

"On June 2016, the facility was shut down because of an unexpected target failure", states an internal PSI report [32].

"Experience with uranium targets is very poor: in IPNS as well as in ISIS they failed after less than 250 mAh loading", reports Bauer in [33, 34].

These are just two examples of unplanned failures of existing spallation targets. The current background regarding material failures suggests that uranium targets tend to undergo grain growth. This usually leads to cracking in the cladding, which causes release of fission products.

Studies have been conducted on the behaviour of tantalum in the case of water cooled targets [35]. This study is intended to support the design of the China Spallation Neutron Source (CSNS) tungsten target [36]. Tungsten is indeed susceptible to corrosion in water and to oxidation when exposed to air at high temperatures [35]. This may lead to material fragmentation and to several issues in terms of loss of neutronic performance together with damages to cooling systems.

At SINQ, several accidents took place highlighting the potential failures of steel if irradiated with improper beam focusing. Another major concern is the production of hydrogen by the spallation process. Hydrogen can increase the risk of explosions and can cause embrittlement of solid targets [37].

As a general design guideline, a good target material should exhibit [33]:

- good thermal conductivity in the operational temperature range;
- small thermal expansion to minimize fatigue stresses;
- good elastic properties and ductility even under irradiation;
- low residual heat production to allow prompt emergency stops;
- resistance to corrosion;
- good manufacturability and good integration capabilities with other materials.

Liquid targets could easily meet several of these requirements since they can be targets and coolants at the same time. Experience, though, showed that the point of failure in this case would be the containment vessel. For mercury targets, for instance, the intense power of the proton beams induce strong pressure waves in the liquid. These, in turn, cause cavitation damage to the vessel compromising the lifetime [38]. Studies are addressing this issue in order to minimize the cavitation [39, 40].

From the above considerations, it is important to try to minimize and prevent the occurrence of failures; it is also of primary importance the availability of diagnostic systems capable of detecting failures and damages. Indeed, in case of normal operation, diagnostic systems can support the delivery of constant performance, whereas in the event of an accident they can provide knowledge of the conditions prior to the failure and information about the causes of failure. This can further the understanding of the behaviour of the material as well as help the early recognition of imminent failures' symptoms.

3.1.2 Target failures and accident cases at the ESS

Among the design efforts for the ESS solid tungsten target, several scenarios have been considered.

Many studies dating back to the 1960s are available on tungsten properties for fusion applications ([41–49] are only a few of the most recent ones).

The requirements for the ESS, however, are different from the requirements of a fusion reactor and the supplier selection procedure was driven by the following criteria [50]:

- integrity under thermomechanical cycles without static or fatigue failure for temperatures between room temperature and 400 °C (110 MPa max);
- resistance to erosion and oxidation in helium atmosphere with an oxygen content smaller than 10 ppm. The tungsten should also tolerate the presence of debris in the helium flow;
- resistance to proton and neutron radiation damage.

Several samples performed sufficiently well, but one important detail to stress is that the repetition of the tests showed a large dispersion of the average values: brittle fractures, the main failure mechanism observed, are stochastic events and an accurate prediction of their occurrence is not possible. This suggests that, despite strict requirements being imposed to the tungsten suppliers, the actual behaviour of the 7000 bricks of the ESS target will be subject to a large variability [50].

Integrity studies on the ESS spallation material are described in the ESS internal reports [51, 52]. The conclusions reached are the following:

- tungsten is chosen for the high mass density;
- pure tungsten is preferred over tungsten-tantalum based alloys due to its better residual ductility after irradiation with corresponding lowest induced microstructural disintegrations [53];
- rolled tungsten will be preferred for superior mechanical strength to other manufacturing techniques;
- oxidation calculations of the bricks' surface recommend to keep the tungsten temperature below 700 °C;
- temperatures below 700 °C will also minimize the risk of hydrogen explosions;
- the metallurgic structure of the chosen tungsten leads to the release of tungsten dust. The size of the grains will be larger than 10 μm reducing the risks linked to the flammable tungsten powders;
- thermal cycles induced by the beam pulses may induce surface cracks and, over time, expand them to the point of brick breaking. No data is yet available on the behaviour of the proton-induced embrittlement of the tungsten.

The formation of cracks and the possibility of brick fractures is of course one big concern, especially considering the fact that the helium cooling relies on a narrow grid (only 2 mm wide spacings) between the bricks to flow.

Another important investigation has been carried out to determine the amount of tungsten dust production. In the ESS Technical Design Report (TDR) issued in 2013, it is stated that the tungsten target will be prone to ablation and dust formation initiated by the flowing helium [16]. The preliminary study concluded that, despite the expectations, a larger contribution to the dust production may come from the steel structure encasing the target wheel, rather than from the tungsten itself [52].

Accident case evaluation, though, does not only involve the tungsten bricks. Several other points of failure have been identified and are summarized in the following list [54]:

- beam synchronization;
- wheel over- and under-speed;
- loss of focusing and/or rastering in the beam optics;
- damage to the target vessel;
- loss of cooling (pressure drop, decrease in flow, etc.);
- blockage of cooling channels due to touching bricks.

3.1.2.1 Diagnostic instruments planned for the ESS

Several diagnostic instruments have been developed in order to monitor the fundamental parameters and to ensure prompt reaction to the possible accidents. These instruments, forming the Target Monitoring System (TMS), are housed in a dedicated plug within the monolith called the Target Monitoring Plug (TMP), as shown in Fig. 3.1.

According to the specified requirements for the TMS, the purposes of the instruments within the TMP are:

i. determine the wheel position relative to the target monolith to detect collisions and misalignments;

ii. monitor the temperature of the steel shroud and of the helium outlet;

iii. perform imaging of tungsten bricks for the assessment of the target's structural integrity;

iv. measure the temperature of the TMP material.

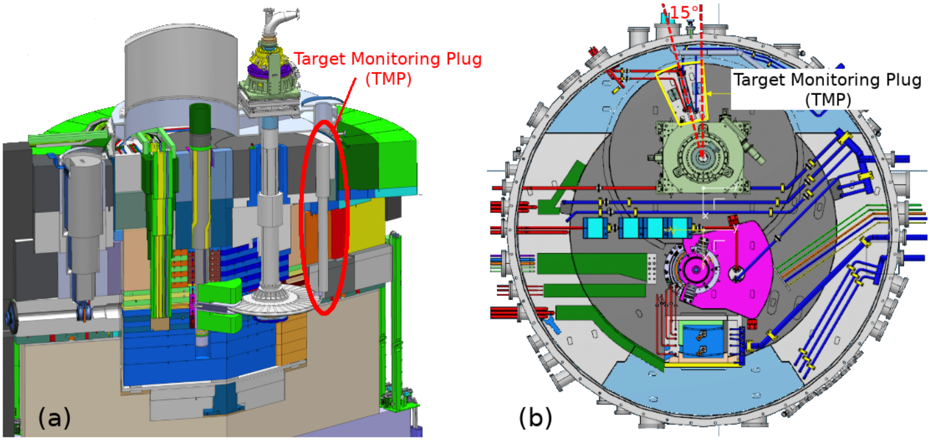

Figure 3.1: ESS target station and TMP: (a) three-dimensional view of the TMP placement within the monolith; (b) top view showing the orientation of the TMP with respect to the proton beam axis [55].

The main objective of this PhD project is to perform a feasibility study for the Target Imaging System (TIS), corresponding to point (iii) on the list. The TIS is intended to provide information on the structural integrity of the tungsten bricks inside the target wheel. It will also detect localized geometry modification resulting from the displacement of tungsten bricks; this type of failure can lead to the blocking of the inter-bricks cooling gaps, thus affecting the coolability of the target. The entire wheel is encased in a steel shroud, therefore no visual inspection of the bricks can be conducted. The TIS will be based on the detection of the γ-rays emitted by the bricks themselves, as a result of the radioactive decays occurring in the irradiated tungsten.

Before focusing the attention on the TIS, a brief overview of the TMP instrumentation will be given. In Fig. 3.2(a) the relative positioning of the TMP with respect to the target wheel and shaft is shown. The whole TMP assembly is oriented 15° away from the direction of the incident proton beam and, as shown in more detail in Fig. 3.2(b), it is a complex structure containing several diagnostic instruments, the TIS being the one in the center of the plug.

In Fig. 3.2(c) a transparency of the various components is presented:

1. the four purple cylinders are the optical heads of the x/y measurement system. Its purpose is to measure the tilting of the wheel shaft to confirm its correct alignment. A small tilt in the shaft may result in a larger displacement of the wheel, potentially leading to a collision within the monolith. The measurement is done with confocal chromatic sensors: a white light is cast onto the point whose distance is to be measured and, from the wave-

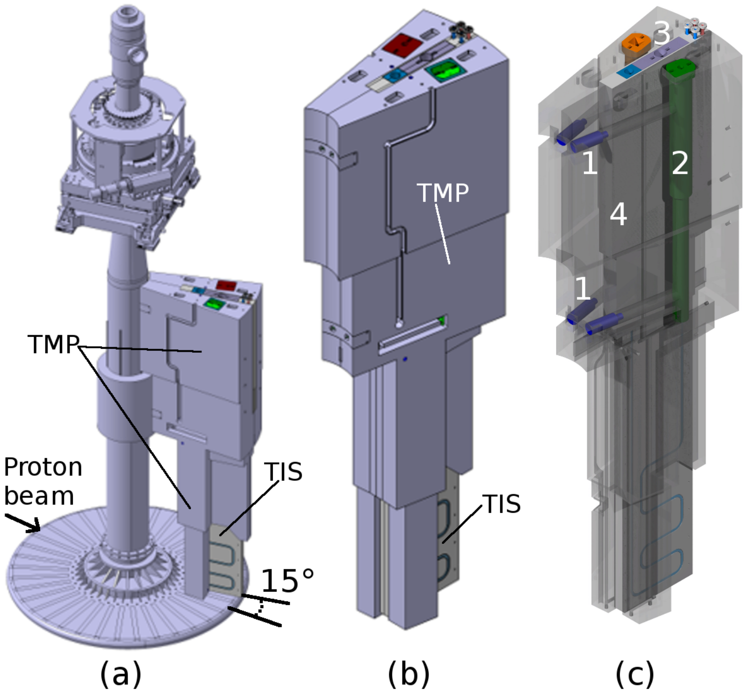

Figure 3.2: Three dimensional representation of the TMP: (a) TMP placement relative to the target wheel; (b) detail of the TMP assembly; (c) transparency of the TMP highlighting the comprised instruments (1: shaft tilting measurement, 2: helium cooling temperature measurement, 3: vertical wheel displacement measurement, 4: target inner structure imaging) [26].

length of the reflected light, it is possible to calculate the distance of the focal point, hence the distance from the sensor;

2. the green insert on the right wall of the TMP is reserved for the measurement of the cooling helium temperature. The temperature will be measured at the inlet position and at the edge of the wheel, above the outermost row of tungsten bricks. The instrument relies on the emitted thermal radiation. Two separate paths are machined into the TMP to allow the Infrared Radiation (IR) to reach the detectors while avoiding neutron straight streaming pipes that would compromise the monolith shielding;

3. the orange insert is dedicated to the measurement of the wheel displacement along the shaft's axis (z). Similarly to the measurement of the shaft tilt, excesses in the z displacements can lead to collisions and to potential

damages to the target station. The measurement technique is based on a phase comparison of a laser light diffusely reflected by the rotating wheel;

4. the central component of the TMP will be reserved for the TIS. As it will be discussed in more detail later, the TIS is intended to monitor the internal structure of the brick layout to detect blockages that could compromise the correct flow of the cooling helium.

So far, the only evaluation of the accident case corresponding to a damage of the brick layout involves only two bricks touching each other after a non-specified mechanical failure. The accident scenario is described as follows [56]:

1. ESS is in mode "Operation - Beam ON" at 5 MW power;
2. the wheel is rotating and synchronized with the proton beam;
3. the flow of coolant is regular (3 kg/s of helium at 10 bar);
4. a channel between two bricks is blocked;
5. a local temperature increase (up to 600 °C) is registered (Fig. 3.3); the temperature, though, does not reach the tungsten oxidation point;
6. no release of radioactive material is expected.

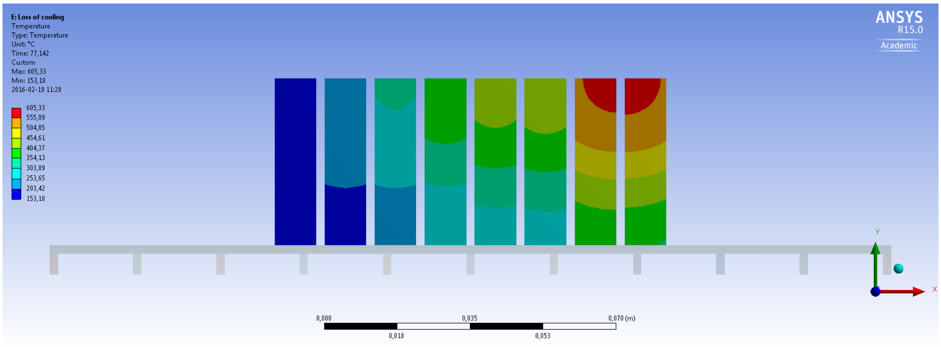

Figure 3.3: Maximum tungsten temperature with one passage blocked [56].

3.2 TIS proposal: principles and system response

Despite the abundance of studies on tungsten under different operating conditions and the detailed simulations of the accident cases, no direct experience is available for the ESS target technology. The high power of the facility (125 MW peak), the scale of the target wheel with its 7000 bricks, the cooling solution with helium flowing in the narrow grid spacings are all unprecedented solutions. Moreover, the tests on debris accumulation and the accident case scenario with only two bricks in contact only represent a small fraction of the potential issues that could arise.

The expected target lifetime has been set to 5 years. The lifetime limiting factor is the estimated resistance to radiation damage of the steel vessel surrounding the tungsten bricks. This figure has been calculated from post-irradiation examinations of the Spallation Neutron Source (SNS) target vessel [57]. The tungsten bricks, instead, are not designed to carry any structural load, but their failure can nevertheless threaten the target lifetime. Thorough investigations of the tungsten fatigue do not provide univocal indications, hence a clear estimate of its lifetime can only be achieved by constant monitoring during operation [58].

It is important to stress that if damage to the tungsten or to the steel structure occurs, there will be no possibility of repairing the failure. Indeed, major accidents occurring either in the steel vessel or in the tungsten bricks would lead to the replacement of the entire target; minor damages, on the other hand, could be overcome by adapting the proton pulse train: irradiations of a damaged wheel sector can be either performed at a reduced power or completely skipped.

By constant monitoring of the integrity of the wheel's inner structure, the TIS will provide invaluable insight on the tungsten behaviour under the ESS conditions. This will contribute to the target maintenance planning and will represent the knowledge basis for accident investigations and for future target development.

The TIS is not intended as a safety system: a target failure will always be accompanied by several other alterations to the ordinary conditions, such as anomalies in the helium flow rate, raise of coolant temperature, losses of pressure in the helium loop, unexpected increase of radioactivity levels in the cooling loops, mechanical anomalies, alert signals from the proton beam instrumentation, etc. Therefore, also for licensing purposes, the safety of the ESS operations should rely on a minimum set of parameters provided by well-known and tested sources. In this respect, the implementation of the TIS will be the opportunity of investigating the target and its potential failure points, but also the playground to further develop the diagnostic system itself.

As with the other TMP instruments, it is also fundamental that the TIS should be a non-contact tool. The rotation of the wheel, together with the temperature and the radiation levels reached on the target's surface do not allow the placement of any instruments on the target assembly. The requirements the TIS needs to fulfill are stringent [59]:

- to image the 2 mm cooling channels, the spatial resolution cannot exceed 1 mm;
- the TIS must be able to monitor the full radius of the wheel;

- the frequency of the measurements should be at least 10 kHz to provide at least three measurements per millimeter;
- the TIS must not compromise the performance of the monolith shielding.

The principle on which the TIS is based is that of the Anger camera (or gamma camera), commonly used in medical imaging applications, such as in Single-Photon Emission Computed Tomography (SPECT) [60]. The simplest construction of the gamma camera consists of a lead pinhole projecting an inverted image of the photons emitted by a radioactive source onto a scintillator (typically NaI) placed in front of an array of several Photo-Multiplier Tubes (PMTs) [61, 62].

The pinhole-based gamma camera provides a good sensitivity and resolution but the Field Of View (FOV) is limited. Improvements on this design include multi-pinhole collimators and parallel-hole collimators [62].

The TIS is based on the latter, i.e. on the parallel-hole design, but with two main differences:

- it is expected to work in a harsh radiation environment, as opposed to the medical gamma camera, which is specifically designed to operate under almost background-free conditions;
- instead of a wide scintillator block or honeycomb layout of PMTs, each collimator channel is individually matched to a small scintillator crystal.

The TIS is intended to detect gamma radiation from the tungsten bricks and, to achieve high spatial resolution, a long collimator is located perpendicular to the target wheel (Fig. 3.2(a)).

The collimator allows the rejection of the unwanted photons based on their direction of travel and restricts the instrument's FOV. To prevent distortion of the viewed image, the TIS relies on a *parallel-hole* collimator; this consists of a set of parallel holes perpendicular to the target surface.

In Fig. 3.4 the collimator geometry is sketched, highlighting the parameters affecting the spatial resolution R_C (Eq. 3.1) [63]:

$$R_C = \frac{d}{l}\left(l + b + |z|\right) \tag{3.1}$$

where d is the size of the collimator hole, l the hole length, b is the effective detector depth (scintillator crystals in this case) and $|z|$ the collimator-to-target distance.

The spatial resolution R_C of the collimator degrades for larger $|z|$, therefore the collimator-to-target distance must be kept to a minimum. The TIS configuration is as follows: $d = 1$ mm, $l = 2850$ mm, $b = 10$ mm and $|z| = 20$ mm, thus resulting in (Eq. 3.2):

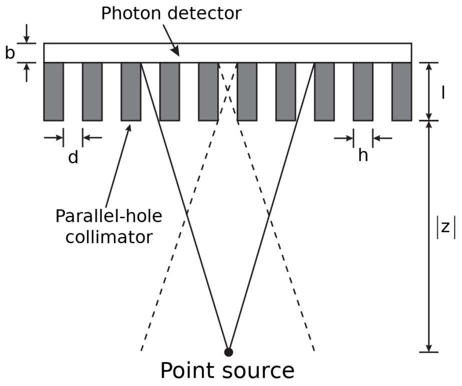

Figure 3.4: Collimator geometry [63].

$$R_C = \frac{1}{2850}\,(2850 + 10 + 20)\ \text{mm} = 1.01\ \text{mm} \tag{3.2}$$

The TIS collimator will be fixed to the TMP and will extend radially. Therefore, the spatial resolution R_C in Eq. 3.2 will not be adjustable along the wheel radius.

It is important to underline that a single row of collimator holes would not be sufficient to uniformly cover the wheel radius. Indeed, as Fig. 3.4 suggests, a 2.85 m long collimator will only allow perpendicular tracks (the viewed solid angle for each groove is of the order of 10^{-9} rad) to reach the end of the block. Therefore, using a single row of holes separated by a 1 mm septum, only a discontinuous image would be obtained. A second row of holes, parallel to the first and offset radially by 1 mm, is necessary to ensure an uninterrupted coverage of the radial axis. This configuration is shown in Fig. 3.5.

Having established that the planned configuration gives a radial spatial resolution of 1 mm and that two parallel rows of grooves are required to fully cover the $\sim$ 50 cm wheel radius, it is straightforward that a total of 500 collimator holes is required.

3.2.1 Characterization of the TIS source term

It is now necessary to discuss the source of photons constituting the signal used for the imaging of the target.

As discussed in the previous sections, the spallation process produces a broad range of isotopes. Many of these are radioactive and undergo α, β and γ decays. It is important to estimate, by means of Monte Carlo simulations and activation calculations, the inventory of radioactive nuclides present in the target after the spallation process.

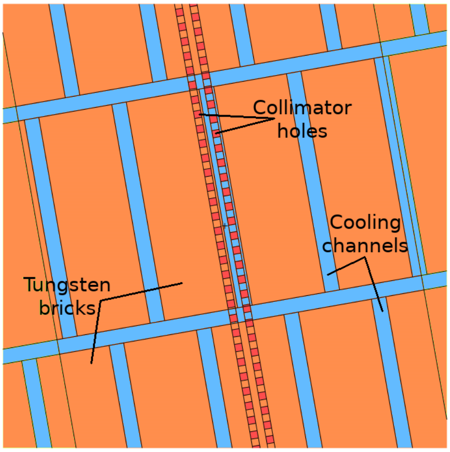

Figure 3.5: Schematic representation of the bricks-collimator arrangement.

The MCNPX Monte Carlo code has been used to simulate the spallation reaction and to calculate the neutron flux within each of the 172 bricks in one wheel sector [64, 65]. This information has then been processed with the CINDER'90 burn-up code, which allows calculation of the nuclide inventory as a function of time [66].

In particular, the CINDER'90 irradiation history used is the following:

1. 2700 h of beam on at 5 MW (corresponding to half a year of ESS operations);
2. 1680 h of cooling (corresponding to the planned maintenance stop);
3. 2700 h of beam on at 5 MW (for the remaining half year of operations);
4. 30 repetitions of the fine beam cycle:
    a. 2.86 ms of beam on at 125 MW (peak power);
    b. 2.57 s of beam off (corresponding to one full wheel revolution before the same sector is irradiated again).

The long irradiations at average power ensure the build up of all the isotopes, whereas the last 30 cycles at full power ensure the detailed inventory on a pulse timescale, therefore computing more precisely the contribution of the short-lived isotopes.

After the last irradiation at full power, the inventory has been calculated after 1 s of cooling time, which is the time required by the wheel's sector to move from the irradiation position to the imaging position (Fig. 3.6).

At this stage, the activation of one wheel sector is resulting in a decay gamma emission peaking in correspondence of the spallation hotspot, as shown in Fig. 3.7,

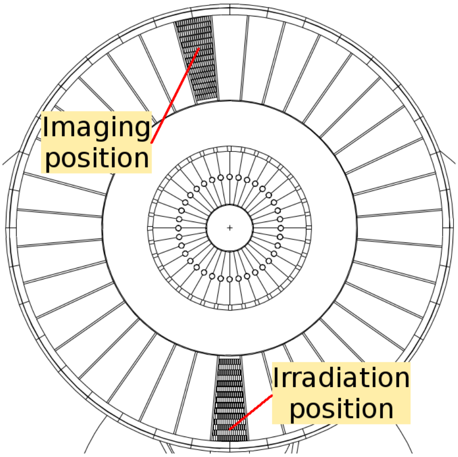

Figure 3.6: MCNPX model of the target wheel (top view) showing irradiation and imaging positions. The transition time is 1 s.

which is located around the second row of bricks and centered along the azimuthal coordinate.

To avoid biased analysis due to the high activity around the hotspot, detailed investigation of the nuclide inventory has been carried out only on the bricks within the black dashed rectangle in Fig. 3.7. In particular, the energy spectrum of the decay γ radiation relative to the cell marked with the red dot was calculated. The result is shown in Fig. 3.8(top) by the blue line.

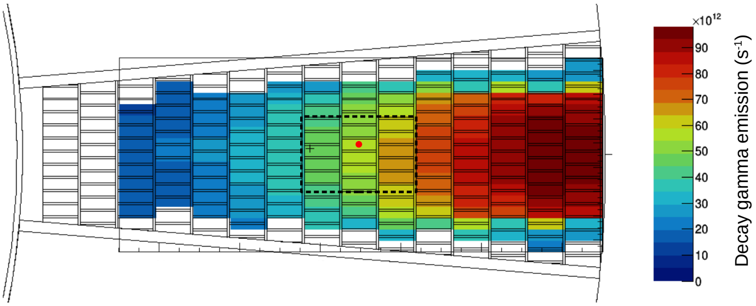

Figure 3.7: Intensity map of decay γ radiation originating from one target sector. Detailed calculations have been carried out for the bricks within the black dashed rectangle, which represent an average sample of the 172 bricks.

The energy resolution provided by CINDER'90 is limited to 25 energy groups. Despite the coarse resolution, the two most intense γ lines from ^{187}W can be identified. The detailed decay scheme of ^{187}W is presented in Fig. 3.9 and the two main lines are reported (red dashed lines) on Fig. 3.8(top) for reference.

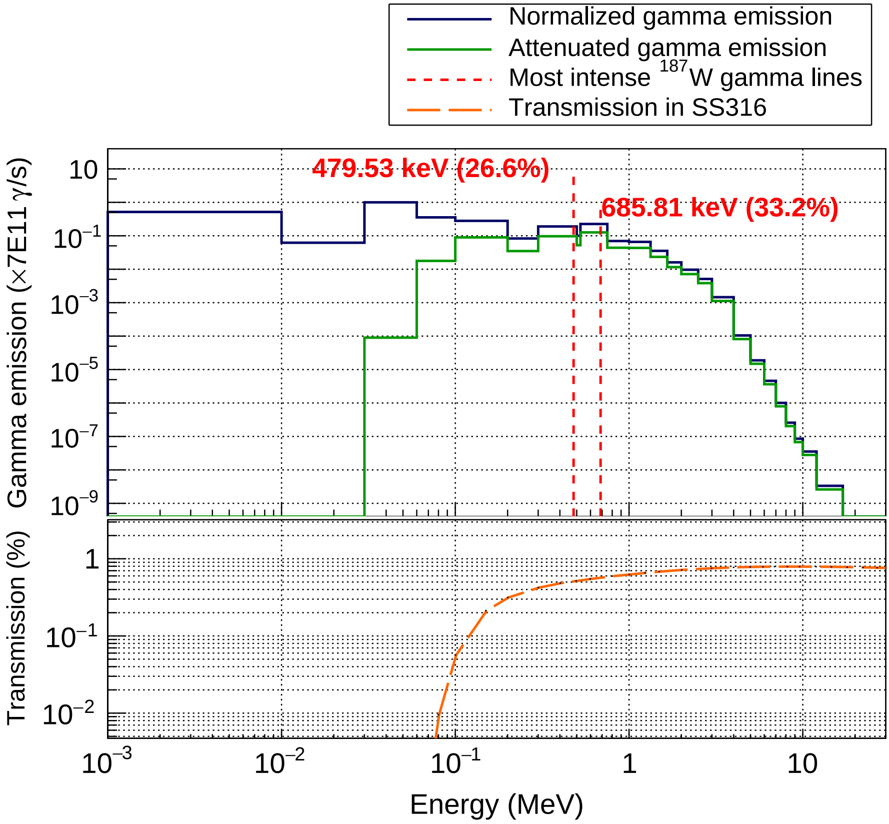

Figure 3.8: Energy spectra before (blue) and after (green) attenuation in steel of the decay γ radiation (top). The red dashed lines correspond to the two most intense peaks from ^{187}W. The fraction of emerging photons is plotted in the bottom panel.

The tungsten bricks are encased in a 1 cm-thick stainless steel (SS316) structure. The SS316 mass attenuation coefficient $\mu_g(E)(\mathrm{cm}^2/\mathrm{g})$ as a function of photon energy is shown in Fig. 3.10 [69]. A density of 7.85 g/cm^3 was considered in the simulations.

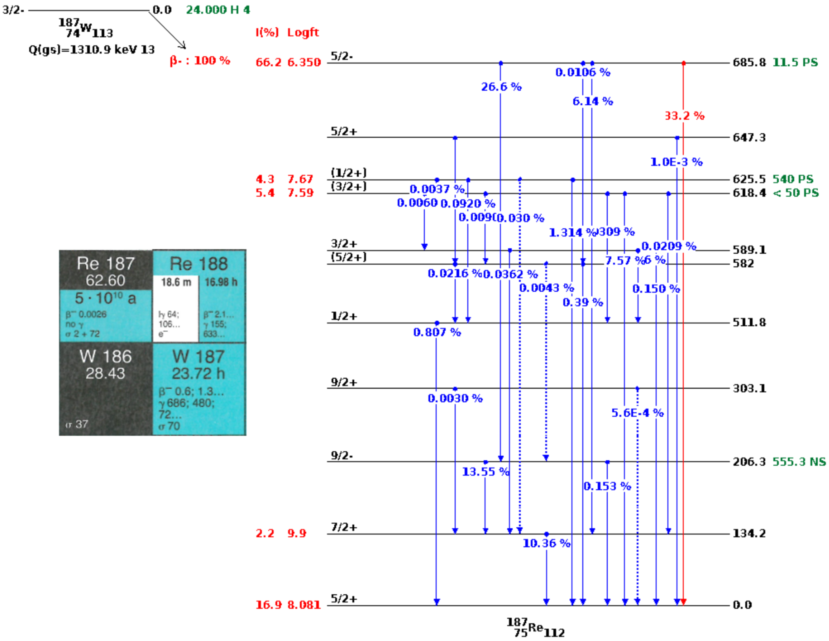

Figure 3.9: Decay scheme of ^{187}W. Only energy levels below 700 keV have been selected for display. The decay channel highlighted in red is the one mainly responsible for the TIS signal [67, 68].

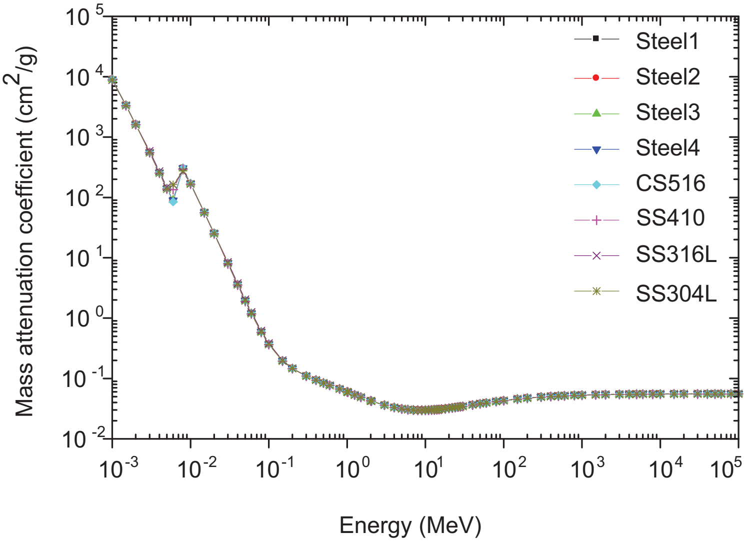

Figure 3.10: Mass attenuation coefficients for photons in different types of carbon and stainless steel [69].

The fraction of photons emerging from the steel vessel, calculated according to Eq. 3.3, is shown in Fig. 3.8(bottom).

$$\frac{I}{I_0} = \mathrm{e}^{-\mu x} \quad \text{where} \quad \mu = 7.85\ \mathrm{g/cm^3} \times \mu_{\mathrm{g}}(E) \quad \text{and} \quad x = 1\ \mathrm{cm} \tag{3.3}$$

Finally, the energy spectrum of the photons emerging from the shroud is calculated and shown in Fig. 3.8(top) by the green line.

All the low energy contributions ($E \leq 200$ keV) are strongly attenuated by the shroud, and the formation of the TIS signal is therefore dependent on the presence of the 480 keV and 686 keV γ lines from ^{187}W. The cooling helium is not contributing to this signal. Hence, it is possible to map higher photon counts with the portion of the wheel containing bricks, whereas fewer counts correspond to the interstitial space filled with helium. Not only tungsten, though, is susceptible to activation: neutrons will indeed activate all the steel shroud and many other parts of the target monolith. The intensity of the resulting decay γ radiation, representing a steady state background, has also been calculated by means of the same simulation procedure discussed above and its magnitude is of the same order of magnitude as the signal from the tungsten. This confirms the possibility to isolate the signal from the background to perform the intended target imaging.

Simulations supporting the concept have been carried with MCNPX and the results for a stationary wheel configuration are further discussed in Paper 1.

ICANS XXII IOP Publishing
IOP Conf. Series: Journal of Physics: Conf. Series **1021** (2018) 012020 doi:10.1088/1742-6596/1021/1/012020

Development of a target imaging system for the European Spallation Source

Nicolò Borghi[1], Esben B Klinkby[1], Bent Lauritzen[1], Eric Pitcher[2], Nigel Poolton[1] and Luca Zanini[2]

[1]Technical University of Denmark, DTU Nutech, Risø Campus, Frederiksborgvej 399, Bldg. 201, 4000 Roskilde, DK
[2]European Spallation Source ERIC, Tunavägen 24, 223 63 Lund, SE

E-mail: `nicbo@dtu.dk`

Abstract. At the European Spallation Source (ESS) neutrons will be produced by a proton beam impinging on a rotating target wheel. The technology of the target wheel, which comprises a large number of closely spaced tungsten bricks and is cooled by helium, is largely untested. The durability of the target wheel and hence the overall ESS neutronic performance depend on the integrity of the tungsten bricks. In order to monitor whether the target geometry is preserved over the expected 5 year lifetime of the target wheel, we propose a Target Imaging System (TIS). The TIS consists of a scintillator array detecting the collimated single photon emission (decay gammas) from the activated tungsten bricks. Preliminary Monte Carlo simulations support the feasibility of this imaging system. As a proof-of-principle, an experimental test-rig is being constructed allowing to test the main aspects of the imaging system under conditions relevant to ESS.

1. Introduction

The European Spallation Source (ESS) will be the most powerful spallation neutron source in the world. Neutron production is initiated by a 2 GeV, 5 MW proton beam impinging on a rotating target wheel, comprising a large number of closely spaced tungsten bricks encased in a steel vessel [1]. The technology of the helium-cooled tungsten wheel, however, is largely untested and the durability of the target wheel depends *inter alia* on the integrity of the tungsten bricks. The tungsten bricks will operate in a brittle regime after exposure to radiation and thermal stresses, both of which may induce erosion or cracking of the bricks, eventually resulting in the blocking of the coolant channels, unwarranted heating and loss of mechanical stability of the wheel.

2. The Target Imaging System

Among several diagnostic systems currently under development, we propose a Target Imaging System (TIS) in order to investigate whether the target geometry is preserved over the expected 5 year lifetime of the target wheel. The TIS is intended to provide a means for a high spatial resolution recording of the decay gammas from the target wheel.

During operation, the target with the tungsten bricks is exposed to intense particle irradiation, especially protons and neutrons, giving rise to highly radioactive bricks, encased in a steel vessel of somewhat lower activity. By recording the decay gammas from the tungsten bricks, the TIS will be able to detect changes to the brick layout, especially the presence of brick fragments in the cooling channels between the bricks.

The TIS is not a safety system but is intended as a monitoring instrument capable of providing support to issues of target maintenance and operation, as well as future design development.

As shown in figure 1(a), the TIS is positioned in the vertical target diagnostic plug that lies above the target wheel, on the side opposite to the incoming proton beam and forming a 15° angle (azimuthal) with respect to the proton beam axis.

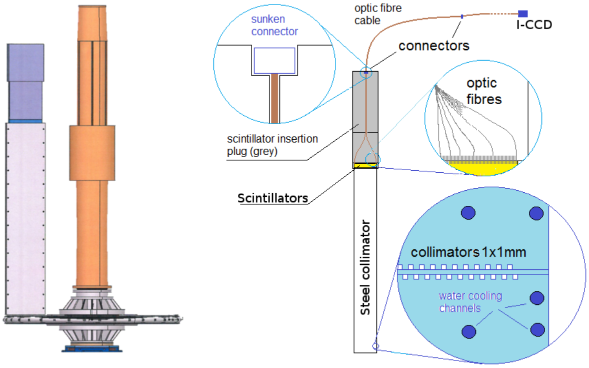

(a) (b)

Figure 1. (a) Target diagnostic plug positioning relative to the target system; (b) schematic representation of the main components of the TIS.

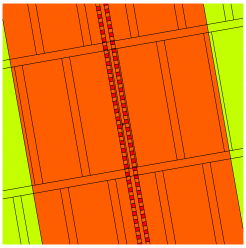

Figure 2. MCNPX model of the horizontal cross section of tungsten bricks superimposed with collimator grooves.

The TIS is composed of four main components, outlined in figure 1(b):

- a 2.8 m steel collimator suspended 2 cm above the target wheel and normal to its plane. A total of 500 1×1 mm^2 grooves are machined into the collimator structure, aligned along two rows, offset by 1 mm with respect to each other and separated by a 1 mm septum;
- on top of the collimator, a scintillator cartridge housing 500 $1 \times 1 \times 10$ mm^3 scintillators. Each scintillator is precisely coupled to a single collimator groove;
- an optical fiber bundle, where each fiber is coupled to a scintillator. The fiber bundle is $10 - 15$ m long and will be routed outside the ESS target monolith. To comply with ESS requirements, extra shielding material is surrounding the optical fiber bundle;
- a fast-switching (3 ns) image-intensified CCD camera coupled to the optical fiber bundle, to register the scintillation photons.

The TIS can be seen as the collection of 500 independent read-out channels, each composed of a collimator, a scintillator, a fiber and a CCD detector. Each of these channels will detect decay gammas emitted by the tungsten bricks, allowing for a high spatial resolution image.

In figure 2, details of the MCNPX geometry are shown, where the horizontal cross section of the tungsten bricks has been superimposed on the collimator grooves. The two rows of collimators allow the desired spatial resolution (1 mm) to be achieved while ensuring radial coverage of the target wheel; the imaging along the azimuthal direction is achieved through rotation of the wheel.

3. Data acquisition and imaging

With the high spatial resolution required for proper monitoring of the target wheel, each of the scintillators will have a count rate of about 10 γ/s. For each of the collimators, the passing time for a collimator across the gap between the bricks (that act as cooling channels) is of the order of 300 μs during normal operation, hence real-time image reconstruction is not possible. However, by taking advantage of fast image-intensified CCD cameras, several accumulation techniques may be envisaged to gather sufficient statistical significance in a relatively short time during ESS operation. This includes sector-averaging, in which only high-spatial resolution is maintained in the radial direction, supplemented by intelligent gating procedures allowing for high-spatial azimuthal angular resolution covering smaller sections of the wheel.

Two main sources of noise will affect the measurements:

- prompt γ background, resulting from the spallation process. This can effectively be avoided by limiting the acquisition time to the beam-off intervals;
- delayed gamma background, resulting from the activation of all the components within the monolith, including the scintillators themselves. This background can be limited with specific shielding.

4. Neutronic simulations

Extensive Monte Carlo simulations and activation calculations, performed with MCNPX [2] and CINDER'90 [3], respectively, are carried out to investigate the signal-to-noise ratio of the TIS.

The MCNPX and CINDER'90 simulations are carried out in three phases: (i) MCNPX simulation of a 2 GeV proton beam impinging on the target wheel to calculate the neutron fluxes in one sector of the wheel; (ii) CINDER'90 activation calculation. For the latter, we employed the following time structure:

- 1 year irradiation at 5 MW i.e., average power of the proton beam;
- 30 irradiation cycles comprising 2.86 ms irradiation at peak power (125 MW) interleaved with 2.57 s cooling time;
- cooling time of 1 s.

The 1 s cooling time corresponds to the time needed for the wheel to move from the irradiation position to the imaging position, i.e. the measurement of a sector of the target wheel is performed 1 second after the proton pulse. Finally, an MCNPX simulation is performed to calculate the instantaneous gamma flux at the scintillators.

In figure 3, the result of the simulation is shown, corresponding to the layout of figure 2. The figure shows the gamma flux at the position of the scintillators; each point corresponding to one of 113 scintillators included in the simulation. The cooling time is 1 s.

The blue dots correspond to the left row of scintillators in figure 2, imaging three bricks, whereas the red dots are for the right row, imaging two bricks only. The cooling channels in between the bricks are associated with the reduced gamma fluxes at around 300 $\gamma/\mathrm{cm}^2/\mathrm{s}$. Note that the overall gamma intensity grows with the distance from the target shaft, since the primary proton beam intensity is larger at the wheel edge. The constant values of the gamma flux across each of the bricks is an artifact of the simulation where each brick is treated as a single cell.

5. The test-rig

As a proof-of-principle for the TIS, a test-rig is being constructed at DTU. A 3D view of the setup is provided in figure 4(a). The test-rig will be equipped with 60 collimator grooves; 30 with 1 mm^2 cross section and 30 with 0.5 mm^2 cross section, allowing for different spatial resolutions. A scaled model of the wheel, shown in figure 4(b), will be fitted with several resolution targets

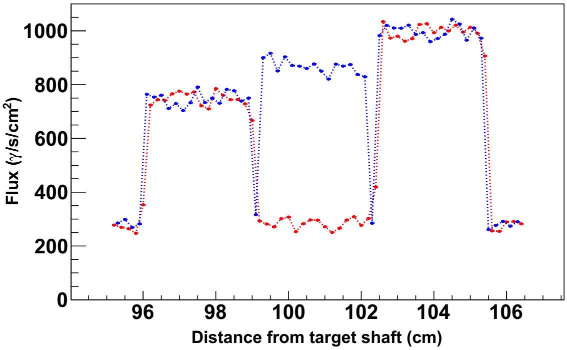

Figure 3. Simulated gamma flux at the scintillators 1 s after irradiation: left row (blue), right row (red). Background due to activation of the monolith has not been included. Dotted lines are to guide the eye.

made of lead. While the lead targets will not be activated themselves, measurements will be performed using the DTU Nutech medical radiation source (^{60}Co, 450 TBq).

The test-rig will allow assessment of the detector performance of the proposed TIS in terms of spatial resolution, temperature-dependent signal degradation, radiation damage of the components, etc. In addition, data acquired from the measurements of the test-rig will be used for the development of the control and data analysis software.

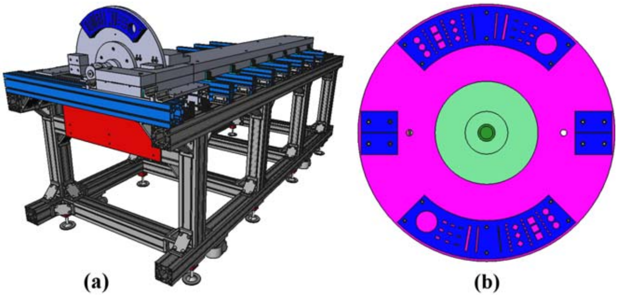

Figure 4. (a) The DTU test-rig: 3D rendering of the entire setup; (b) detail of the model wheel with resolution targets.

References

[1] Peggs S (editor) 2013 *ESS Technical Design Report* ESS-doc-274
[2] Pelowitz D (editor) 2011 *MCNPX User's Manual, Version 2.7.0* Los Alamos National Laboratory LA-CP-11-00438
[3] Wilson W B *et al* 2007 *RSICC Computer Code Collection - CINDER 1.05 - Code system for actanide transmutation calculations* Oak Ridge National Laboratory LA-UR-07-8412

3.3 Basic design and mode of operation

The simulations presented in Paper 1 support the concept of a gamma-camera based TIS. The results, however, are relative to a stationary investigation, where only the radial spatial resolution can be assessed. The purpose of the TIS is to provide data from the ESS target both in the radial (r) and azimuthal (θ) directions.

This section, covered by a published paper, provides further details about the design of the proposed TIS and about the data acquisition in (r, θ) coordinates. The timing of the acquisition and the gating schemes are discussed. Finally, the anomaly detection capability is investigated by means of the Pearson's χ^2 statistical test applied to simulated data.

DETECTION EFFICIENCY OF THE ESS TARGET IMAGING SYSTEM: MONTE CARLO SIMULATIONS

N. Borghi, E. Klinkby, B. Lauritzen
Technical University of Denmark – DTU Nutech
Frederiksborgvej, 399 – 4000, Roskilde – Denmark
nicbo@dtu.dk; esbe@dtu.dk; blau@dtu.dk

L. Zanini
European Spallation Source ESS ERIC
Box 176 – S-221 00, Lund – Sweden
luca.zanini@esss.se

ABSTRACT

A Target Imaging System (TIS) is proposed for the European Spallation Source (ESS) aiming at detecting damaged areas of the spallation wheel, e.g. due to erosion or cracking of the spallation tungsten bricks. The TIS is a collimator imaging camera consisting of an array of scintillators individually coupled to an image-intensified sCMOS camera; the TIS records the 1D radial distribution of decay gammas from the activated target material while 2D image reconstruction is achieved through rotation of the target wheel. To investigate the efficiency of the TIS in detecting errors in the tungsten brick geometry, numerical simulations of the gamma fluxes are performed using MCNPX and CINDER90 software packages and image reconstruction algorithms are described that will allow detection of anomalies, e.g. in the form of brick fragments trapped in the cooling channels between the tungsten bricks. Preliminary results indicate that the TIS will be capable of detecting such anomalies in the target wheel.

KEYWORDS
Image reconstruction, Imaging system, Gamma camera, ESS

1. INTRODUCTION

Neutron production at the European Spallation Source (ESS) will be initiated by a 2-GeV proton beam with an average current of 2.5 mA impinging on a tungsten target [1]. The ESS target is unique among spallation neutron sources: the target comprises a helium cooled rotating wheel of diameter 2.5 m, subdivided into thirty-six 10° sectors, each containing around 180 tungsten bricks with dimensions of $1\times3\times8$ cm^3. The bricks are directly exposed to the helium flow, and erosion or cracking of the bricks could occur during operation, with fragments ending up in the cooling channels in between the bricks. This may damage the target structural integrity potentially leading to target failure and ultimately reducing the 5 year expected lifetime of the wheel.

A Target Imaging System (TIS) has been proposed to monitor the target wheel during operation and detect possible damage [2]. The TIS is based on the detection of the gamma radiation emanating from the activated tungsten bricks and provides a means of reconstructing an image of the inner target structure.

In this study, the principles for data acquisition and an image reconstruction methodology that allows the identification (presence, location and extent) of anomalies in the brick configuration are described. To examine the performance of the TIS, preliminary numerical simulations of the target image are performed for different types of anomalies. The capacity of the TIS for detecting anomalies in the target wheel is derived through statistical analysis of the reconstructed image of a healthy wheel and wheels with anomalies in the brick configuration.

2. THE TARGET IMAGING SYSTEM

The TIS is conceptually similar to the Anger camera used in medical applications [3]. In the TIS, the gamma emission from the decay of radioactive isotopes in the target wheel is collimated and, by means of scintillators, converted into light suitable to be transported by optical fibers towards an Intensified sCMOS (I-sCMOS) camera for the final acquisition. Thanks to the collimation stage, the emission position of the decay gammas can be mapped to the I-sCMOS detector, providing an image of the radioactive gamma source.

2.1. Detailed TIS Design

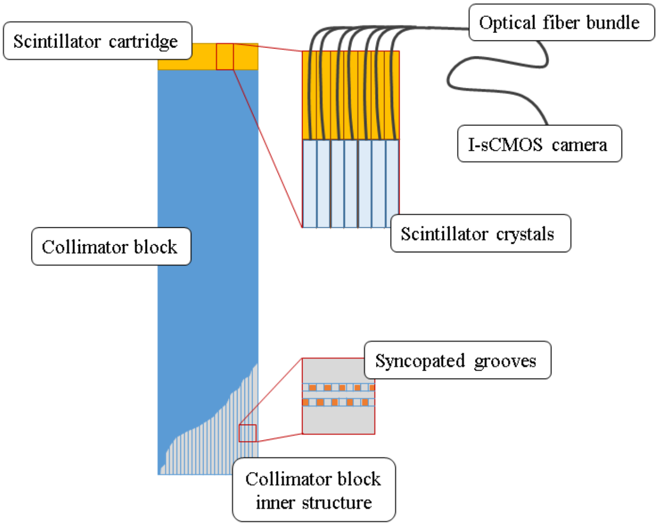

Figure 1. Schematic TIS design

The proposed configuration of the TIS, presented in Fig. 1, includes four components:

1) A 2.8-meter long steel collimator, in which two parallel rows comprising 350 1×1 mm^2 grooves, offset by 1 mm and separated by a 1 mm septum are machined. The dimensions of the grooves ensure a narrow angular acceptance, important to achieve the required spatial resolution of 1 mm.
2) A scintillator cartridge connected to the collimator body, comprising 350 $1\times1\times10$ mm^3 scintillator crystals, each coupled to a single groove. Since radiation and alternating temperatures will

progressively damage the crystals, thus reducing their detection efficiency, the scintillator cartridge is removable, allowing for periodic replacements.

3) A fiber optic bundle, composed of 350 individual fibers, each optically coupled to a single scintillator. The search for the suitable material for the optical fibers is ongoing, considering the ability to withstand high radiation levels, accessibility of the components for regular maintenance and commissioning/maintenance costs.
4) An Intensified sCMOS camera reading the scintillation light conveyed by the fibers, positioned 10-15 meters away from the intense radiation fields. The sCMOS camera allows for a large number of frames per second (fps), fundamental to the TIS since the characteristic passing time of 1 mm under the field of view of the collimator is of the order of 300 s. The image intensifier coupled to the sCMOS camera allows to amplify the optical signal from the scintillators and provides flexible gating opportunities. This enables the TIS to avoid prompt background from proton beam pulses and to select specific areas of the target wheel for detailed investigation.

While the imaging in the radial direction is achieved by means of the 350 scintillators, the imaging along the azimuthal coordinate is achieved by means of the wheel rotation. With the TIS geometry, high radial resolution is intrinsically available, whereas the resolution in the azimuthal direction is determined by the chosen gating scheme of the image intensifier.

Apart from the I-sCMOS camera, all other components of the TIS will be housed within the target monolith. The TIS will be part of a larger assembly, the Target Monitoring Plug (TMP), which includes other diagnostic systems, such as vibration and temperature sensors. The TMP will be located opposite the target shaft and oriented at a 15° angle with respect to the incoming proton beam (Fig. 2).

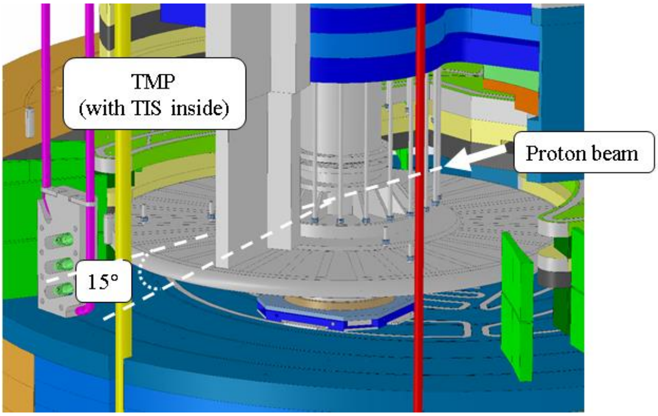

Figure 2. Location of the Target Monitoring Plug within the ESS target monolith.

2.2. Data Acquisition and Image Reconstruction

Data collection of the TIS is controlled by the I-sCMOS camera, which can be gated according to user requirements. In particular, the gating can serve two purposes:

1) Prompt background suppression: the image intensifier suppression ratio (10^8) is large enough to ensure that, when the gate is closed, no light reaches the sCMOS chip. In addition, the positioning of the TIS within the target monolith ensures that, during the proton pulses (i.e. when the gate is closed) the collimator is directed at the supporting structure between adjacent sectors of the wheel, thereby ensuring that no important signal is lost due to the gating.
2) Variable-resolution acquisition: low spatial resolution of the entire wheel or high spatial resolution of smaller areas of interest can be achieved by means of the image intensifier. Due to its switching on/off times being of the order of a few tens of nanoseconds, the gate can be triggered whenever an area of interest falls within the field of view of the collimator. From an anomaly detection perspective, the variable resolution enables the TIS to narrow down on the impurities found in the grid of tungsten bricks and eventually reconstruct a high-resolution image of the problematic area.

Two gating strategies are envisaged:

1) *Full-arc time averaged* gating: this scheme allows to acquire data from a whole wheel segment. The integration time t_g is constant, given by the passing time of one sector minus the proton beam-on time:

$$t_\mathrm{g} = t_\mathrm{sector} - t_\mathrm{pulse} = (71.38 - 2.86)\ \mathrm{ms} = 68.5\ \mathrm{ms} \qquad (1)$$

   The gating of the camera intensifier will be synchronized with the position of the wheel, so that the optical switch is opened as soon as the proton pulse is off and is closed after passing of the segment, prior to the next proton pulse. The photon counts are independently accumulated for each scintillator; the data are stored to free the camera memory for subsequent data acquisition. At successive wheel revolutions, data from corresponding sectors will be added and averaged over time.
2) *Narrow intra-rotation* gating: more complex time structures for the camera gating can be implemented allowing for the imaging of smaller portions of a wheel sector. In this mode of operation, short gating times will imply larger readout noise of the camera electronics. To overcome this effect, on-chip integration can be used to accumulate data before the readout stage, rather than storing them after each acquisition event. The main drawback of this solution is that data must be preserved onto the sCMOS chip for a number of wheel rotations, depending on the required spatial resolution.

The aim of the TIS is to reconstruct target images that can be used to identify anomalies in the target brick configuration. The ability of the TIS to detect errors or anomalies in the spallation wheel is based on the assumption that the main contribution to the activity comes from the isotopes contained in the tungsten bricks and not from the cooling channels. Therefore, regardless of the gating scheme chosen, any brick fragment or radioactive debris accumulating within a cooling channel will result in a variation of the activity. If the image reconstruction algorithm is capable of resolving this kind of anomaly, the location and extent of the damage can be investigated.

The reconstruction procedure can be subdivided into three logical steps: i) selection of the required gating scheme in order to determine which parts of the wheel should be investigated; ii) selection of the required acquisition time to accumulate sufficient statistics; iii) comparison of reconstructed image with a reference image in order to evaluate the condition of the selected area of interest. The evaluation is performed by means of statistical evaluators, such as the Pearson's χ^2 test or the Kolmogorov-Smirnov test [4]. If the comparison of the two images suggests the presence of an anomaly in the target geometry, the above steps are re-iterated, adapting the gating scheme.

Data from the TIS can be presented in the form of either a 1D or 2D histogram. An example is provided in Fig. 3, where the 1D histogram shows the simulated number of photons reaching the scintillators as a function of the distance from the wheel center, corresponding to the full-arc gating mode. This imaging mode provides an overview of each segment and can lead to the identification of the *presence* of a problem. When shorter gating windows are chosen to narrow down on a smaller region within one sector, 2D images of the wheel sector can be derived.

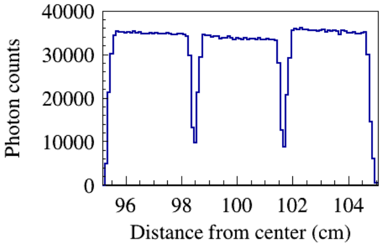

Figure 3. Simulated photon counts in the full-arc gating scheme showing the number of primary photons reaching the scintillators for an acquisition time of two days.

3. NUMERICAL SIMULATIONS

To investigate the feasibility of the TIS, numerical simulations are performed of the nuclide inventory in the target wheel and the corresponding gamma field, as well as the detection and image reconstruction processes. The first task is accomplished by means of the MCNPX and CINDER90 codes to yield the gamma flux at the scintillators [5, 6]. To address the simulation of the image reconstruction and the possibility for error detection, a simplified approach is taken where the detection efficiency is reduced to a geometrical problem. Eventually, the physics of the Monte Carlo simulations should be merged with the geometrical description to obtain a complete overview of the TIS operation.

3.1. Gamma Fluxes from MC Simulations

Simulation of the decay gammas recorded by the TIS is divided into four steps:

1) MCNPX is used to simulate the spallation process, starting from protons impinging on the tungsten target. The initial setup of the MCNPX calculation involves 2-GeV protons impinging on sector 1 (Fig. 4) of the target wheel, and the neutron flux in the target wheel including the steel casing is determined.
2) Activation of the tungsten bricks and the steel casing is calculated with the activation code CINDER90. The irradiation scheme is chosen to reflect the conditions after 1 year of ESS operation at the nominal 5 MW average beam power. The last target irradiation steps are taken as 30 rotations of the wheel at peak beam power: 125 MW for 2.86 ms and no beam for the remaining 68.5 ms, corresponding to a 14 Hz rotation frequency with a 4% duty cycle.

3) The gamma spectrum is extracted 1 second after the last irradiation, corresponding to the rotation of the wheel from the irradiation position (marked number 1 in Fig. 4) to the location of the TIS (number 2 in Fig. 4).

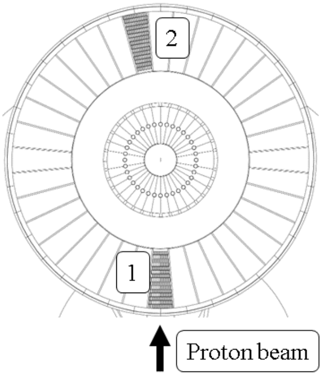

**Figure 4. Top view of the target wheel (MCNPX model).
(1) Irradiated segment; (2) Segment imaged by the TIS.**

4) Finally, a gamma-only MCNPX simulation is carried out to estimate the flux reaching the scintillators. With the scintillator plane 2.8 m above the target wheel most of the sampled source photons would be emitted in directions not contributing to the TIS signal. Hence, source biasing has been introduced so that the gamma emission is limited to a cone with an aperture equivalent to the viewed solid angle. The observable of interest is the gamma flux at each scintillator (Fig. 5).

In Fig. 5(a), the blue points (circles) follow the profile of three bricks interleaved with two transversal cooling channels, corresponding to the left row of scintillators (Fig. 5(b)), whereas the red points (triangles), give the profile of two bricks with a radial cooling channel in between (right row of scintillators, Fig. 5(b)).

The results shown in Fig. 5 do not include the background radiation arising from activation of the TMP itself or from the target monolith surrounding the detectors.

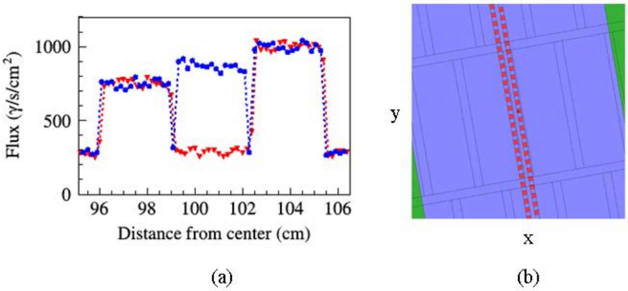

(a) (b)

Figure 5. (a) simulated gamma flux at the scintillators; (b) projection of collimator grooves onto brick structure (MCNPX geometry).

3.2. Image Reconstruction of Rotating Wheel

A simplified geometrical model is applied to simulate the recordings of the TIS during wheel rotation in order to design a suitable image reconstruction and error detection algorithm. The coding of the model is integrated in the ROOT framework [7], allowing to model the geometry, run the numerical simulation and perform the data analysis in a single package.

Two assumptions have been made:

1) The main contributing isotope to the gamma flux at the scintillators is ^{187}W, having a gamma line at 686 keV; hence attenuation in tungsten implies that the bricks seen from the scintillators' perspective can be approximated by a 2D grid, since only the top part of each brick is contributing to the imaged signal.
2) With the small solid angle acceptance of the collimator grooves, it is assumed that the trajectory of a detected gamma is normal to the target surface, thus neglecting blurring effects due to the variation in the emission angle.

To simulate wheel angular motion, the trajectory that a single collimator groove describes over the target wheel is considered. This trajectory is an arc and its angular span is determined by the gating scheme adopted (Fig. 6).

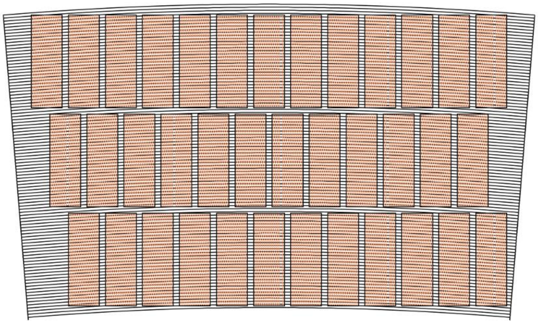

Figure 6. Brick layout in target wheel segment. Arcs represent the trajectory of collimator grooves.

In the simulations, the number of bricks is limited to three complete rows, located around the center of one wheel segment. All bricks are ascribed the same uniform neutron activation, hence neglecting variations of the gamma flux with respect to the target brick coordinates. Therefore, the gamma flux at the scintillators is simply proportional to the area within an arc that is covered by the bricks.

To mimic the statistical (Poisson) fluctuations observed by the detector a Monte Carlo calculation is performed for an average number of sampled points within each arc given by

$$N_{\mathrm{s}} = \phi T_{\mathrm{R}} \frac{\Delta\theta}{2\pi} A_{\mathrm{d}} \tag{2}$$

where ϕ is the mean photon flux at the scintillators, T_{R} is the total acquisition time, $\frac{\Delta\theta}{2\pi}$ is the fraction of wheel segment that is imaged, which is equivalent to the ratio of the gating time to the wheel rotation period, and A_{d} is the detector (scintillator) surface area. With a uniform sampling in the (r, θ) coordinate space, the average number of sampled points N_{s} per arc is constant.

Hence, for a specified data acquisition time (T_{R}), both photon yield at position of the scintillators as well as the statistical fluctuations are obtained in the Monte Carlo simulation.

4. RESULTS

In Fig. 7, three impurities are shown, corresponding to fragments of tungsten bricks present in the cooling channels. In Fig. 8(a), the result of the full-arc imaging of the wheel containing impurities is shown in the form of a 1D histogram of the number of photons reaching the scintillators during 2 days of data acquisition, while the image in Fig. 8(b) is the result of 40 days of data acquisition from a target wheel without impurities.

A mean photon flux of $\phi = 1000\ \gamma/\mathrm{cm}^2/\mathrm{s}$ was used, representative of the photon flux at the scintillator when positioned above one of the tungsten bricks, cf. Fig. 5(a). Full arc imaging is assumed, $\frac{\Delta\theta}{2\pi} = 68.5\ \mathrm{ms}/2.57\ \mathrm{s} = 0.0267$, where 2.57 s is the wheel rotation period, and $t_{\mathrm{g}} = 68.5\ \mathrm{ms}$ corresponds to the full arc gating time, Eq. (1). Finally, $A_{\mathrm{d}} = 0.01\ \mathrm{cm}^2$ is the scintillator cross section area. With a two days acquisition time, the average number of sampled points within an arc is $\mathrm{N_s} = 46000$, while, for 40 days, $\mathrm{N_s} = 920000$.

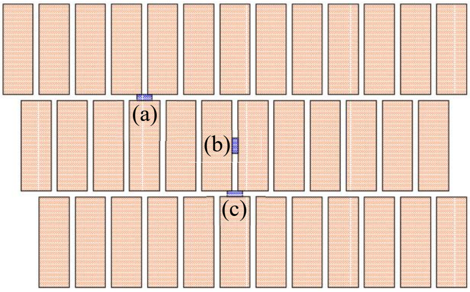

Figure 7. Target geometry containing three impurities (blue squares) within cooling channels.

By comparing the image in Fig. 8(a) with an image of a wheel segment without impurities (Fig. 8(b)), the location of the three anomalies may be observed, provided that they are visible over the inherent statistical fluctuations of the photon counts. In the present case, only the increased photon count associated with impurity (b) is visible. By increasing the data acquisition time, the fluctuations will be reduced relative to the signal associated with the anomalies.

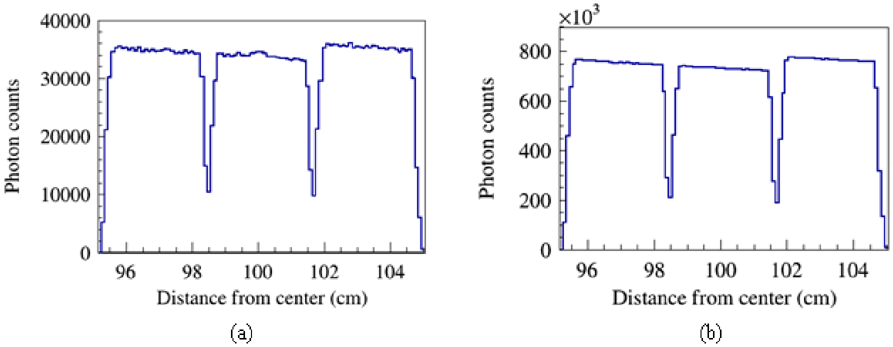

(a) (b)

Figure 8. Photon counts in scintillators (three anomalies); (a) 2 days of data acquisition; (b) 40 days of data acquisition.

The Pearson's χ^2 test is applied to compare the two images in Fig. 8(a-b). With a p-value of $p = 0.00173$, it is possible to conclude that the two images are not sampled from the same distribution, i.e. one of the images (Fig. 8(a)) shows the presence of anomalies. In Fig. 9, the normalized residuals provided together with the two images scaled to the same acquisition time clearly show the impurities marked with (a) and (c) in Fig. 7.

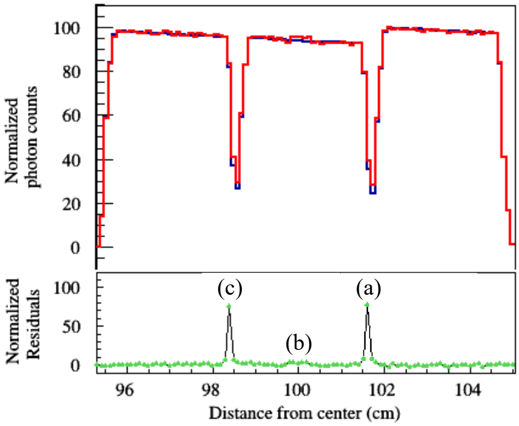

Figure 9. Normalized residuals resulting from the comparison of the image of the target containing impurities and the image of the ideal target.

5. CONCLUSIONS

The preliminary results presented in this paper support the feasibility of the TIS and indicate that the algorithm outlined for image reconstruction is capable of providing information on anomalies in the target wheel. Several simplifying assumptions were applied in this study:

- A simplified geometrical model was applied to simulate the detector response.
- All bricks were assigned a uniform activity distribution, therefore not taking into account gradients of the primary proton beam and neutron production.
- Activation in the steel shroud, as well as background stemming from neutron activation of surrounding components were not included.

A more comprehensive study, taking into account all of the above effects will lead to an increase in the required acquisition time for error detection.

In addition, the results presented in this paper are based on the simulated gamma flux at the scintillators, while the crystals' detection efficiency, the optical fiber efficiency and losses, and the characterization of the I-sCMOS camera should be taken into account to simulate the entire detection chain.

In a future study, it is planned to investigate the proposed error detection algorithm in detail. This will include 2D image reconstruction and statistical analysis intended for automated control of the camera gating scheme.

REFERENCES

1. S. Peggs (Ed.), "ESS Technical Design Report", *European Spallation Source ESS-doc-274*, April 2013.
2. N. Borghi, E.B. Klinkby, B. Lauritzen, E. Pitcher, N. Poolton, L. Zanini, "Development of a target imaging system for the European Spallation Source", *Proceedings of ICANS XXII*, Oxford, 27-31 March 2017, IOP Publishing, submitted.
3. J.L. Prince, J.M. Links, *Medical Imaging Signals and Systems*, 255-292, Pearson Education (2014).
4. N.D. Gagunashvili, "Comparison of weighted and unweighted histograms", *arXiv:physics/0605123v1*, May 2006.
5. D. Pelowitz (Ed.), "MCNPX User's Manual, Version 2.7.0", *Los Alamos National Laboratory LA-CP-11-00438*, April 2011.
6. W.B. Wilson et al., "A manual for CINDER90, Version 07.4.2 Codes and Data", *Oak Ridge National Laboratory LA-UR-07-8412*, March 2008.
7. R. Brun, F. Rademakers, "ROOT – An Object Oriented Data Analysis Framework", *Proceedings AIHENP'96 Workshop*, Lausanne, Sep. 1996, Nucl. Inst. & Meth. in Phys. Res. A 389 (1997) 81-86.

CHAPTER 4

The DTU prototype instrument

To study the feasibility of the TIS, a test setup was built at DTU. The construction took place over the course of 18 months and involved budget definition and management, mechanical design, provisioning of the mechanical and optical components, production and assembly of custom parts and deployment of the test setup to start operation. The first functionality tests were carried out from January to March 2018, followed by extensive measurements in November and December 2018. This chapter provides details of the manufacturing process, an overview of the software controls implemented for the test-rig operation and, finally, the characterization of the optical components. This last section of the chapter is covered by a publication submitted to Radiation Measurements.

4.1 Test-rig manufacturing

4.1.1 Target wheel

The test-rig target wheel is shown in Fig. 4.1; the wheel's backplane is made of 2 cm-thick aluminium and the resolution targets mounted on the outer edge are made of 4 cm-thick lead. Lead was initially cast into a mould, then the outer shape milled to specifications. Finally, the holes and figures were obtained by wire cut Electrical Discharge Machining (EDM). The layout of the resolution targets on the wheel surface is centrally symmetric to ensure a uniform weight distribution during target rotation.

The test-rig target wheel is designed uniquely for the TIS prototype instrument. Unlike the ESS target, where the tungsten bricks are the main source of radiation (emission radiography), the test-rig is based on the opposite principle, where a constant source is attenuated in correspondence of resolution targets to produce test patterns (transmission radiography).

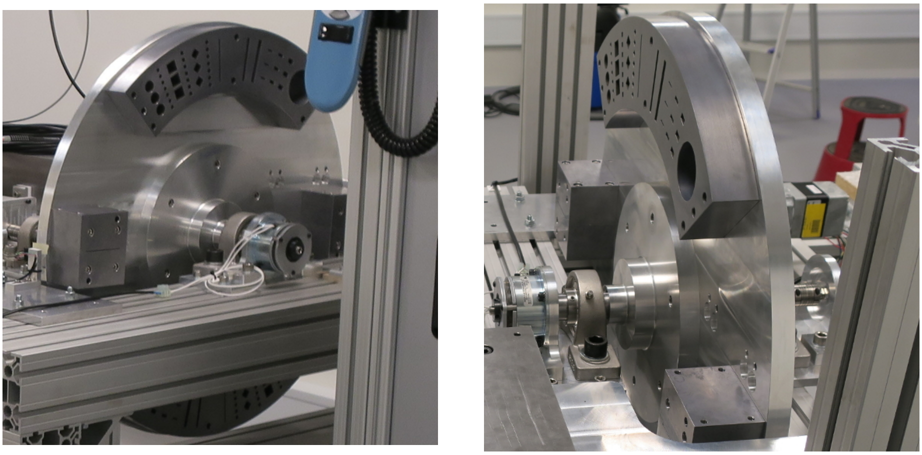

(a) (b)

Figure 4.1: Test-rig target wheel: front (a) and side (b) views. The lead resolution targets are mounted on the aluminium backplane and their layout is centrally symmetric to balance the weights during rotation.

The design of the resolution targets is presented in Fig. 4.2 and each shape serves a specific function:

- square shapes and slits (groups 2 and 3 on the picture), parallel and orthogonal to the wheel radius are intended to mimic the grid layout of the ESS tungsten bricks, corresponding to an undamaged target (Fig. 2.17 and Fig. 2.18(a));

- circles and diamond shapes (groups 1 and 4 on the picture) are instead designed to evaluate the achievable resolution with non-orthogonal features. This accounts for the condition in which debris or brick fragments are located within the grid layout at arbitrary angles.

The dimensions of the shapes in Fig. 4.2 are listed in Tab. 4.1.

The main wheel shaft (Fig. 4.3(a)), is supported by ball bearings and is independent from the motor shaft. This facilitates equipping the wheel shaft with a rotary encoder to monitor the wheel rotation and with an emergency electromagnetic friction brake for safety. The encoder chosen is a Bourns ENS1J-B28-L00256L with a resolution of 256 pulses per revolution.

The coupling of the wheel shaft to the motor shaft is achieved by means of a timing belt and the gear ratio chosen is 40 : 20 = 2. The motor chosen to drive the target unit is a Crouzet 80035512 (brushless, 5 Nm, geared). It is controlled by a Pulse Width Modulation (PWM) signal and it is capable of a maximum

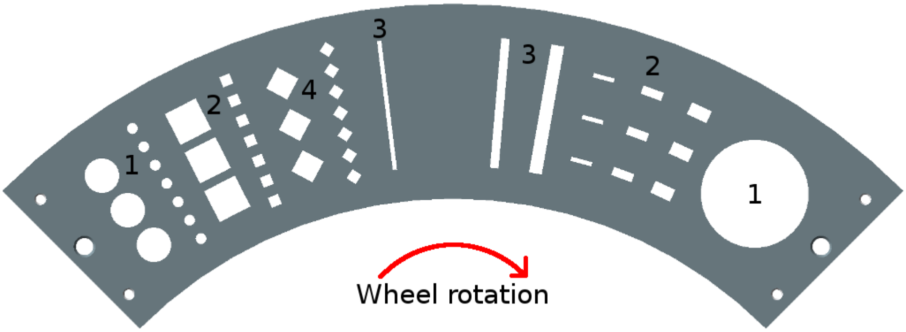

Figure 4.2: Test-rig target wheel: design of the resolution targets. The dimensions of the shapes are listed in Tab. 4.1 according to the numbering in the picture.

Table 4.1: Dimensions of test-rig resolution targets (Fig. 4.2).

Group	**Type**	**Quantity**	**Width×Length** (mm × mm)	**Radius** (mm)
1	Circles	1	-	50
		3	-	16
		7	-	5
2	Azimuthal slits	3	6 × 10	-
		3	4 × 10	-
		3	2 × 10	-
	Squares	7	5 × 5	-
		3	16 × 16	-
3	Radial slits	1	6 × 60	-
		1	4 × 60	-
		1	2 × 60	-
4	Diamonds	3	11 × 11	-
		7	5 × 5	-

56 rpm speed. Given the gear ratio, this corresponds to a maximum achievable wheel speed of 28 rpm.

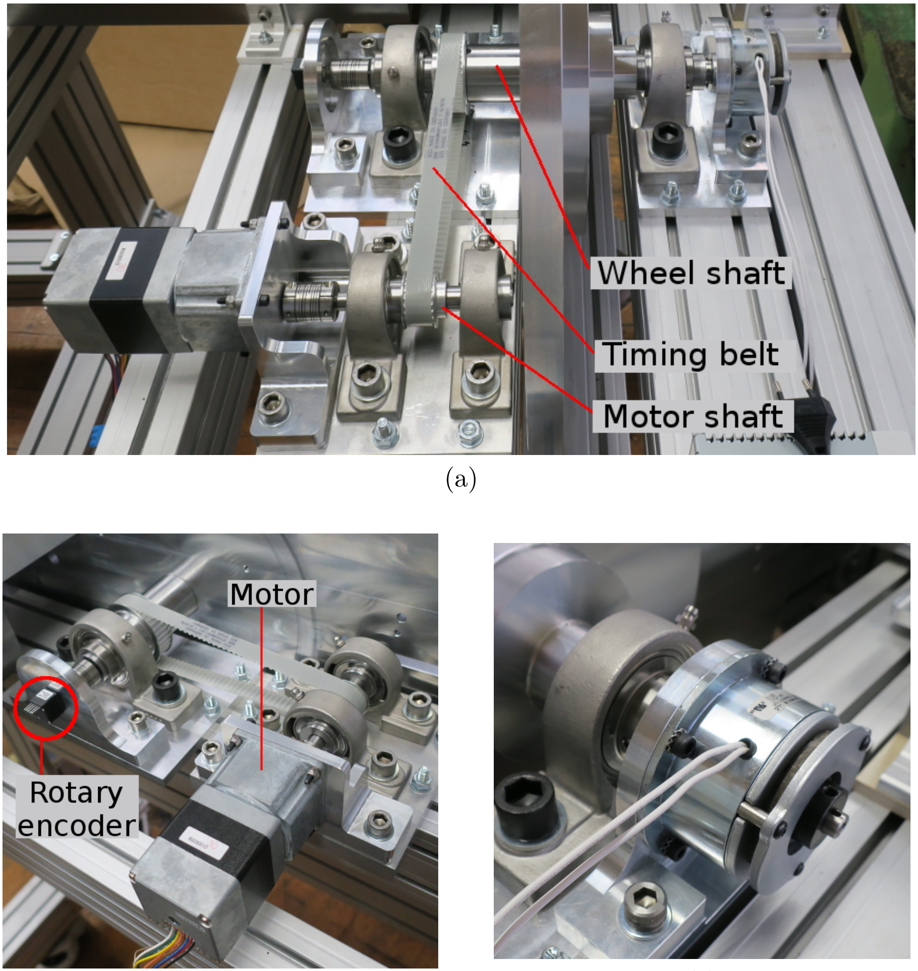

(a)

(b)

(c)

Figure 4.3: Detail of the target unit assembly. The wheel and motor shafts (a) are coupled by means of a timing belt. The wheel shaft is equipped on one end with a rotary encoder (b) and on the other end with an electromagnetic friction brake (c).

4.1.2 Collimator block

The collimator block is composed of three separate parts, as shown in Fig. 4.4(a): the top and bottom blocks, containing the collimator grooves, are separated by a 1 mm thick steel sheet. The material for the collimator is tool steel (EBI 1730 DIN C45U) [70]. A total of 60 grooves are machined to a precision of 50 μm over the 2 m collimator length. In Fig. 4.4(a), the layout of the two sets of grooves (1 mm and 0.5 mm) is shown. The red frame highlights the subset of grooves used for the measurements presented in Chapter 5 and the numbering of the grooves corresponds to the channels in the reconstructed images discussed in Chapter 5.

Along the sides of the bottom collimator block (Fig. 4.4(b)), two larger grooves with a 1 cm^2 cross section are machined for laser alignment to the ^{60}Co source.

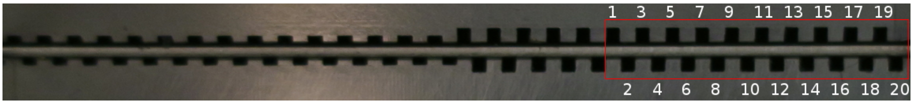

(a)

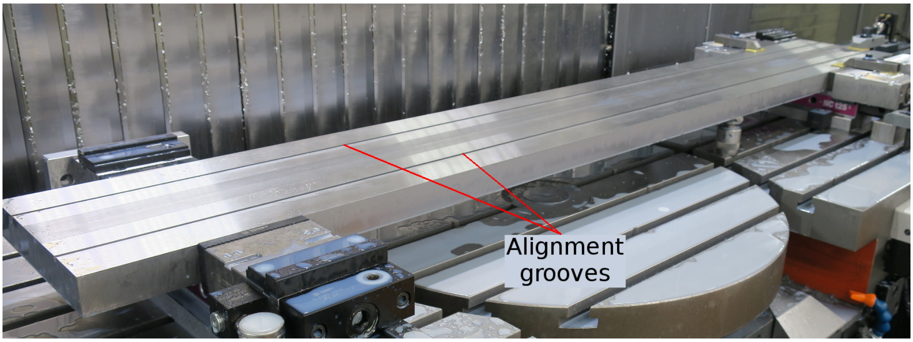

(b)

Figure 4.4: Collimator block. The 60 grooves (a) are laid out in two groups of 30 to provide different radial spatial resolutions. For the test-rig operations presented in Chapter 5, a subset of 20 (1×1 mm^2) was used, as indicated by the red frame in (a). Channels are numbered according to their radial coordinate in the reconstructed images. Two 1×1 cm^2 grooves (b) were machined to allow alignment to the ^{60}Co source.

4.1.3 Scintillator cartridges and cartridge holder

The coupling of the scintillator cartridges (Fig. 4.5(a)) to the collimator block was achieved by means of an aluminium holder, shown in Fig. 4.5(b), fixed to the end of the collimator. The cartridge support replicates the cross section profile of the scintillator cartridge to ensure alignment (Fig. 4.5(c)). Two screws are used to stabilize the cartridge within the holder.

The scintillator cartridges are a key component in the TIS optical chain. They must ensure the alignment of the crystals to the collimator grooves and, additionally, provide a mechanically stable support to the crystal-fiber coupling.

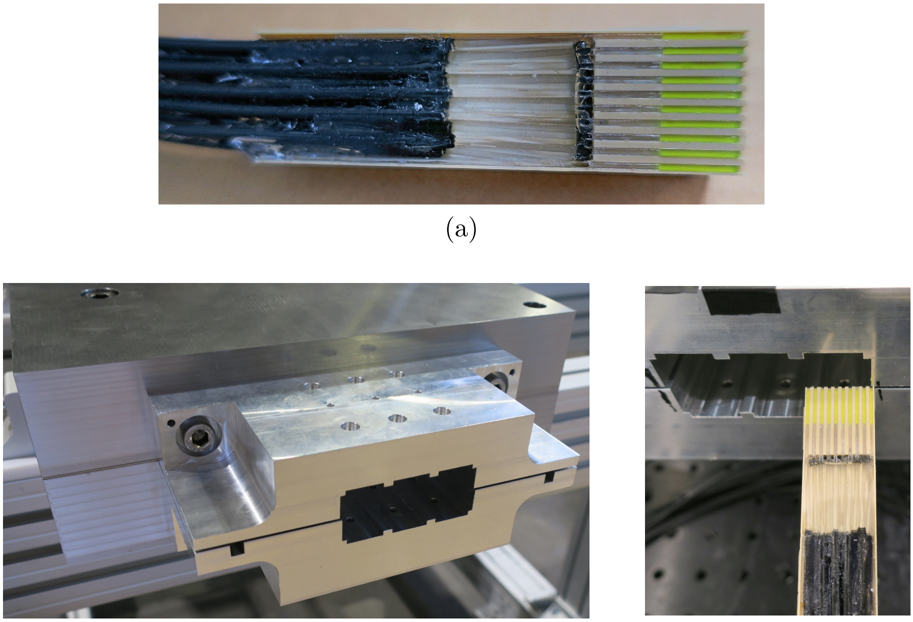

(a)

(b) (c)

Figure 4.5: Detail of the scintillator unit: cartridge fully populated with 10 scintillators and fibers (a); cartridge support block attached to the collimator (b); insertion of cartridge in the dedicated slot (c).

For the test instrument, Poly(aryl Ether Ether Ketone) (PEEK) was chosen as the cartridge material, thanks to its mechanical strength and temperature resistance [71, 72]. However, its radiation resistance under mixed neutron and gamma fields has not been investigated.

Crystals and fibers have been glued together and to the cartridge. The gluing process is a critical step in the cartridge assembly and has not been optimized for large scale production. The crystal-fiber coupling has been achieved with Norland 61 optical glue, whereas a transparent epoxy was used to secure the fibers to the PEEK support. In this case, transparent epoxy has been chosen to allow visual quality inspection of the joints and light tightness has been achieved by sealing all the openings in the cartridge holder (Fig. 4.5(b)) with aluminium foil and black tape. Measurements with the test-rig have been conducted in a dark room to minimize stray light leaking into the fibers.

4.1.4 Supporting frame

The collimator block, the target wheel and all the mechanical components are assembled on a frame built from commercially available aluminium elements (Kanya MA1-2 and MA2-5 extruded profiles). The support structure of the test-rig, designed to carry loads in excess of 1 ton with negligible deformation of the collimator blocks, is shown in Fig. 4.6.

Figure 4.6: Aluminium test-rig structure.

In Fig. 4.7, the test-rig deployed in front of the ^{60}Co source is shown.

4.1.5 Optical fiber connections

The ESS target monolith will be operated under high vacuum conditions (0.1 – 0.01 Pa). For this reason, together with maintenance flexibility, the optical fibers from the crystals to the camera cannot be laid out as uninterrupted 20 m long cables. At least two splitting points are envisaged for the final TIS: one at the monolith interface, to comply with the vacuum requirements and one close to the camera, to facilitate deployment and maintenance operations.

Figure 4.7: Test-rig deployed in front of the ^{60}Co source.

It is estimated that a dry coupling between two polished fibers induces light losses of about 20% per connection [73]. To investigate the effect of these losses on the overall test-rig performance, two patch panels with SMA connectors were built (Fig. 4.8)

The 20 m long fibers were split in three pieces:

- 1 m long leads attached to the collimator cartridges;
- 18 m long fiber patch cables terminated at both ends with SMA connectors;
- 1 m long leads attached to an aluminium holder providing support for the fiber imaging.

4.1.6 Fiber holder matrix

In Fig. 4.9, the technical details of the aluminium holder for the optical fibers are shown. The fibers are arranged in a 8×8 matrix and the separation between them is limited by the thickness of their jackets.

Firstly, fibers are exposed from their jacket, then glued to the aluminium support. Once the holder is populated, fibers are cut flush to the support's surface and polished to ensure uniformity in the light emission. The holder is inserted in an aluminium barrel fixed to the camera lens (Fig. 4.10).

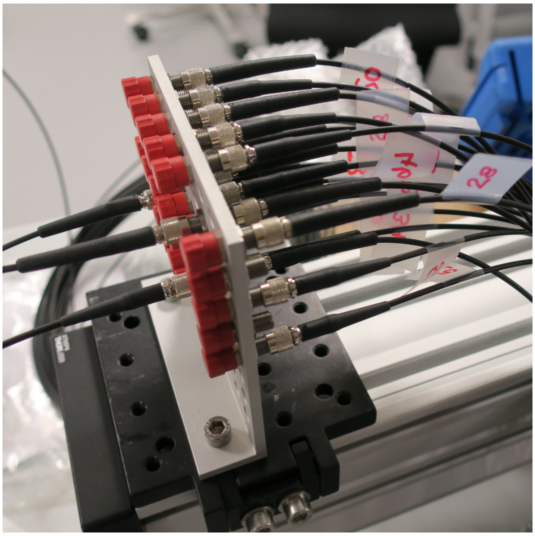

Figure 4.8: Fiber patch panel populated with 20 SMA connectors. Two identical panels were used to test the effect of fiber connections on the signal degradation.

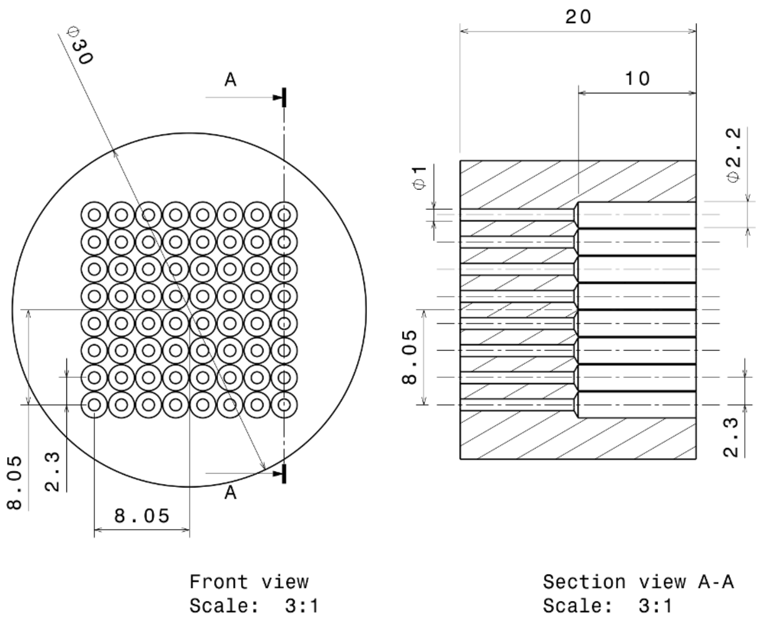

Figure 4.9: CAD drawing of the fiber matrix holder. The surface density is maximized (left) and limited by the diameter of the optical fiber jackets, which are also inserted in the holder (right) to provide structural support.

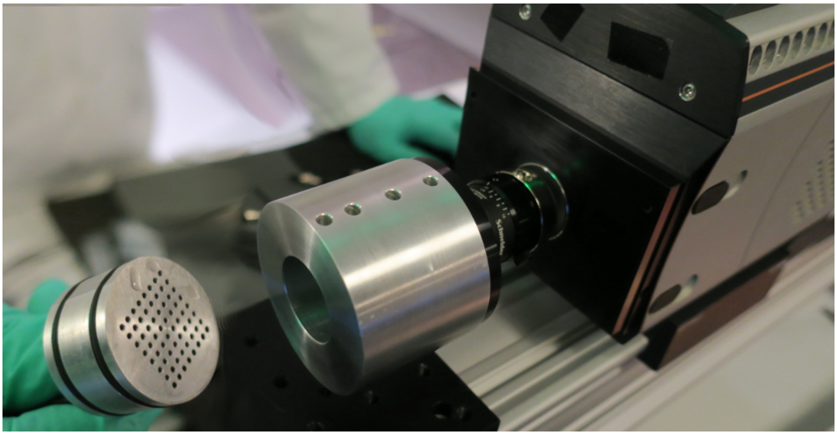

Figure 4.10: Fiber holder coupled with camera optics: the barrel, attached to the camera optics, is light tight and grub screws are used to hold the matrix adapter in position.

The test-rig was operated with 20 channels out of the 60 available, hence the matrix is only populated at the center. The full scale TIS will require to accommodate 500 optical fibers, thus requiring the re-design of the holder to increase the density of fibers per cm^2.

4.2 Test-rig and camera software controls

The test-rig is instrumented to allow remote control and monitoring during data acquisition. The control software was developed in G, the graphical programming language adopted by the LabVIEW platform.

The software allows to control the motor for the target wheel and to receive trigger signals from it, which are relayed to the I-sCMOS camera for further processing.

A Software Development Kit (SDK) for LabVIEW is also available from the camera manufacturer. This would allow to design a fully integrated system for controls and data acquisition. However, the ESS system integration requirements do not allow LabVIEW as an instrument control platform and, therefore, require new control software to be developed.

A test was carried out to investigate the high-speed capabilities of the I-sCMOS camera intensifier. As discussed in Chapter 3, the intensifier will also be used as an optical switch to prevent light from the prompt spallation background to reach the sCMOS chip. Moreover, two acquisition modes based on different gating schemes are envisaged. In both cases, it is crucial to achieve μs accuracy in the intensifier operations.

Indeed, depending on the settings, the sCMOS chip is not designed for high frame rate operations and it can achieve frame rates between 15 and 20 fps. In the case of the ESS TIS, however, continuous full resolution acquisition would require a frame rate of at least 3000 fps.

The intensifier, however, is capable of on/off switching times of the order of 10 ns, hence it offers a great gating flexibility. While operating the camera at a low frame rate, the intensifier can be controlled independently up to a 0.1 μs precision.

In the example shown in Fig. 4.11, the frame rate is very low, about 7 fps. Frame #1 (light blue line) is maintained open for 68.5 ms, i.e. the time required to scan an entire ESS target sector. The chip is left unexposed for the following 71.4 ms before starting frame #2, thus leaving one full sector in between two frames.

During the first exposure (frame), the intensifier is switched on and off for three increasingly long intervals (yellow peaks correspond to the switching signals and green lines indicate the intensifier status). The light from the camera photocatode (i.e. from the optical fibers) can only reach the chip during these time intervals, thus allowing for fine control of the gating profile.

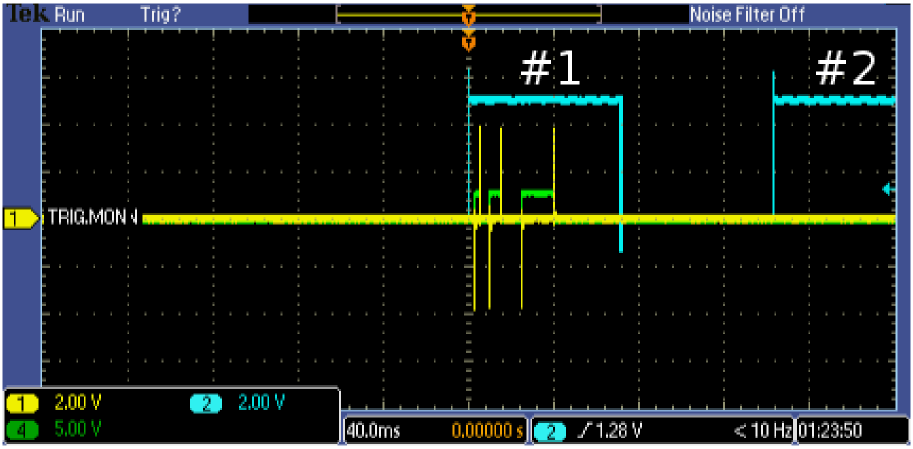

Figure 4.11: High-speed intensifier controls (oscilloscope signal analysis). The sCMOS chip is operated at low frame rates (open frames correspond to light blue lines). Two 68.5 ms frames are opened and separated by a 71.4 ms interval. During frame #1, the sCMOS chip is only exposed to light during the intervals when the intensifier is open (green lines). The yellow peaks represent the open and close signals sent to the intensifier.

4.3 Characterization of optical components

The test-rig is intended to provide a versatile platform to test components, materials and data analysis techniques in preparation for the construction of the final TIS instrument.

Components, such as the scintillator crystals, the optical fibers, the camera lenses need to be thoroughly investigated to understand their performance under conditions relevant to the ESS.

The publication presented in this section has been submitted to Radiation Measurements. It allows to identify a set of suitable components used for the rig operations. Moreover, the results found in this study provide a baseline configuration to be used as a comparison term for future research and development.

The investigations discussed in the paper are based on a sample of three different scintillator materials, namely LuAG:Ce, YAG:Ce and BGO. An extensive literature search has been conducted to identify the most suitable crystals for the TIS and the decision to test BGO as a reference, compared to YAG:Ce and LuAG:Ce is based on references [74–86].

Characterization of optical components for the ESS Target Imaging System

N. Borghi[a,*], B. Lauritzen[a], L. Lindvold[a], N. Poolton[b]

[a] *Technical University of Denmark (DTU), Frederiksborgvej 399, 4000 Roskilde, Denmark*
[b] *Camlin Photonics, 31 Ferguson Drive, Lisburn BT28 2EX, Northern Ireland*

Abstract

At the European Spallation Source (ESS), a Target Imaging System (TIS) has been proposed to monitor the integrity of the target wheel. The TIS signal will be provided by the gamma decay photons from the activated tungsten bricks of the target. To collect the photons, a linear array of 500 scintillators is mounted on a collimator and the imaging is achieved via a *push-broom* method. Scintillation light will be carried by optical fibers to an intensified sCMOS camera.

This study presents a characterization of the performance of the full detector chain: emission from crystals, attenuation in optical fibers and response of the camera optics. The behaviour of both unirradiated and irradiated optical fibers is also evaluated for γ-only irradiations up to 15 kGy.

Among the tested crystals (LuAG:Ce, YAG:Ce and BGO), LuAG:Ce is the preferred choice both in terms of radiation hardness and photon yield.

Losses induced by Poly methyl methacrylate (PMMA) and quartz optical fibers are $\sim$ 65% and $\sim$ 45%, respectively. In ESS conditions, over half-year of continuous operations, PMMA fibers are estimated to lose an additional 3%, compared to 2% for quartz fibers. Both PMMA and quartz fibers represent a potentially viable choice: the former suffer a more serious radiation damage than the latter, but formation of permanent defects in quartz can impair the efficiency of quartz fibers in the $580-620$ nm range. Mix-and-match of PMMA and quartz fibers may represent a cost-effective compromise for the final TIS design.

Two different fibers-camera coupling optics are compared. The measured difference in transmittance is 3%.

Keywords: target imaging system, gamma camera, optical fibers, inorganic scintillators
2010 MSC: 00-A79

---

[*] Corresponding author
Email address: `nicbo@dtu.dk` (N. Borghi)

Preprint submitted to Radiation Measurements *July 29, 2019*

1. Introduction

At the European Spallation Source (ESS) an intense flux of neutrons is produced by means of a 2 GeV proton beam impinging on a rotating target wheel, as shown in Fig. 1a. The target wheel (Fig. 1b) comprises ∼ 7000 tungsten bricks arranged in a grid-like structure with narrow spacing to allow for the flow of cooling helium. The bricks are encased in a 10 mm thick steel vessel forming the outer structure of the wheel [1].

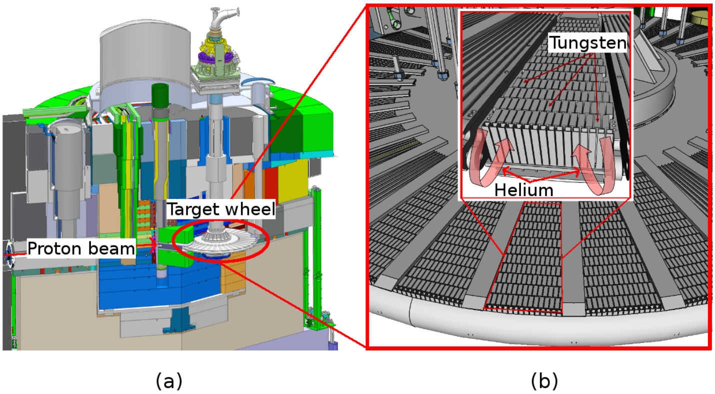

Figure 1: The ESS target station (a) comprises the target wheel which contains a total of ∼ 7000 tungsten bricks serving as the spallation target (b); the insert in (b) shows the flow of the helium gas coolant [1].

To monitor the integrity and possible faults occurring in the target wheel during operation, a Target Imaging System (TIS) is proposed [2]. The TIS is intended to perform high-resolution imaging of the target brick structure by detecting decay gamma photons from the activated tungsten bricks that will be able to penetrate the steel shroud. The TIS consists of a steel collimator matched to a 1D radial array of scintillators. These are individually coupled with optical fibers to an Intensified sCMOS (I-sCMOS) camera; 2D imaging is achieved in push-broom manner through target wheel rotation. The image intensifier of the I-sCMOS allows for the fast gating required for high-resolution imaging of the ESS target wheel [3]. By means of the optical fiber network, comprising a total of approx. 7 km of optical fibers, the radiation-sensitive I-sCMOS camera can be located remotely from the intense radiation field inside the target monolith.

A prototype TIS has been developed at the Technical University of Denmark (DTU) to investigate the feasibility of the final design intended for ESS. This test-rig has been constructed as a platform to assess different design solutions, materials and manufacturing processes. The prototype TIS offers different options for collimators, optical components (scintillators, fibers and optics), optical readout as well as target wheel geometry. The optical components are characterized in terms of the light yield from the scintillator crystals and the spectral transmission properties of the optical fibers. Measurements are carried out before and after irradiation to examine the possible degradation of the TIS optical components in a harsh radiation environment.

In Section 2, an overview of the test-rig's features is given. Section 3 deals with the study of the optical properties of scintillators, fibers and camera optics in a radiation-free condition. In Section 4, the effects of γ-only irradiation are studied for the optical fibers in order to complement the results of Section 3.

2. Test-rig

The test-rig has been developed as a flexible prototype TIS (Fig. 2); it is placed in front of a medical ^{60}Co source (365 TBq), normally used for fundamental dosimetry research. Different transmission signal patterns can be obtained by means of a rotating wheel (Fig 2b) equipped with lead resolution targets and positioned in between the gamma source and the collimator. Unlike the TIS intended for the ESS, images in the test-rig are based on gamma transmission rather than gamma emission.

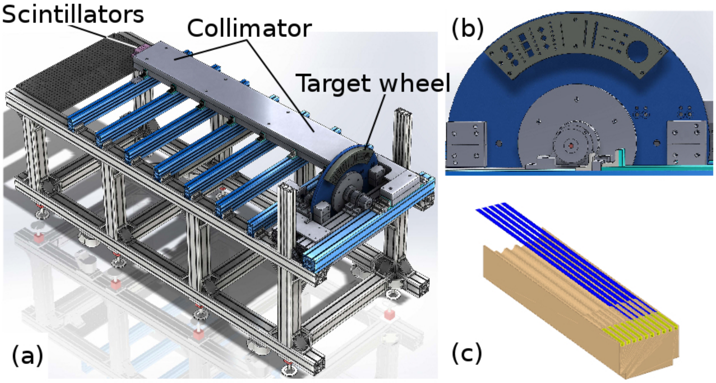

Figure 2: (a) Test-rig with collimator and target wheel; (b) target wheel with lead resolution targets; (c) scintillator cartridge with detail of scintillator crystals (green) and optical fibers (blue).

The prototype comprises (i) a collimator, (ii) optical components and (iii) a data acquisition system. By functional necessity, the collimator length of the DTU TIS prototype and the final ESS TIS will be about the same, as will be the size of scintillators and groove dimensions. Because of the relatively small radiation field produced by the ^{60}Co test source (2 cm width), there are fewer readout channels in the prototype. Briefly, the prototype has:

i) A 2 m long collimator precision milled to 50 μm with a total of 60 square collimator grooves (30 1×1 mm^2 and 30 1×0.5 mm^2) to allow imaging with different spatial resolutions. The final version of the TIS will have approximately 500 grooves, all with identical cross-section areas; the size of these will be determined from experiments on the DTU test-rig.

ii) Optical components including scintillator cartridges, optical fibers and camera optics.

   a. Six cartridges, each containing 10 scintillator crystals individually glued to 1 m long PMMA optical fibers terminated with SMA connectors (Fig. 2c). All sides of the crystals have been optically polished. As scintillators, $1 \times 1 \times 10$ mm^3 LuAG:Ce, YAG:Ce and BGO crystals are used (see Table 1 for comparison with other materials; green emission and short attenuation length are considered as key parameters in the choice of scintillator) [4]. Critical to the cartridge performance are the mechanical stability of the scintillator-fiber glue coupling, which can impair optical transmission if damaged, and the efficiency of the scintillator light collection by the fiber leads. Also, the assembly process of the cartridges should be optimized for reproducibility. Cartridges have been machined in Poly ether-ether-ketone (PEEK) for good radiation resistance and mechanical stiffness.

   b. 20 m long optical fibers with SMA connectors, connecting the cartridges to the camera optics. For the ESS TIS, about 7 km of optical fibers will be used, making the cost/performance ratio a critical figure. As optical fibers, PMMA (1 mm core diameter, black polyethylene jacket, attenuation < 0.20 dB/m, Numerical Aperture N.A. = 0.50, fluorinated cladding) and quartz (Thorlabs Multimode FP600URT, N.A. = 0.50, 600 μm core diameter) fibers are applied. A combination of quartz and plastic fibers may also be considered.

   c. Two different systems are considered for the camera optics: a compact VIS-NIR lens from Schneider (31.5 mm diameter, 10 mm focal length, aperture f/1.9 f/22) and a custom assembly based on Thorlabs and Edmund Optics components (aspheric condensers, 75 mm diameter, 60 mm and 50 mm focal lengths).

iii) Data acquisition achieved with an Andor iStar sCMOS camera. The image intensifier of the camera can be used for fast gating (10^{-9} s) and is used as a shutter in the present application (on/off contrast 1:10^{-8}). At the test-rig, the gating is synchronized with the rotation of the target wheel in reference to a zero position, defined by a fast opto-switch located on the wheel's rim. Hence, portions of the wheel can be selectively monitored. Data can be accumulated from each of the 60 readout channels and mapped to planar coordinates of the wheel [3]. Software has been developed to integrate the camera operations with the test-rig controls and to perform the image reconstruction.

Table 1: Properties of selected scintillator materials ([(a)] Data from Crytur [5]; [(b)] Data from Saint-Gobain [6]; [(c)] Attenuation length for 500 keV photons; data from NIST [7]).

Scintillator material	Density (g cm^{-3})	Attenuation length[(c)] (cm)	Refractive index	Photon yield (MeV^{-1})	Peak wavelength (nm)	Decay constant (ns)	Relative cost
LuAG:Ce[(a)]	6.73	1.3	1.84	2.5×10^4	535	70	$$
YAG:Ce[(a)]	4.57	2.5	1.82	3×10^4	550	70	$$
BGO[(a)]	7.13	1.1	2.15	8×10^3	480	300	$$
BCF-60[(b)]	1.05	10.2	1.60	7×10^3	530	7	$
LaBr3:Ce[(b)]	5.08	2.3	2.30	6.3×10^4	360	16	$$$

3. Characterizing optical components

The characteristics of crystals, fibers and camera optics are assessed in a no-radiation context; individually and combined in the full readout chain, from scintillator to sCMOS camera.

3.1. Scintillator photon yield

The three different scintillator materials (BGO, LuAG:Ce and YAG:Ce) supplied by Crytur are compared. Five samples of each material are individually placed into the COLUR instrument (Risø station for CryOgenic LUminescence Research), a modified Horiba spectrofluorometer consisting of [8]:

i. Horiba spectrofluorometer (Fluorolog-3) modified to include cryogenic sample cooling (7 – 295 K, not used in this work).
ii. Hamamatsu R-928P PMT coupled to an emission monochromator for high-sensitivity photon counting. Spectral correction applied in the range 290 – 850 nm.
iii. Miniature Moxtek X-ray source (40 kV anode voltage, 100 mA anode current).

The integration time was set to 500 ms, whereas the exposure to X-rays was not timed. The measurements were carried out in high vacuum conditions (0.1 – 0.01 Pa).

The curves in Fig. 3 (left) represent the radioluminescence (RL) spectra of the selected crystal materials. The ∼10% spread characterizing all the measurements is within the experimental uncertainties associated with the particular use of the COLUR instrument. When irradiated with 40 kV X-rays, LuAG:Ce and YAG:Ce exhibit comparable photon yields. At this energy, the attenuation lengths of the crystals are of the order of $10^{-3} - 10^{-2}$ cm, much smaller than the crystals size, implying almost total absorption of the X-rays.

For ESS conditions, where the gamma energies are of the order of 700 keV (main signal from ^{187}W at 686 keV), the photon attenuation lengths are comparable to the crystal size (cf. Tab. 1) [7] and total absorption no longer applies. A Monte Carlo simulation of the energy deposition in the crystals is performed [2, 9, 10, 11]. The simulation includes all the isotopes produced in

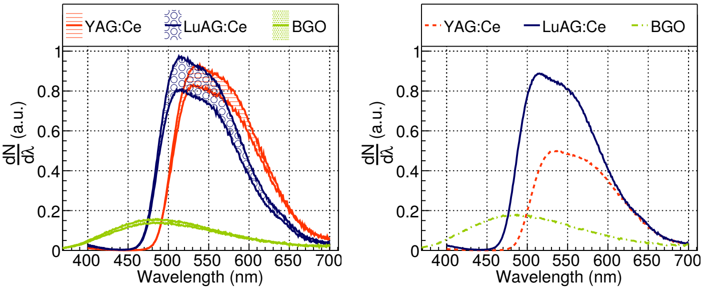

Figure 3: Radioluminescence spectra from crystals: total absorption (left); under ESS conditions (right). Spectra are normalized to the maximum spectral intensity of LuAG:Ce.

the target wheel during the spallation process. The calculated energy deposition for a single crystal in the center of the scintillator block for the LuAG:Ce, YAG:Ce and BGO is 2.02 MeV/s, 1.16 MeV/s and 2.44 MeV/s, respectively. As Fig. 3 (right) shows, the LuAG:Ce photon yield is the largest, whereas the longer attenuation length of YAG:Ce results in a much smaller photon yield. Despite the higher density of BGO, which is reflected in the larger mean energy deposition from the gammas, its photon yield is ~ 30 times smaller than that of LuAG:Ce, resulting in a less intense photon emission. Therefore, LuAG:Ce allows for the most compact design of the scintillator cartridges, as it matches a short attenuation length with a high photon yield.

3.2. Optical fibers

The attenuation $A(\lambda)$ in the optical fibers is measured with the so-called *cut-back method*: transmission (T_l) of white light from an Ocean Optics HL-2000 halogen lamp is measured in a 20 m long fiber by an Ocean Optics QE65000 CCD spectrometer and repeated (T_s) for a fiber shortened to 2 m without changing the optical coupling to the light source. The white light source is filtered with a metallic neutral density filter to prevent the saturation of the spectrometer. The The fibers were terminated at both ends with SMA connectors to allow stable and reproducible coupling to the spectrometer. The spectrometer readings were corrected for spectral efficiency as well as electrical and dark noise. From the ratio between the two measurements the attenuation in dB/m is obtained as $(\Delta L = 18\ \text{m})$:

$$A(\lambda) = \frac{-10 \times \log_{10}\left(\frac{T_l(\lambda)}{T_s(\lambda)}\right)}{\Delta L} \tag{1}$$

The attenuation for both PMMA and quartz fibers is shown in Fig. 4.

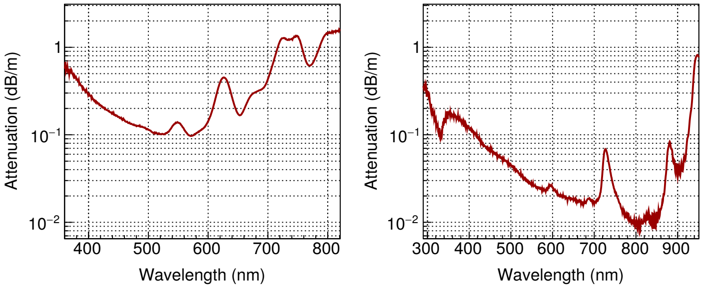

Figure 4: Attenuation (dB/m) in plastic fiber (left) and quartz fiber (right).

3.3. Optics and camera photocatode

The commercial Schneider VIS-NIR Cinegon 1.9/10 lens and a custom assembly built with two aspheric condenser lenses (Thorlabs ACL7560U-A and Edmund Optics 46-244)

The quantum efficiency (Q.E.) of the Andor I-sCMOS intensifier photocatode is shown in Fig. 5 (blue, long-dashed line) [12], together with the response functions of the Schneider lens (left, orange, dashed line) and a single aspheric lens (left, green, solid line). Either the Schneider or the custom optics will be coupled to the camera. Fig. 5 (right) shows the resulting response function of the optics and camera photocatode.

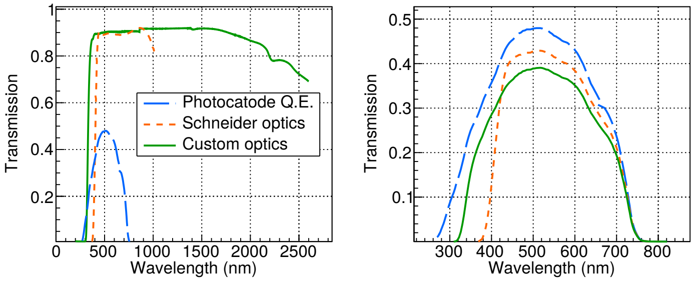

Figure 5: Relative transmittance of fiber-to-camera coupling optics: individual components (left) and combined performance (right) [12, 13, 14, 15]. In the right figure, the photocatode Q.E. (dashed blue line) is shown for reference.

The overall response of the custom optics is 3% lower than that of the Schneider assembly, which also exhibit a sharp drop in transmission around 400 nm.

This feature is not expected to affect the transmission of any of the three scintillators considered in this study, which all have emission peaks above the 400 nm cut-off.

For the TIS at ESS, the need for imaging a large number of optical fibers (500 fibers arranged in a matrix layout) will affect the final design. From this perspective, the larger diameter of the custom optics may result in a better signal collection.

3.4. Degradation of scintillator signal

To evaluate the response function of the whole light chain, it is necessary to convolute the initial scintillator spectra (Fig. 3) with the attenuation due to the optical fiber and to the camera optics. This allows to compare the different options under ESS-relevant conditions.

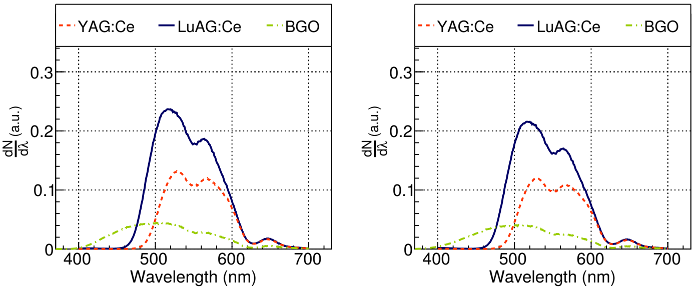

Figure 6: Total response function: attenuated crystal photon yields under ESS conditions (PMMA fiber, no radiation damage): Schneider optics (left); custom optics (right).

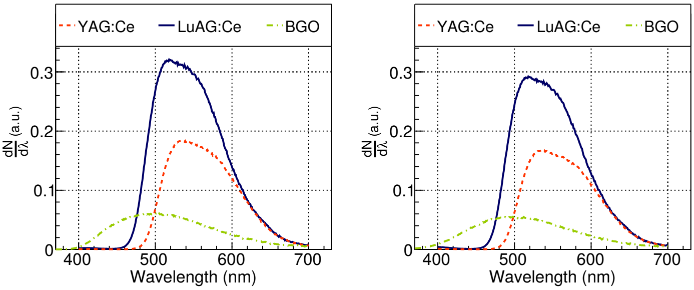

Figure 7: Total response function: attenuated crystal photon yields under ESS conditions (Quartz fiber, no radiation damage): Schneider optics (left); custom optics (right).

The emission spectra in Fig. 3 are normalized to the maximum spectral intensity of LuAG:Ce, and the resulting spectra for plastic and quartz fibers are reported in Fig. 6 and Fig. 7, respectively. The plot on the left is for the Schneider optics, whereas the one on the right is for the custom assembly. As anticipated, the 400 nm cut-off is not affecting the collection of light in the camera and the higher attenuation of the custom optics results in a 3% loss in the intensity of photons reaching the sCMOS.

The TIS measurements will not provide spectral resolution. It is therefore more relevant to compare the integral photon yield from the three crystals. For the BGO and the YAG, the photon yield integrated over the wavelength is comparable and both around 50% lower than the LuAG integrated photon yield.

4. Tests under gamma irradiation

In the final TIS installation, the initial 2-3 m of optical fibers attached to the scintillators will be embedded into the ESS target monolith. The calculated dose rate at $Z = 2.9$ m above the target wheel is $\lesssim 0.1$ Gy/h (Fig. 8). One year of ESS operations comprises a total of 5400 h of beam on target, subdivided in two phases of 2700 h each interleaved by 1680 h of stop. This results in a total dose rate of 540 Gy at $z = 2.9$ m over one year of operations.

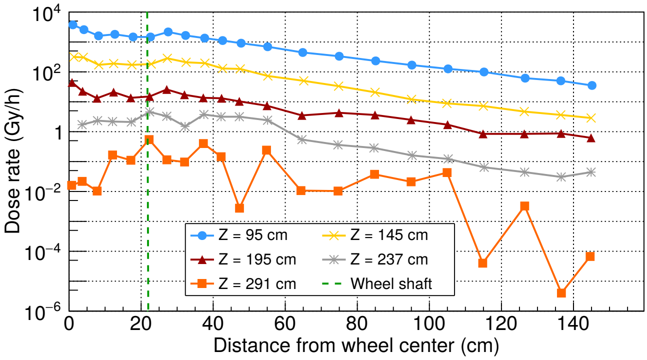

Figure 8: Dose rate in Target Monitoring Plug (TMP) evaluated at different elevations (Z) from the target wheel surface and at an angle $\varphi = 12°$ with respect to the proton beam axis. The vertical green dashed line represents the radius of the wheel shaft. [16].

In Fig. 9, the degradation of the fiber transmission is shown for plastic and quartz fibers, respectively. Fibers were irradiated in a ^{60}Co gamma cell with a dose rate of 6.5 kGy/h and transmission measurements performed for accumulated doses up to 15 kGy. For both PMMA and quartz fibers, a total length of 15 m was exposed to the radiation field. In the $500 - 550$ nm region, where the maximum emission from LuAG:Ce is observed, the light transmission in plastic fibers degrades more rapidly than in the radiation resistant quartz fiber. Compared to Fig. 4, the overall attenuation of both PMMA and quartz fibers is larger after irradiation. However, only the $300 - 700$ nm wavelength range exhibits a dose dependent behaviour.

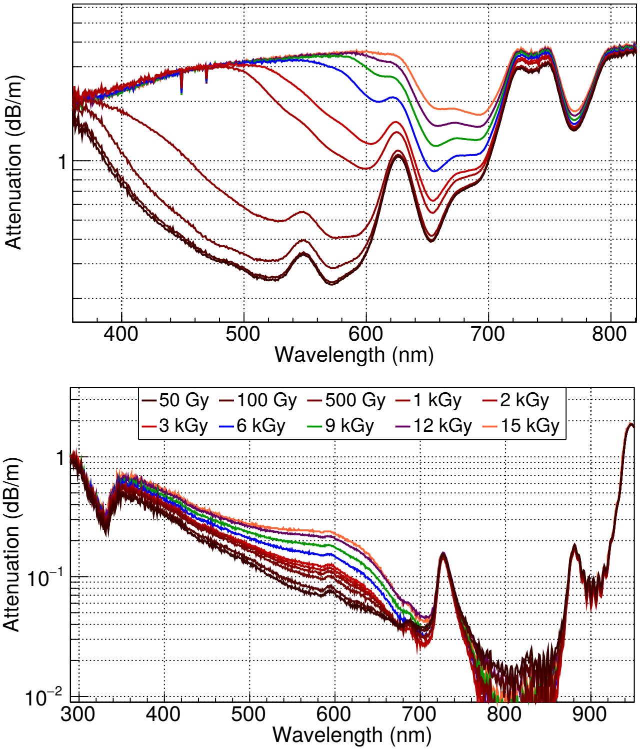

Figure 9: Attenuation (dB/m) for increasing accumulated doses in PMMA (top) and quartz (bottom) fibers. Note the different scale on the two figures, with the quartz fibers having overall a lower attenuation than the PMMA fibers. The legend showing the accumulated doses applies to both figures.

The spectra obtained for LuAG:Ce (Fig. 6) are folded with the response function of the irradiated fiber (Fig. 9) in order to estimate the overall performance degradation. The resulting spectra are plotted in Fig. 10 (PMMA on the left, quartz on the right). For PMMA fibers, the radiation-induced damage results in a 3% loss in the total transmittance after 250 Gy, which correspond to half-year of ESS full-power operations. For the same accumulated dose, the damage in quartz fiber is 2% (Fig. 10 (right)).

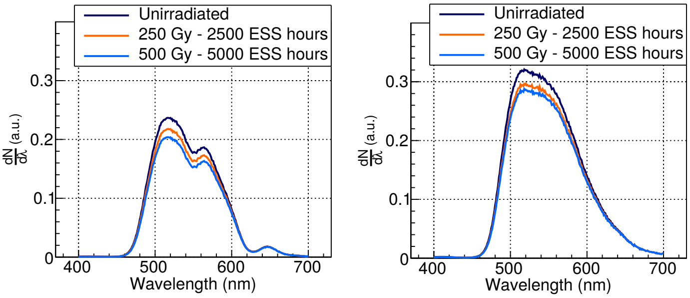

Figure 10: Degradation of signal transmission at ESS irradiation conditions (half-year and one year equivalent dose): signal in PMMA fiber (left) and in quartz fiber (right).

As mentioned in Section 3, the TIS measurements will not provide spectral resolution. The integrated photon yields as a function of the accumulated dose are shown in Fig. 11. Under ESS conditions, 500 Gy correspond to 1 year of operations. The integral photon yield is reported up to 10 years of operations.

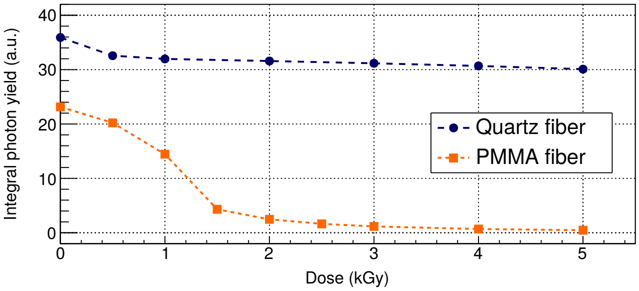

Figure 11: Integral of photon yield as a function of dose: 1 year of ESS operations corresponds to 500 Gy of accumulated dose. The quartz (blue, top) and PMMA (orange, bottom) curves are shown for doses up to the equivalent of 10 years of operations.

In addition to the initial difference between quartz and PMMA fibers (0 Gy), the degradation of PMMA fibers is significant over the first 2 years, corresponding to 1 kGy and causes an almost total loss of signal after the 5 years of expected target lifetime (2.5 kGy). Overall, quartz fibers exhibit less damage from prolonged irradiations than plastic fibers.

A localized increase in the $500 - 700$ nm for quartz fibers is observed, suggesting the formation of a defect in the semi-crystalline structure of quartz. To investigate this, a function $Y(\lambda, D)$ is defined as the logarithm of the measured spectral photon intensity for different accumulated doses. The first derivative $\frac{\partial Y}{\partial D}(E)$, where $E = hc/\lambda$, is taken and shown in Fig. 12.

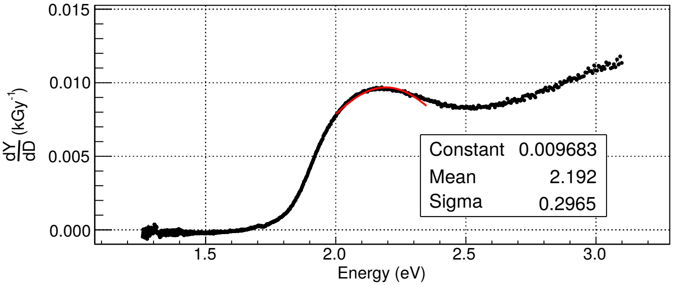

Figure 12: Identification of defect formation in quartz fiber. Data has been fitted with a Gaussian function centered around Mean $= E = 2.192$ eV.

The increased attenuation observed in Fig. 9(bottom) corresponds to the broad peak observed in Fig. 12. A Gaussian function is fitted to the data (red line in Fig. 12) and found to be centered around $E = 2.192$ eV. This is consistent with the Non-Bridging Oxygen Hole Center (NBOHC) formation hypothesis, as further discussed in [17].

5. Conclusions

The present study allows to identify a set of components suitable for the TIS design from an optical performance point of view.

LuAG:Ce exhibits a higher photon yield under ESS conditions than YAG:Ce and BGO, resulting in a more intense signal to the camera. Moreover, its emission spectrum in the $450 - 600$ nm range and peaking at 535 nm matches the region of lowest attenuation for PMMA and quartz fibers, ensuring minimum losses.

Quartz fibers exhibit a $\sim 20\%$ lower attenuation compared to PMMA fibers. PMMA fibers are more prone to radiation damage for large accumulated doses than quartz fibers. However, a color center formation at around 600 nm in quartz fibers can compromise the transmission efficiency in the vicinity of the LuAG:Ce emission range.

The overall transmittance of the Schneider optics assembly allows for $\sim 3\%$ higher signal compared to the custom assembly based on the aspheric condenser lenses.

6. Further considerations for the final TIS gamma camera

Several factors need to be considered for the final design of the TIS. This study focuses on the optical performance of the scintillators, fibers and camera optics.

The effect of γ-only irradiation on PMMA and quartz fibers has been assessed in Sections 3 and 4. However, neutron background will also be present within the ESS monolith. The decay of radioactive nuclides originating from the neutron activation of the scintillators generates an intrinsic signal inside the crystals which reduces the Signal-to-Noise Ratio (SNR). To limit the radiation damage to the optical fibers, it is necessary to avoid the presence of fluorinated components, usually contained in the fiber cladding. The low-Z composition of the plastic fibers may result in a larger sensitivity to neutrons than quartz fibers. The induced activation can cause yellowing and degradation of spectral transmittance.

The purpose of the ESS target monolith is to provide adequate shielding from the intense radiation fields originating from the spallation process. In order to shield against neutrons, straight openings must be avoided to limit neutron streaming out of the target monolith. PMMA fibers allow for smaller bending radii than quartz fibers. This allows for smaller clearances in the shielding design, making it easier to accommodate the TIS while reducing the chance of neutrons streaming through the target monolith.

The data relative to the spectral attenuation support the choice of the Schneider optics assembly as a fiber-to-camera coupling. Additional considerations are necessary to evaluate the image reconstruction performance. The TIS design is based on a set of 500 fibers arranged in a matrix layout to be imaged by the camera. The image collection relies on the definition of Regions Of Interest (ROIs) on the sCMOS chip. Each ROI encompasses a single fiber illuminating a multi-pixel cluster. The image reconstruction, performed as a time series of the collected photon intensities for each ROI, only relies on the integral of the photon intensity over each ROI area. In this perspective, the footprint of the matrix fiber layout needs to be compared to the diameter of the optics in order to minimize edge aberrations and losses. The diameter of the Schneider assembly, whilst suitable for the limited number of fibres used for test-rig operations, is too small to efficiently image the full-size matrix (500 bers) of the TIS onto the camera intensifier area. Further investigations on larger optics are needed to support the final choice of the camera lenses. A comparison between the options from the image reconstruction perspective should involve the integral values of the ROIs, the losses to scattering and aberration, the cross talk between adjacent ROIs and the SNR.

The coupling of the scintillators to the fibers must ensure the highest possible light collection efficiency. Studies should be carried out to evaluate the need for mechanical stabilization of the coupling by means of appropriate optical glues. Such glues should exhibit good transmission efficiency in the scintillator emission range and should not suffer from yellowing due to neutron and γ irradiation.

The ESS monolith will be kept in high vacuum conditions, therefore the selected glue must also comply with the outgassing requirements imposed for the monolith environment. An alternative solution may consist of a dry scintillator-fiber coupling, embedded in a vacuum-compliant epoxy fixing the fiber jackets to the scintillator cartridges. This option would provide vacuum tightness to the end of the fiber jackets, preventing outgassing form about 1 km (500×2 m) of fibers within the monolith.

In addition to the considerations relative to the optical components, other engineering constraints needs to be taken into account. The mechanical feasibility of the collimator block is to be assessed. The 500 narrow grooves impose stringent requirements to the tolerances of the milling process. Accurate positioning of the scintillator cartridges must be ensured to maximize the light collection in the crystals. Thermal studies are necessary to evaluate the presence and effect of temperature gradients which can lead to deformations in the collimator block.

Requirements on construction, comprising availability of materials and quality assurance, planning for commissioning and maintenance are also factors to be taken into account. The lifetime of the TIS components needs to be evaluated and compared to the maintenance plans for the ESS target station.

Economy also plays an important role in the design of the TIS. The three scintillator options considered, all supplied by Crytur, have the same cost. LuAG:Ce, being the one with the best optical performance, represents the most cost-effective option between the three. Quartz fibers are more expensive than plastic fibers. The difference in cost, however, must be weighed with the durability of the two options. The cheaper plastic fibers may require more frequent replacements than quartz fibers due to radiation damage. The long-term cost should therefore be assessed. A mix-and-match of quartz and plastic fibers may represent a cost-effective compromise. The cost of the camera optics solutions considered in this study is minor compared to the cost of scintillators and fibers. The Schneider optics assembly is about 4 times more expensive than the custom assembly. The cost of provisioning and manufacturing of the non-commercial TIS components, such as the collimator block and the scintillator cartridges needs to be estimated.

The complete evaluation of the remaining factors is left for future investigations.

References

[1] S. Peggs (Ed.), ESS Technical Design Report, European Spallation Source, 2013.

[2] N. Borghi, E. B. Klinkby, B. Lauritzen, E. Pitcher, N. Poolton, L. Zanini, Development of a target imaging system for the european spallation source, Journal of Physics: Conference Series 1021 (2018) 012020.

[3] N. Borghi, E. Klinkby, B. Lauritzen, L. Zanini, Detection efficiency of the ess target imaging system: Monte carlo simulations, 13th International

Topical Meeting on Nuclear Applications of Accelerators 2017, AccApp 2017 (2018) 468–477.

[4] M. T. Lucchini, K. Pauwels, K. Blazek, S. Ochesanu, E. Auffray, Radiation tolerance of luag:ce and yag:ce crystals under high levels of gamma- and proton-irradiation, IEEE Transactions on Nuclear Science 63 (2) (2016) 586–590. `doi:10.1109/Tns.2015.2493347`.

[5] Crytur materials, `http://www.crytur.cz/materials/`.

[6] Saint-Gobain scintillation products, `https://www.crystals.saint-gobain.com/products`.

[7] NIST Photon cross section data for single elements, compounds, or mixtures, `https://physics.nist.gov/PhysRefData/Xcom/html/xcom1.html`.

[8] A. Prasad, Understanding defect related luminescence processes in wide bandgap materials using low temperature multi-spectroscopic techniques, Ph.D. thesis (05 2017). `doi:10.13140/RG.2.2.16880.56327`.

[9] L. RSICC, *CCC-740 MCNPX 2.7.0 (C00740MNYCP08)* (2011).

[10] D. Pelowitz (Ed.), MCNPX User's Manual, Version 2.7.0, Los Alamos National Laboratory LA-CP-11-00438, April 2011.

[11] W. Wilson, et al., RSICC Computer Code Collection - CINDER 1.05 - Code system for actanide transmutation calculations, Oak Ridge National Laboratory LA-UR-07-8412, December 2007.

[12] ANDOR iStar sCMOS - Ultrafast platform for nanosecond time-resolved imaging and spectroscopy, `https://andor.oxinst.com/assets/uploads/products/andor/documents/andor-istar-scmos-specifications.pdf`.

[13] Schneider Kreuznach Mega Pixel lens for image circle 16 mm, `https://schneiderkreuznach.com/application/files/6615/0839/6567/Cinegon-1.9-10.pdf`.

[14] Thorlabs aspheric condenser lenses, `https://www.thorlabs.com/newgrouppage9.cfm?objectgroup_id=3835&pn=ACL7560U-A`.

[15] Edmund Optics aspheric condenser lens, `https://www.edmundoptics.com/p/75mm-diameter-x-50mm-flaspheric-condenser-lens/6712/`.

[16] M. Almgren, *Private communications* (2017).

[17] M. A. S. Kalceff, M. R. Phillips, Cathodoluminescence microcharacterization of the defect structure of quartz, Phys. Rev. B 52 (5) (1995) 3122–3134.

CHAPTER 5

Prototype TIS operation

In this chapter, the results obtained from the test-rig operations are presented.

The response of each channel is first calibrated, then gated acquisitions are performed. The images are reconstructed and compared to the theoretical expectations.

Measurements are performed using LuAG:Ce crystals, PMMA fibers (1 mm core diameter, not radiation resistant) and both the available optics (Chapter 4).

The results discussed in this chapter allow to confirm the test-rig imaging functionalities, supporting the feasibility of the final TIS. In particular, the gating synchronization and reproducibility over long time scales (max 20 h tested) has been confirmed.

The proposed image reconstruction steps, moreover, prove the possibility of detecting features with dimensions of the order of 1 mm.

In addition to the optics comparison discussed in Chapter 4, the Schneider and the custom optics are compared from the image formation point of view: the number of collected photons and the contrast of the reconstructed images are used as Figures of Merit (FOMs). Despite the slightly better transmittance of the Schneider lens, the custom optics coupling is better suited for the test-rig purpose. It is however important to stress that the final TIS will comprise 500 optical fibers, therefore the lens systems adopted for the presented measurements may not be suitable for the scale of the ESS instrument.

5.1 Calibration

To detect anomalies in the ESS target wheel, as well as to reconstruct the test-rig resolution target shapes, only relative calibration between the channels is required. The variation of the reconstructed signal over time provides sufficient information regarding the status of the target.

The relative calibration of the test-rig channels was achieved by a stationary measurement performed with the wheel parked in a feature-free position (uniform attenuation from aluminium without lead resolution targets), as shown in Fig. 5.1.

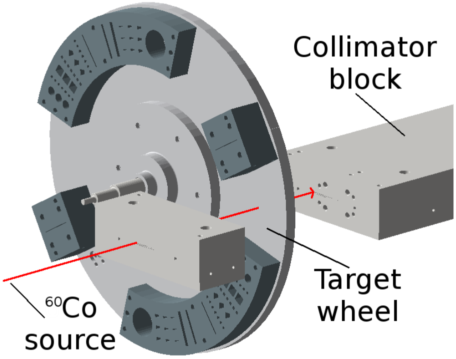

Figure 5.1: Representation of the calibration setup: the test-rig target wheel is parked in a feature-free position. The ^{60}Co source is used to provide a uniform illumination of the collimator grooves.

The measurement was repeated over time: 5000 repetitions with 0.5 s gating (total time 2500 s) and 20 repetitions with 25 s gating and 50 accumulations on chip per repetition (total time 25000 s).

Results for each fiber were averaged over the repetitions. The averaged response for the 20 fibers was normalized to the minimum value to reduce the error. Fig. 5.2 shows the uncalibrated (left) and calibrated (right) data. Fig. 5.2 is relative to the calibration with long integration times using the small Schneider camera optics. The remaining cases, covering the short integration time and the larger optics assembly, are treated in the same way. A summary of the calibration factors is presented in Tab. 5.1.

5.2 Principles of TIS image reconstruction

The TIS, as well as the test-rig, consist of a 1D array of scintillators extending along the radial direction of the rotating targets, as shown in Fig. 5.3(a). During a single gate, all the optical fibers (20 for the test-rig, 500 for the TIS) are imaged at once. The fibers are arranged in a square matrix fixed in front of the camera optics. The schematic representation of the resulting frame is shown in Fig. 5.4(b).

The two rows of collimator grooves are separated by a 1 mm septum; at any given time, they are therefore viewing a different part of the wheel. Regardless of the gating scheme, the same portion of wheel is imaged by channels 2, 4 and 6 (Fig. 5.3(a)) after a delay $\Delta t_f(r)$, defined by Eq. 5.1.

$$\Delta t_f(r) = \frac{2\ \mathrm{mm}}{v(r)} \qquad v(r) = \frac{2\pi}{T} r \tag{5.1}$$

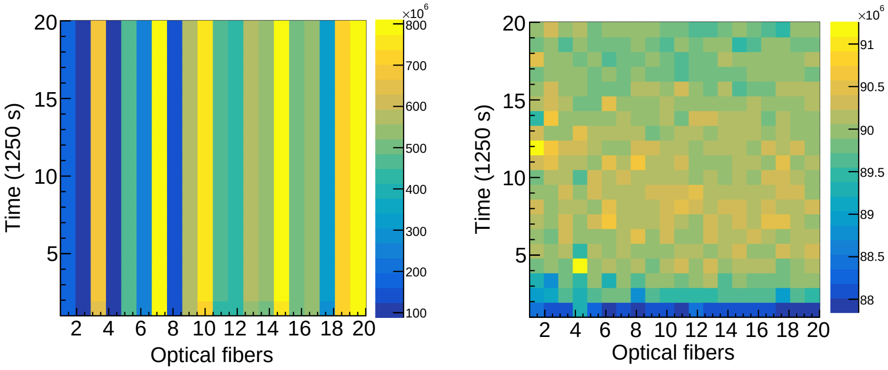

Figure 5.2: Calibration of test-rig channels: before (left) and after (right) calibration. Acquisition of raw data was performed with long integration times and with the Schneider optics assembly. Resulting calibration factors are listed in the first column of Tab. 5.1.

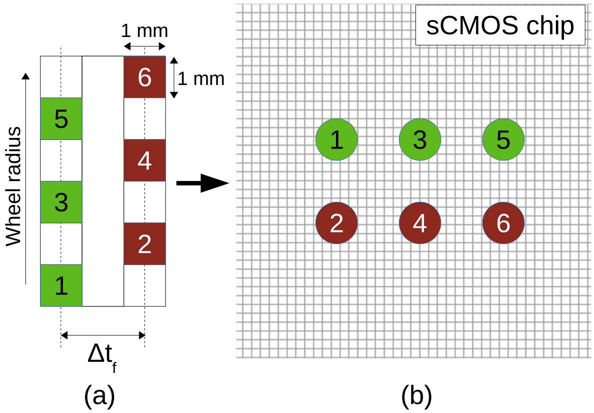

Figure 5.3: Schematic representation of the correspondence between the collimator grooves (a) and the layout on the I-sCMOS chip (b). Distance between the two rows of grooves is 2 mm and, depending on the wheel rotation speed, it corresponds to a $\Delta t_f(r)$ defined by Eq. 5.1.

Table 5.1: Calibration coefficients for test-rig. For each fiber-camera coupling optics, factors for the long and short integration times are given.

	Schneider optics		**Custom optics**	
Fiber	**Long int. time**	**Short int. time**	**Long int. time**	**Short int. time**
1	1.912	1.628	1.389	1.404
2	1.000	1.210	1.140	1.144
3	7.481	7.390	3.696	3.971
4	1.163	1.000	1.000	1.000
5	5.119	4.718	2.557	2.671
6	2.814	2.557	1.964	2.017
7	8.790	8.292	3.968	4.282
8	1.758	1.568	1.350	1.379
9	6.416	6.352	3.707	3.983
10	8.371	8.272	4.763	5.162
11	5.081	4.742	3.051	3.239
12	4.733	4.535	2.842	2.986
13	6.312	5.923	3.605	3.880
14	5.837	5.739	3.269	3.507
15	8.664	8.374	3.931	4.219
16	5.502	5.286	3.261	3.485
17	6.147	5.953	3.349	3.581
18	3.426	3.201	2.179	2.238
19	7.985	7.802	4.454	4.686
20	8.963	9.078	4.553	4.928

where r is the radial distance from the target's center and T is the rotation period.

For a given gate width G_W, one frame spans an arc whose length $l_f(r)$ depends on the radial distance r (Eq. 5.2).

$$l_f(r) = v(r)G_W \tag{5.2}$$

As an example, Fig. 5.4 shows a square feature (light blue area) to be imaged. The radial extent of the feature allows to instate the approximation $l_f(r) \approx l_f$. The gate width G_W is such that $l_f = 1$ mm and successive gates are delayed exactly by G_W, so no frames are overlapping. The side of the square feature is exactly $4l_f$.

The feature's edge imaged by channels 1 and 3 in Frame 1 (Fig. 5.4(a)) reaches channels 2 and 4 only in Frame 3 (Fig. 5.4(c)). The full imaging of the feature requires a total of 6 frames (Fig. 5.5(a)) and, in order to reconstruct the true shape of the feature, the delayed channels 2 and 4 must be translated by a number

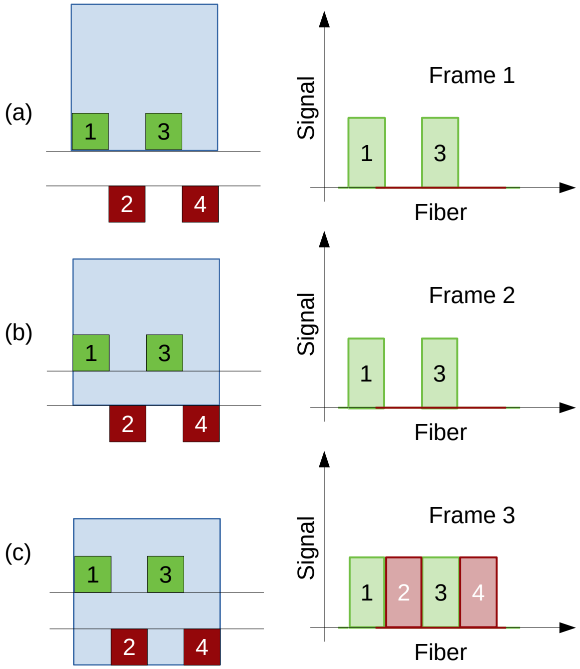

Figure 5.4: Steps of the data acquisition process. A feature (light blue area) moves with respect to the fixed collimator. The entire crystal/fiber array is imaged at each frame (a), (b) and (c). Due to the separation of the two collimator rows, the signal from half of the fibers is delayed. The offset in the number of frames is given by Eq. 5.3.

of frames Δframes defined by Eq. 5.3, where the radial dependence has been restored.

$$\Delta\text{frames}(r) = \frac{2\ \text{mm}}{l_f(r)} \tag{5.3}$$

In the example presented, $\Delta\text{frames}(r) \approx \Delta\text{frames} = 2$. As shown in Fig. 5.5(b), after translating channels 2 and 4 by $\Delta\text{frames} = 2$, the shape of the square feature is reconstructed.

Under ESS conditions, if the full resolution gating scheme is applied, $G_W = 330\ \mu\text{s}$. On the wheel's edge, $\Delta\text{frames}(r = 1.25\ \text{m}) = 2$, whereas at the inner TIS end $\Delta\text{frames}(r = 0.75\ \text{m}) \simeq 3$.

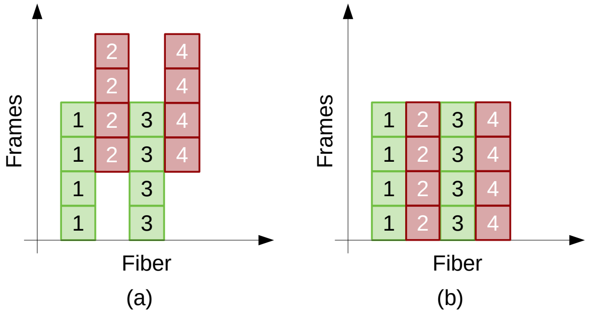

Figure 5.5: Alignment of offset images to reconstruct shapes. The result of the acquisition process shown in Fig. 5.4 is presented in (a). After correcting for the Δframes, the reconstructed image of the square feature is obtained (b).

5.2.1 Overlapping frames

The underlying assumption of the case presented in Fig. 5.4 is that the edges of the feature are perfectly synchronized with the camera gating. This assumption cannot be generalized to the entire wheel geometry. As shown in Fig. 5.6, a discontinuity from a low-signal to a high-signal region can fall exactly between two consecutive frames (Fig. 5.6(a)) or arbitrarily between two frames (Fig. 5.6(b)) up to the point where it reaches exactly the edge of the successive frame (Fig. 5.6(c)).

Ideally, the transition from low to high signal can be used to achieve sub-frame spatial resolutions. However, this capability is limited by noise fluctuations and by the gating-rotation synchronization. Uncertainties in the repeatability of the gating are represented by the gray area around the discontinuity in Fig. 5.6(b).

5.2.2 Image distortion

The layout of the test-rig resolution target is shown in Fig. 5.7(a). In the target's reference, each point is identified with $I(r_i, \theta_i)$, where $r_P \leq r_i \leq r_Q$ and $\theta_P \leq \theta_i \leq \theta_S$ are the boundaries in the radial and azimuthal directions, respectively. Any shape $S(r, \theta)$ on the resolution target is transformed into a shape $S'(x, y)$, where x and y represent point coordinates in the reconstructed image reference, according to Eq. 5.4.

$$\begin{cases} x = r \\ y = r\theta \end{cases} \tag{5.4}$$

As shown in Fig. 5.7(b), the reconstructed image appears distorted with respect to the original target shape due to the stretching of the arc into a rectangular block.

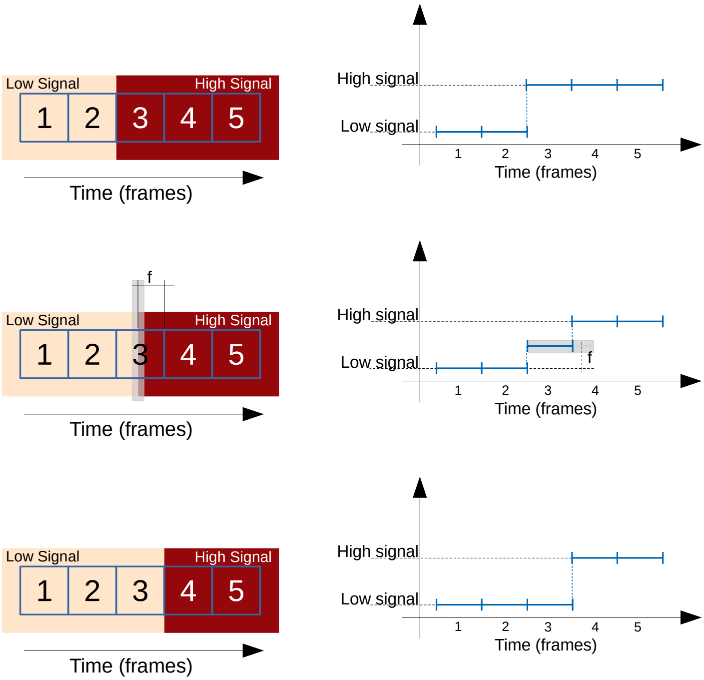

Figure 5.6: Intra-frame signal transition. An edge on the imaged target can fall exactly between two frames (top), resulting in a sharp signal increase from one frame to the following. Otherwise, the edge can be located arbitrarily in between two frames, resulting in an intermediate-strength signal f, until the point where it coincides with the successive frame change (bottom).

5.3 Test-rig images

In the following sections, data from the test-rig are presented. The setup was operated in its minimal configuration, with 20 channels (20 crystals + 20 optical fibers) spanning 2 cm in the radial direction and matching the extent of the ^{60}Co source.

An IR sensor was used as the trigger source. A reflective tag placed on the wheel edge (Fig. 5.8) provided a TTL signal once per wheel revolution. The I-sCMOS camera was directly programmed to trigger on the TTL signal and to acquire images based on specific sequences. For all the cases presented, the wheel rotation speed was kept constant with a rotation period $T = 4.26$ s.

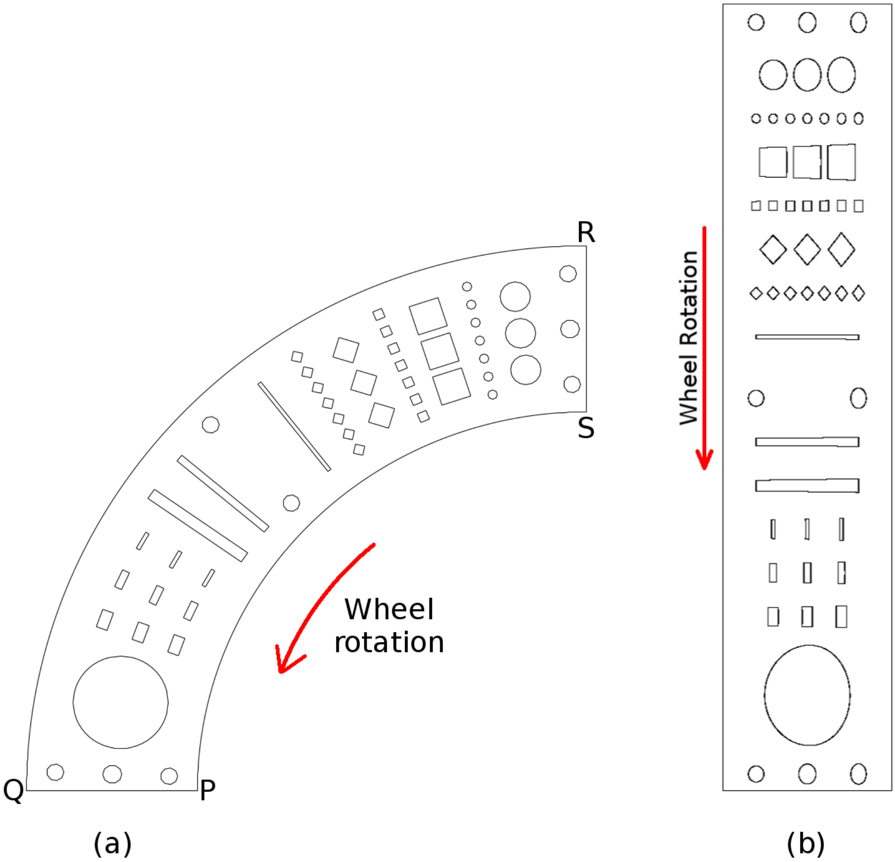

Figure 5.7: Test-rig resolution target: (a) as mounted on the wheel support; (b) as expected after image reconstruction. The stretching is calculated according to Eq. 5.4.

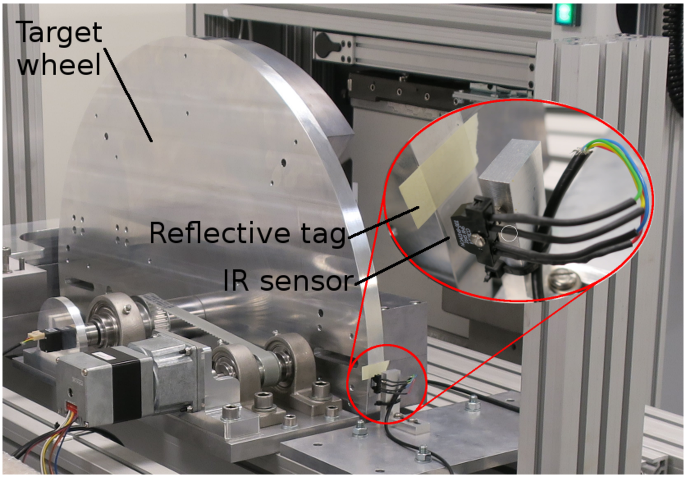

Figure 5.8: Test-rig target assembly with a detail (insert) of the IR trigger source and the reflective tag on the wheel edge.

5.3.1 Full resolution imaging

The TIS is expected to provide 1 mm spatial resolution. Under the test-rig conditions, this corresponds to a gate width $G_W = 2.240$ ms calculated on the wheel edge ($r = 30$ cm). The IR sensor trigger is defines the azimuthal $\theta = 0°$ position. With respect to this reference, the first resolution target is located at $\theta = 45°$. The camera was programmed with a gate delay $G_D = 500$ ms, corresponding to the time between the trigger and the first image ($\Delta\theta_{G_D} = 45°$). The gate step $G_S = 2.240$ ms was chosen to achieve the full azimuthal coverage. To ensure high statistics, each frame consists of several successive accumulations of the same wheel segment. The acquisition time for a single frame is $n_{\mathrm{acc}} G_W = 60 \cdot 2.240 \text{ ms} = 134.4$ ms. The total number of frames $n_{\mathrm{frames}} = 135$ results in a total imaging time $T_{\mathrm{total}} = n_{\mathrm{frames}} n_{\mathrm{acc}} T = 34506 \text{ s} \approx 10$ h.

The measurement was repeated for the two available fiber-camera coupling optics, the Schneider and the custom assemblies. The resulting images, corrected according to Eq. 5.3, are shown in Fig. 5.9(a) and Fig. 5.9(b), respectively. With the same acquisition settings, a successive portion of the wheel was imaged, as shown in Fig. 5.10.

5.3.2 High statistics imaging

A test with the custom optics was carried out with an increased number of accumulations per frame (100 instead of 60). The camera gating settings were the following: gate width $G_W = 2.240$ ms, gate step $G_S = 2.240$ ms and gate delay

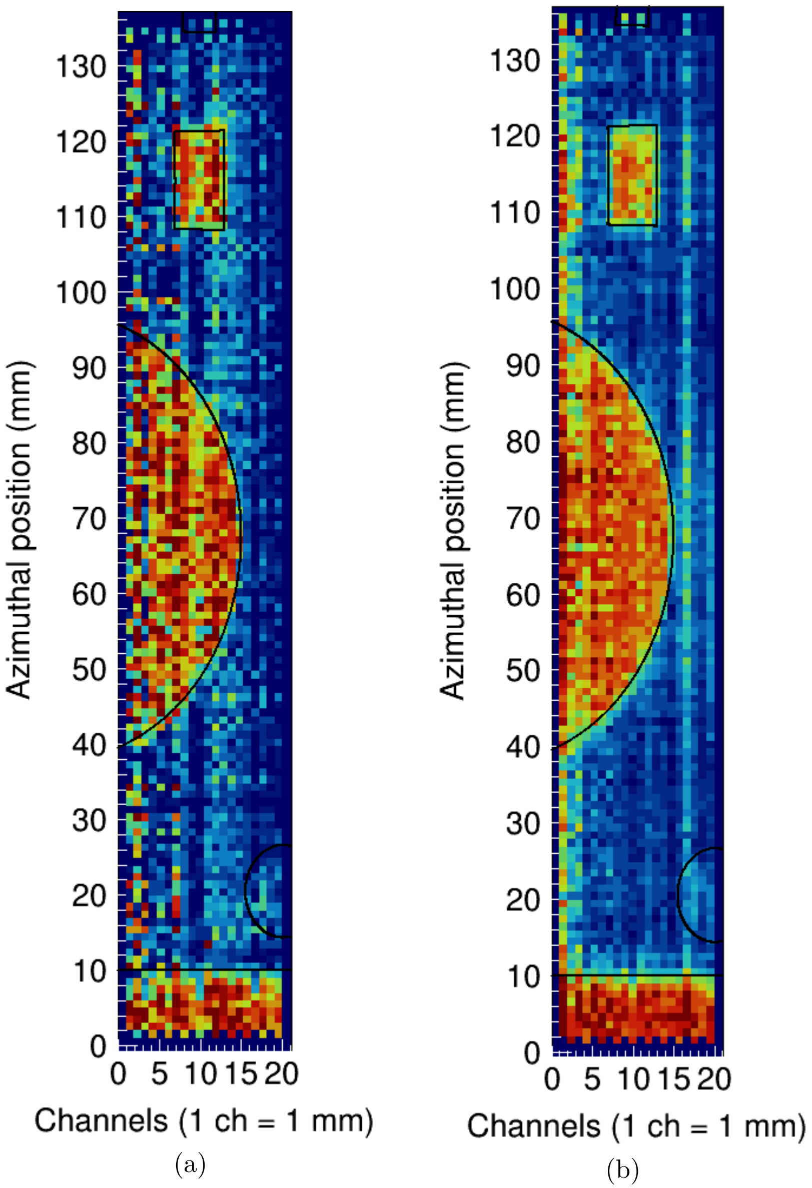

(a) (b)

Figure 5.9: Reconstructed image at full resolution from $\theta = 45°$. The length of the imaged arc, calculated on the edge of the wheel, is ≈ 13.5 cm, corresponding to a $\Delta\theta = 25°$. Results for the two optics are shown: (a) Schneider, (b) custom. Black contours indicate the reconstructed shapes, according to Eq. 5.4 and to Fig. 5.7.

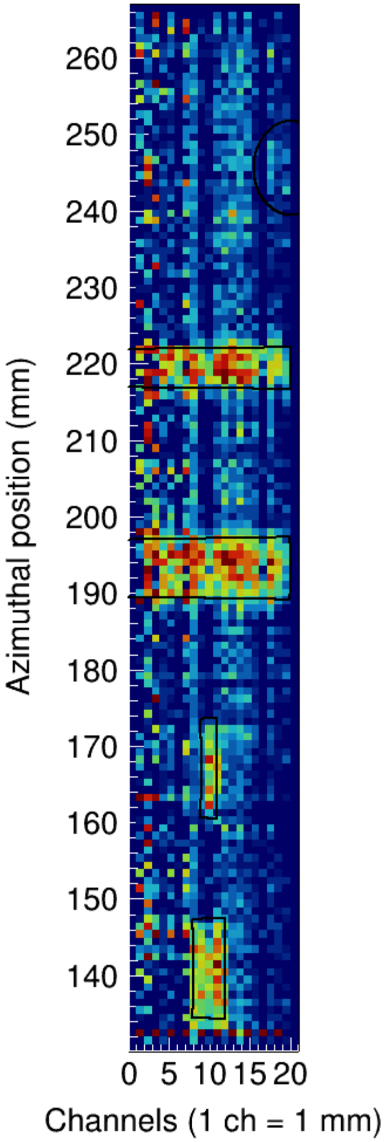

Figure 5.10: Reconstructed image at full resolution from $\theta = 70°$, with a $\Delta\theta = 25°$. Results for the Schneider optics are shown. Black contours indicate the reconstructed shapes, according to Eq. 5.4 and to Fig. 5.7.

$G_D = 500$ ms (image collection starts at $\theta = 95°$). The resulting image is shown in Fig. 5.11

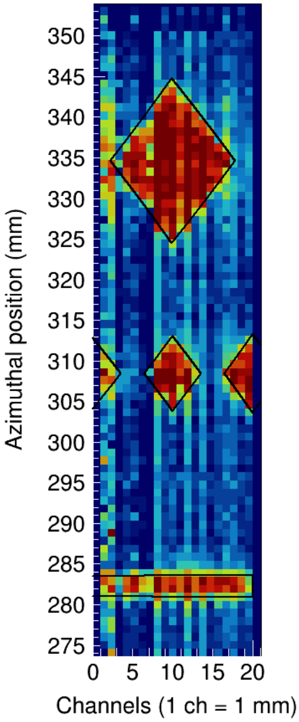

Figure 5.11: Full resolution image from $\theta = 95°$ to $\theta = 110°$. Higher statistics is accumulated for this image (100 on-chip accumulations instead of 60). Black contours indicate the reconstructed shapes, according to Eq. 5.4 and to Fig. 5.7. The custom optics was used for this test.

5.3.3 Half resolution imaging

The TIS operation allows for two gating schemes: a full-resolution sequence and a more coarse gating, providing a less accurate spatial resolution.

A test with half the spatial resolution (2 mm instead of 1 mm) was performed to investigate the imaging capabilities of the system. The 2 mm spatial resolution, defined on the wheel outer edge, corresponds to $G_W = 4.480$ ms and $G_S = 4.480$ ms; a different section of the wheel was imaged, starting from $\theta = 55°$, corresponding to $G_D = 615$ ms. For the coarse resolution test, $n_{\text{acc}} = 500$ and $n_{\text{frames}} = 34$, resulting in $T_{\text{total}} = n_{\text{frames}} n_{\text{acc}} T = 72420 \text{ s} \approx 20$ h.

The two optics have been tested and results are shown for the Schneider lens and for the custom assembly in Fig. 5.12(a) and Fig. 5.12(b), respectively.

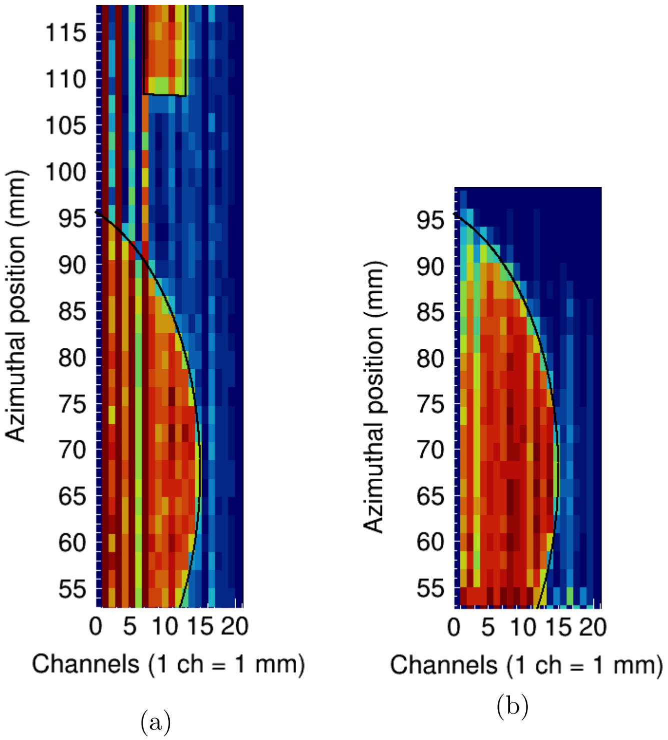

(a)

(b)

Figure 5.12: Half resolution image, 2 mm instead 1 mm, obtained for the two optics: (a) Schneider, (b) custom. For this acquisition, $\theta = 55°$, $\Delta\theta = 13°$ and $n_{\text{acc}} = 500$.

5.4 Optics performance

To compare the performance of the two fiber-camera coupling optics, two observables are taken into account: the intensity of the collected light and the distribution of the pixel intensities.

The fiber holder used for the test-rig arranges the fibers in a 19×19 mm^2 matrix that needs to be imaged onto a 13×13 mm^2 chip area. The diameter of the Schneider assembly, 30 mm is comparable to the size of the matrix holder, as shown in Fig. 5.13. This introduces losses and aberrations due to the proximity of the matrix edges to the outer edge of the lens. The custom optics, with larger diameter lenses (75 mm) allows for reduced off-axis distortions.

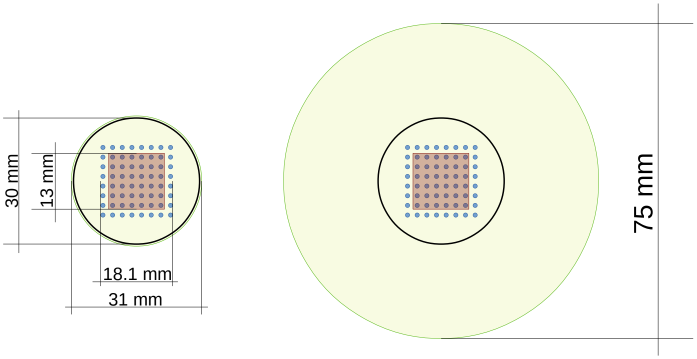

(a) (b)

Figure 5.13: Fiber-camera adapter (the black circle represents the adapter diameter and the matrix of blue circles represents the layout of max. 64 fibers in the holder) dimensions compared to sCMOS chip (dark-red area) and to the two different optics (light-green circular areas): (a) Schneider optics; (b) custom optics.

In addition, as shown in Fig. 5.14, the chip area illuminated by the fiber matrix is much smaller for the Schneider optics (Fig. 5.14(a)) than for the custom lenses (Fig. 5.14(b)).

In Fig. 5.15, obtained from Fig. 5.9 by selecting the same channel from both the images, the signal from one scintillator/fiber is plotted as a function of time. The larger illuminated area on the chip allows for more intense signals, hence for an improved Signal-to-Noise Ratio (SNR).

In Fig. 5.16, the distributions of pixel intensities for the two optics are shown (Schneider optics on the left, custom optics on the right). The distributions are calculated from data in Fig. 5.9. The two distributions exhibit a clear bi-modal shape. The peaks at lower intensities ($\mu_{\mathrm{S}_1} = 2.4 \times 10^3$ and $\mu_{\mathrm{C}_1} = 4.1 \times 10^4$ for Schneider and custom optics, respectively) represent the pixels of Fig. 5.9 corresponding to the Pb target (higher γ attenuation). The peaks at higher intensities ($\mu_{\mathrm{S}_2} = 8.9 \times 10^3$ and $\mu_{\mathrm{C}_2} = 1.3 \times 10^5$ for Schneider and custom optics, respectively) represent the pixels corresponding to the Al parts (lower γ attenuation).

The contrast of the reconstructed images (Fig. 5.9) is important to allow for shape discrimination. The separation $\Delta = \mu_2 - \mu_1$ between the high and low intensity peaks is a good measure of the contrast of the image. The higher intensities obtained with the custom optics result in a separation $\Delta = 8.8 \times 10^4 > \sigma_{\mathrm{C}_1} + \sigma_{\mathrm{C}_2} = 3 \times 10^4$. The separation for the Schneider optics is only $\Delta = 6.5 \times 10^4 \simeq \sigma_{\mathrm{C}_1} + \sigma_{\mathrm{C}_2} = 5 \times 10^4$. The standard deviations σ_{S} and σ_{C} for the various peaks are a measure of the fluctuations of the measured signals. If the

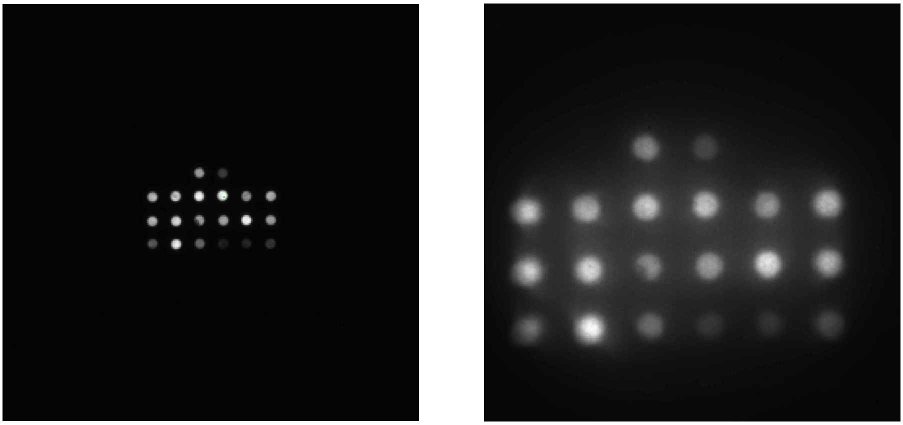

(a) (b)

Figure 5.14: Sample frame from I-sCMOS camera showing the fiber layout on the camera chip. The square area is a 2048 × 2048 pixel surface, with 8 × 8 binning, resulting in 1 macro-pixel encompassing 64 6.5 μm pixels on the sCMOS chip. The bright circles correspond to the matrix layout of the 20 optical fibers, as anticipated in Fig. 5.3; in (a), the fiber matrix is imaged with the Schneider optics, whereas in (b) the custom assembly is used.

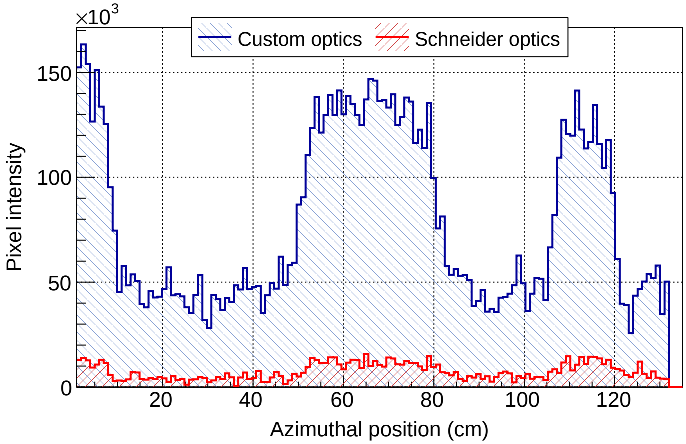

Figure 5.15: Signal from a single test-rig fiber as a function of time, hence of azimuthal position. The comparison between the two optics is presented.

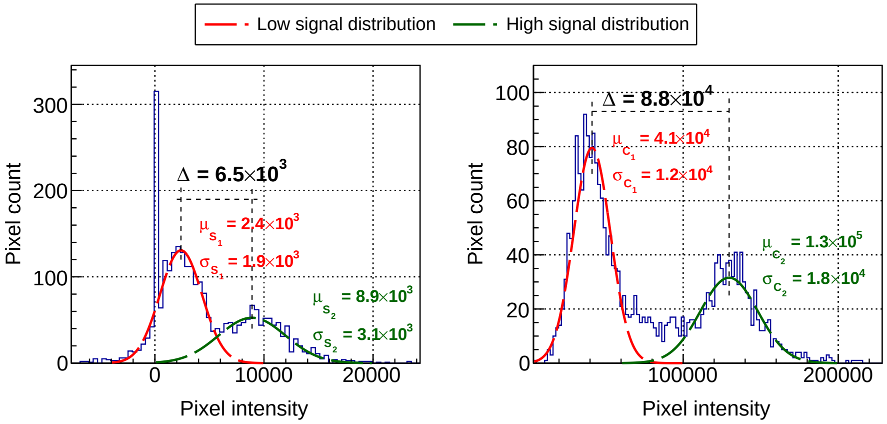

Figure 5.16: Pixel intensity distribution for the Schneider optics (left) and for the custom optics (right). The mean values of the low (red) and high (green) signal intensities are calculated with a Gaussian fit. The peak separation $\Delta = \mu_2 - \mu_1$ is compared to the fluctuations σ_1 and σ_2 around the mean values.

peak separation is comparable to the fluctuations, i.e. $\Delta \simeq \sigma_1 + \sigma_2$, as for the Schneider lens, the detection of high signal regions, especially the smaller ones, is less efficient.

In addition to the smaller SNR, the pixel distribution for the Schneider optics is also characterized by a spike at zero intensity with a tail extending to negative values. This behaviour results from the measured signals being too weak to overcome adequately the dark background, which was subtracted prior to calibration. This observation further supports the choice of the larger optics design.

5.5 Issues with calibration

The calibration procedure described in Sec. 5.1 is defined so that the signal $c_i(t_n)$ per channel i as a function of time t_n is (Eq. 5.5):

$$c_i(t_n) = \frac{f_i(t_n) - b_i}{\epsilon_i} \tag{5.5}$$

where $f_i(t_n)$ is the raw value of the i-th pixel at time t_n, b_i the dark background to be subtracted from the i-th channel and ϵ_i the i-th calibration factor (Tab. 5.1).

This definition implies that b_i and ϵ_i are constant over time and that the calibration can only be performed once. However, the reconstructed images in Fig. 5.11 and Fig. 5.12 are characterized by a striping effect affecting the signal intensity over the entire measurement.

This channel-to-channel inconsistency, visible both in regions of high signal as well as in regions of low signal, suggests a drift in the calibration coefficients ϵ_i and/or in the dark background estimation b_i can take place.

Calibrations should therefore be carried out periodically to provide uniform response from the TIS. Similarly to what was discussed in Section 5.1, calibration should be carried out in correspondence of target portions where a uniform response for all the channels is expected.

A FOM function G can be defined as follows:

$$G = \sum_i \sum_n \left(c_i\left(t_n\right) - \alpha\right)^2 \tag{5.6}$$

where α is a constant value. If calibration is successful, the function G, which is a measure of the distance from α, should be minimized. An *a priori* solution $S = \{\overline{b_i}, \overline{\epsilon_i}, \overline{\alpha}\}$ can be found by imposing $\frac{\partial G}{\partial b_i} = \frac{\partial G}{\partial \epsilon_i} = \frac{\partial G}{\partial \alpha} = 0$. The high dimensionality of the resulting system, though, requires the use of numerical solvers which strongly depend on the choice of initial conditions.

5.6 Considerations on anomaly detection

The results presented in this chapter show that the desired 1 mm spatial resolution can be achieved by the instrument.

The full resolution gating mode, however, is very time consuming due to the short integration times per exposure. It is, therefore, not recommended to use the full resolution mode for normal operations. The coarse resolution gating, however, only provides 1 mm resolution along the radial coordinate, due to the collimator geometry.

Anomaly detection in these conditions cannot rely on morphological image processing to recognize known (and isolate unknown) features on the reconstructed images. Moreover, being the radiation fields position dependent, the damage to the components is not uniform along the radial axis. This can lead to non-uniform efficiency degradation; localized variations in the signal need to be investigated to prevent artifacts from being classified as target failure points.

Analysis of the time series is an effective approach. Bayesian techniques or machine learning algorithms could be implemented to improve detection efficiency based on previous measurements.

CHAPTER 6

Implementation at the ESS

The DTU test-rig is a working prototype of the TIS proposed for the ESS.

It allowed to test the core functionalities of the system and provides flexibility to carry out systematic optimization tests for each of the main TIS components, both hardware and software.

However, the scale and the requirements of the final TIS are extremely challenging and the development of the larger instrument is not straightforward. Some of the experiments performed will need to be repeated more extensively and some ESS-specific tests will need to be conducted.

In this chapter, the attention is focused on the recommendations for each individual components, based on the experience gained with the test-rig development.

6.1 Collimator

The collimator block for the test-rig is 2 m long and is laid out horizontally. The TIS collimator will be mounted vertically, attached to the TMP support structure and will be 2.85 m long. This introduces several criticalities:

- the TMP is equipped with cooling loops to maintain a constant temperature. However, temperature gradients in either the radial or the azimuthal directions can affect the straightness of the collimator block. The collimator grooves are 1×1 mm^2 in cross-section and a deformation of 500 μm can reduce the transmitted gamma flux by 50%. The possibility to perform thermal stress tests has been included in the test-rig;

- the large number of collimator grooves may present issues with the high vacuum compliance. Venting holes along the collimator body can mitigate the issue of outgassing;

- from the shielding point of view, the presence of 500 straight channels departing from the target's surface need to be analyzed to assess the effectiveness of the monolith shielding against neutrons escaping from the target;

- the type of steel used for the test-rig was chosen for its mechanical stability. The material for the final TIS collimator must be subject to investigations to assess its compliance with the outgassing and the water release requirements within the target monolith.

6.2 Scintillators

6.2.1 Scintillator crystals

The investigations carried out in Paper 3 identified LuAG:Ce as the most cost-effective option between the three scintillators compared. Good optical properties in addition to its radiation resistance support LuAG:Ce as the choice for the TIS.

Further investigations, however, are recommended to assess the following properties:

- the efficiency of the scintillation process is temperature dependent [87]. The requirements imposed on the maximum temperature at the crystal position (z = 2.85 m above the target wheel) limit the achievable temperature to 40 °C. A thorough study of LuAG:Ce's performance as a function of temperature has not been conducted and is recommended to quantify the signal losses in case higher temperatures are reached. Collective reduction of the scintillators' photon yield can lower the SNR and impair the overall TIS performance;

- a preliminary test was carried out at DTU to investigate the auto-induced luminescence due to the decay of radioactive isotopes formed during neutron irradiation. Crystals were exposed for about 8 hours to a fast neutron spectrum (flux $\phi \approx 10^8$ n/cm^2/s). After the minimum allowed cooling time, samples were measured with the Horiba spectrometer (as discussed in Paper 3) to evaluate color center formation and/or self-induced luminescence. No effect was observed. Irradiations with different neutron spectra and fluxes are recommended to provide a better evaluation of the LuAG:Ce behaviour;

- temperature and radiation induced damages should be evaluated to estimate the expected crystal lifetime. The maintenance schedule of the TIS components embedded in the TMP can be planned accordingly. Components should be designed to remain in operation for at least one year. However, the crystals located close to the target shaft, i.e. the first 150 channels, would not be accessible before five years. Accessing these scintillators implies removing the target drive unit and this maintenance operation is only carried out during target replacements. The possibility of yearly replacements of only 350 crystals should be considered to ensure continuous monitoring with the TIS.

These considerations regarding the expected target lifetime and maintenance windows intervals are only based on the ESS design assumption of a 5 year target lifetime. However, the ESS will not be operated at full power for several years after its first commissioning, so this may extend the first deadline for target replacement, unless severe damage occurs forcing earlier intervention.

6.2.2 Scintillator cartridges

As discussed in Section 4.1.3, crystals are assembled in groups of 10 in cartridges. For the test-rig setup, PEEK was chosen as the construction material for its strength and temperature resistance.

The cartridge assembly procedure, involving gluing of crystals and fibers, is subject to large quality fluctuations. The crystal-fiber alignment and connection are crucial parameters to be controlled, as they strongly affect the signal strength.

The gluing process must provide: i) mechanical strength to ensure a stable and durable connection, ii) temperature and vacuum resistance and iii) good radiation resistance, to prevent embrittlement or darkening, which can potentially affect the light collection efficiency of the fibers.

In particular, the prototype construction of the scintillator cartridges allowed to identify the following criticalities:

- fibers must be laid out in two layers to accommodate all 10 cables. The lower layer, however, is subject to a tight curve from the crystal plane to the cartridge bed. The choice of fiber material (quartz or PMMA) impacts on the minimum allowed bending radius. In all cases, a strain relief needs to be fitted to prevent damage from the sharp edges (Fig. 4.5(b)); this is particularly important in case metal cartridges are designed for the final system, since any damage to the exposed fiber core can result in large light losses and, in the worst cases, in the complete severing of the optical fiber;
- the gluing process must be made reproducible in time and Quality Assurance (QA) and Quality Control (QC) procedures must be instated for maintenance purposes. Critical points are:
    i. the crystal-fiber joint, as the amount of glue and the alignment stability affect the light collection. The large signal variations from fiber to fiber visible in Fig. 5.2 are, among other factors, strongly related to fluctuations in the gluing quality;

ii. the fiber-cartridge gluing. The glue curing time is important to ensure good fiber alignment. Long curing times require high stability of the assembly support structure. Also, a vacuum-compliant glue is required to fulfill the ESS requirements on this matter. For the test instrument, transparent glue has been adopted to allow visual quality inspections. Black, light-tight and radiation resistant epoxies are however recommended for the final TIS, provided that a standardized assembly procedure for the cartridges is developed.

6.2.3 Cartridge holder

The cartridge holder must ensure the best alignment of the crystals to the collimator grooves. Moreover, depending on the material used, it can provide various levels of shielding against gamma and neutron radiation. This would result in a smaller background from the crystals.

The final design should take the following into consideration:

- the holder material, aluminium in the test-rig, must provide maximum mechanical stability to ensure the correct alignment of the cartridges;
- unlike the test-rig, where the holder is freely accessible, the final TIS will be embedded into the TMP. This requires remote handling for commissioning and maintenance. Fixing screws to hold the cartridges in position will not be a viable solution, thus requiring other insertion and alignment solutions to be designed;
- the shielding capabilities and the neutron activation of the cartridge holder have an impact on the background to the camera as well as on the handling during maintenance.

6.3 Optical fibers

For the optical fibers of the final TIS, the following considerations must be taken into account:

- in Paper 3, the effect of γ-only irradiation on optical fibers was investigated. The fibers used for the final TIS, however, will be subject to a mixed γ and neutron radiation field. Due to their location in the target monolith, fibers will likely be exposed to a neutron spectrum with thermal components. This may induce higher levels of activation in the plastic fibers due to the low-Z material. It has been shown that quartz fibers are less prone to radiation damage. The presence of fluorinated components in the fiber cladding must be avoided to improve the fibers radiation resistance;

- the ESS target monolith serves the purpose of providing shielding from the intense radiation fields originating from the spallation process. To prevent neutron streaming out of the monolith, straight openings must be avoided. PMMA fibers are more flexible than quartz fibers and allow for smaller bending radii than quartz fibers. This allows to minimize the clearances in the shielding design, facilitating the TIS accommodation;

- the vacuum requirements imposed for the target monolith environment ($0.1 - 0.01$ Pa during operation) must be accounted for also with respect to the optical fibers. In order to couple the fibers to the scintillator crystals, the fiber core has to be exposed. The cut jacket must be sealed to prevent any air pocket along the fiber cable to be released into the monolith atmosphere. Moreover, the jacket material itself must be capable of withstanding the high vacuum condition;

- for the test-rig setup, fiber were split in two points and connected by means of dry-coupled SMA connectors. To comply with the vacuum requirements, sealed connectors should be adopted. Moreover, the transmission efficiency of each connector can be improved if the interface to air is removed by means of couplings capable of matching the refractive indices;

- the very different response to radiation of plastic and quartz fibers allows for further considerations regarding the economy of the final TIS. The present proposal comprises 500 fibers, each ~ 20 m long, for a total of about 10 km. The low radiation resistance of PMMA fibers may result in frequent replacements of the damaged fibers. On the other hand, the more resistant quartz fibers are also more expensive. A quartz-only solution, therefore, may have a good performance with a very high cost. A cheaper plastic-only design, instead, may result in frequent maintenance and increased costs. A compromise and cost-effective solution can be envisaged consisting of a combination of radiation resistant quartz fibers in the initial part of the cables, and plastic fibers for the remaining length.

6.4 Camera optics

The two optics used for the test-rig measurements provide insight into the design requirements for the final TIS optics. As discussed, in Chapter 5, the larger optics allows for better light collection. This results in an improved SNR, and in a sharper contrast between high and low signals. However, none of the two options is suitable to accommodate the full array of 500 fibers. A new design for the camera optics and for the matrix holder, with a much higher density of fibers per cm^2 are therefore required.

The characterization of the high-speed operations described in Section 4.2 supports the suitability of the Andor iStar I-sCMOS camera for the final TIS installation.

6.5 Image reconstruction and integration with ESS controls

The image reconstructions performed in Chapter 5 showcase the full resolution capabilities of the proposed system.

However, as discussed in Paper 2, two modes of operation are envisaged; the full resolution mode, being very time consuming, should only be selected when anomalies are found. Normal operations should be carried out at coarser resolutions.

In this case, morphological image analysis is not suitable for shape identification. As discussed in Paper 2, statistical algorithms shall be implemented to analyze the time evolution of the TIS signals.

In principle, according to Eq. 5.4, the expected signal from the target wheel can always be calculated. However, variations in the system performance, especially if position dependent (e.g. different radiation fields at different radial coordinates resulting in different damage to the components), can impair the ability to compare the measured signals with the theoretical predictions.

The Bayesian approach of the Kalman filter, for instance, could provide the required time-dependent predictive capabilities. Machine learning techniques can also represent a viable choice for the detection of anomalies in signal patterns.

For the final TIS, regardless of the algorithms adopted to detect failures in the target geometry, it is fundamental to define how the instrument should be integrated in the ESS control systems. In particular, it is necessary to retrieve:

- the status of the proton beam to control the camera intensifier accordingly;
- the exact position of the target wheel to allow for repeatable measurements.

The output information that the TIS should relay to the ESS controls in case anomalies are found have not been defined at the current status of the development.

CHAPTER 7

Conclusions and outlook

The long-term objective of the Target Imaging System (TIS) project, and the Target Monitoring Plug (TMP) in general, is to equip the ESS target with a set of diagnostic tools to monitor its health condition during operation.

This PhD project covered the initial phase of the TIS development: from the basic concept, defined in collaboration with the ESS, to a working prototype built and commissioned at DTU.

Monte Carlo simulations of the irradiation environment to which the TIS will be subject indicate the feasibility of the device, from both signal and background points of view. The signal (the decay γ radiation from the activated tungsten bricks) is of sufficient intensity to be detected by the scintillators, and provide the required spatial information about the target bricks. The background at the location of the scintillators is of the same order of magnitude as the signal, ensuring the possibility to reconstruct a detailed image of the target.

The test instrument constructed represents a significant step towards the TIS development: it demonstrates the feasibility of the basic concept, the possibility to achieve high spatial resolution imaging as designed and provides a flexible test platform offering means of further detailed investigations of the final TIS design and performance.

Optical components have been identified and characterized: LuAG:Ce is indicated as a suitable scintillator material based on its light emission properties (spectrum and photon yield) and radiation resistance. The effect of neutron irradiation on LuAG:Ce requires further investigations to evaluate activation and decay phenomena which can ultimately lead to a SNR degradation.

Characterization of PMMA and quartz optical fibers has been carried out. Their transmission properties have been investigated under radiation-free conditions as well as after γ irradiation up to a total accumulated dose of 15 kGy (5 years of ESS operations correspond to 2.5 kGy). Quartz fibers proved to be more suitable for the TIS requirements for the lower attenuation (≤ 0.1 dB/m) than PMMA fibers under radiation-free conditions. Quartz fibers also exhibit a better resistance to γ irradiation than PMMA fibers. Further investigations are recommended to evaluate the effect of a mixed γ-neutron radiation field.

The camera chosen for the prototype work (Andor iStar I-sCMOS) is considered suitable for the final TIS operations. It allows 0.1 μs operations, thus fulfilling the fast-timing requirements imposed by the full-resolution imaging mode of the TIS.

The acquired images demonstrate the possibility of accurately synchronizing the camera gating to the wheel rotation in order to perform consistent imaging of the same wheel portion. This can improve the SNR, especially in the case of short integration times, where readout noise may dominate the acquired data.

Basic software controls were developed and, from them, guidelines for final TIS software can be outlined. Simple image reconstruction techniques have been implemented and the basic image distortions have been corrected.

The work carried out during this PhD provides substantial contributions to the design of the final TIS. New challenges will need to be undertaken in order to upscale the prototype instrument and fulfill all the ESS requirements.

A new collimator must be designed accounting for the constraints imposed by the ESS target monolith, such as the type of steel, the integration with the TMP or the commissioning and maintenance procedures. The coupling of the crystals to the fibers and to the collimator can take advantage of the cartridge design used for the prototype. However, a material review is required, as PEEK might not be suitable for the ESS radiation environment.

Advanced design of the optical fiber arrangement in the monolith is necessary: the 500 optical fibers required need to be routed through the monolith fulfilling the vacuum and shielding requirements while accounting for their limited flexibility. Commissioning, remote handling and maintenance are additional factors to consider.

The design of the fiber-camera coupling optics can take advantage from the specifications of the custom assembly designed for the test operations. However, a new design will be required to accommodate the entire set of 500 fibers. Factors to be accounted for include: i) numerical aperture of fibers and lenses, ii) lens magnification to ensure maximum illumination of the camera chip, iii) compact layout of the fibers in front of the lenses to maximize surface density.

Finally, the software controls used need to be re-designed to allow for the correct integration with the ESS control systems.

This PhD project has set a fundamental baseline for the TIS development and is providing a reference guideline to benchmark the forthcoming design choices. Just like the ESS, the TIS is a unique instrument in its kind. During its operation, it will provide information about the target as well as indications useful for its own development.

The positive outcome of this thesis work proved that this technology is a viable way to monitor spallation targets under demanding operating conditions. Therefore, such device could be applied not only to ESS, but also to future target stations.

Additional bibliography

[1] D. J. Hughes. *The neutron story.* Heinemann, 1959.

[2] J. E. Lynn. *The theory of neutron resonance reactions.* Oxford University Press, 1968.

[3] K. H. Beckurts and K. Wirtz. *Neutron physics.* Springer, 1964.

[4] G. F. Knoll. *Radiation Detection and Measurement; 2nd ed.* New York, NY: Wiley, 1989. URL: https://cds.cern.ch/record/113936.

[5] I. Curie and F. Joliot. “Preuves expérimentales de l’existence du neutron”. In: *Journal de Physique et le Radium* 4.1 (1933), pages 21–33. DOI: 10.1051/jphysrad:019330040102100.

[6] J. Chadwick. “Possible existence of a neutron”. In: *Nature* 129.3252 (1932), page 312. DOI: 10.1038/129312a0.

[7] K. A. Olive. “Review of Particle Physics”. In: *Chinese Physics C* 38.9 (2014). ISSN: 1674-1137. DOI: 10.1088/1674-1137/38/9/090001.

[8] D. Dubbers and M. G. Schmidt. “The neutron and its role in cosmology and particle physics”. In: *Reviews of Modern Physics* 83.4 (2011), pages 1111–1171.

[9] R. Pynn. “Neutron scattering: a primer”. In: *LAUR-95-3840* 19 (1990).

[10] J. S. Nico and W. M. Snow. “Fundamental Neutron Physics”. In: *Annu. Rev. Nucl. Part. Sci.* 55.1 (2005), pages 27–69. ISSN: 0163-8998. DOI: 10.1146/annurev.nucl.55.090704.151611.

[11] K. S. Krane. *Introductory nuclear physics.* Wiley, 1988.

[12] B. S. P. Shen. *Spallation nuclear reactions and their applications.* Dordrecht Reidel, 1976.

[13] D. Filges and F. Goldenbaum. *Handbook of Spallation Research.* Wiley, 2010. ISBN: 9783527407149. DOI: 10.1002/9783527628865.

[14] J. M. Carpenter. “Neutron production, moderation, and characterization of sources”. In: *Elements of Slow-Neutron Scattering.* Cambridge University Press, 2015.

[15] F. Mezei. “Accelerator requirements for next generation neutron sources”. In: *Nuclear Instruments and Methods in Physics Research Section A: Accelerators, Spectrometers, Detectors and Associated Equipment* 562.2 (2006), pages 553–556. ISSN: 0168-9002. DOI: 10.1016/j.nima.2006.02.007.

[16] S. Peggs, editor. *ESS Technical Design Report.* European Spallation Source, 2013.

[17] N. Watanabe. “Neutronics of pulsed spallation neutron sources”. In: *Reports on Progress in Physics* 66.3 (2003), page 339. ISSN: 0034-4885.

[18] G. S. Bauer. “Some general reflexions on ‘‘long pulse’’ neutron sources”. In: *Journal of Neutron Research* 3.4 (1996), pages 253–271. ISSN: 1023-8166. DOI: 10.1080/10238169608200199.

[19] N. Colonna, F. Gunsing, and F. Käppeler. “Neutron physics with accelerators”. In: *Progress in Particle and Nuclear Physics* 101 (2018), pages 177–203. ISSN: 0146-6410.

[20] *European Spallation Source.* https://europeanspallationsource.se/.

[21] *Neutron scattering facilities in Europe - Present status and future perspectives.* https://www.esfri.eu/sites/default/files/u4/NGL_CombinedReport_230816_Complete%20document_0209-1.pdf.

[22] *Neutrons for science and technology.* http://sine2020.eu/index.php?get_file=20170207_2ndensa-brochure_web.pdf.

[23] *Neutron users in Europe: Facility-Based Insights and Scientific Trends.* https://europeanspallationsource.se/sites/default/files/files/document/2018-06/NEUTRON%20USERS%20IN%20EUROPE%20-%20Facility-Based%20Insights%20and%20Scientific%20Trends.pdf.

[24] R. Garoby et al. “The European Spallation Source Design”. In: *Physica Scripta* 93.1 (2017), page 014001.

[25] J. M. Carpenter. “Pulsed spallation neutron sources for slow neutron scattering”. In: *Nuclear Instruments and Methods* 145.1 (1977), pages 91–113. ISSN: 0029-554x. DOI: 10.1016/0029-554X(77)90560-2.

[26] L. Zanini et al. “Design of the cold and thermal neutron moderators for the European Spallation Source”. In: *Nuclear Instruments and Methods in Physics Research Section A: Accelerators, Spectrometers, Detectors and Associated Equipment* 925 (2019), pages 33–52. ISSN: 0168-9002. DOI: 10.1016/j.nima.2019.01.003.

[27] L. Zanini. *Private communications.* 2012.

[28] D. Lyngh. *Private communications.* 2016.

[29] E. Pitcher. *Private communications.* 2016.

[30] A. Aguilar et al. “Design specification for the European Spallation Source neutron generating target element”. In: *Nuclear Instruments and Methods in Physics Research Section A: Accelerators, Spectrometers, Detectors and Associated Equipment* 856 (2017), pages 99–108. ISSN: 0168-9002.

[31] M. Magán et al. “Neutron performance analysis for ESS target proposal”. In: *Nuclear Instruments and Methods in Physics Research Section A: Accelerators, Spectrometers, Detectors and Associated Equipment* 680 (2012), pages 61–68. ISSN: 0168-9002.

[32] R. Zubler and J. Bertsch. “Cleaning of failed lead containing zircaloy-2 neutron spallation target rods with a dissolution process”. In: *Annual Meeting on Hot Laboratories and Remote Handling*. Mito, Japan, September 2017.

[33] G. S. Bauer. “Overview on spallation target design concepts and related materials issues”. In: *Journal of Nuclear Materials* 398.1 (2010), pages 19–27. ISSN: 0022-3115.

[34] J. M. Carpenter and A.G. Hins. “Experience with IPNS targets”. In: *Proc. ICANS-XII, Abingdon 1993*. Rutherfort Appleton Report 94-025, pp. T1-T11, 1994.

[35] O. Caretta, T. Davenne, and C. J. Densham. “Water erosion tests on a tantalum sample: A short communication”. In: *Journal of Nuclear Materials* 492 (2017), pages 52–55. ISSN: 0022-3115.

[36] Z. Zeng et al. “Design of imaging system for CSNS near-target beam diagnostics”. In: *Radiation Detection Technology and Methods* 2.2 (2018), page 37. ISSN: 2509-9949.

[37] W. Wagner, P. Vontobel, and Y. Dai. “Materials issues of the SINQ high-power spallation target”. In: *International Journal of Materials Research* 102.9 (2011), pages 1101–1105.

[38] M. Futakawa et al. “Cavitation erosion induced by proton beam bombarding mercury target for high-power spallation neutron sources”. In: *Experimental Thermal and Fluid Science* 57 (2014), pages 365–370. ISSN: 0894-1777.

[39] M. Teshigawara et al. “Development of JSNS target vessel diagnosis system using laser Doppler method”. In: *Journal of Nuclear Materials* 398.1 (2010), pages 238–243. ISSN: 0022-3115.

[40] M. Futakawa et al. “Development of the Hg target in the J-PARC neutron source”. In: *Nuclear Instruments and Methods in Physics Research Section A: Accelerators, Spectrometers, Detectors and Associated Equipment* 600.1 (2009), pages 18–21. ISSN: 0168-9002.

[41] J. Marian and T. L. Hoang. “Modeling fast neutron irradiation damage accumulation in tungsten”. In: *Journal of Nuclear Materials* 429.1 (2012), pages 293–297. ISSN: 0022-3115.

[42] A. Hasegawa et al. “Neutron irradiation effects on tungsten materials”. In: *Fusion Engineering and Design* 89.7 (2014), pages 1568–1572. ISSN: 0920-3796.

[43] M. Fukuda et al. “Neutron energy spectrum influence on irradiation hardening and microstructural development of tungsten”. In: *Journal of Nuclear Materials* 479 (2016), pages 249–254. ISSN: 0022-3115.

[44] X. Hu et al. “Irradiation hardening of pure tungsten exposed to neutron irradiation”. In: *Journal of Nuclear Materials* 480 (2016), pages 235–243. ISSN: 0022-3115.

[45] X. Hu et al. “Defect evolution in single crystalline tungsten following low temperature and low dose neutron irradiation”. In: *Journal of Nuclear Materials* 470 (2016), pages 278–289. ISSN: 0022-3115.

[46] A. Hasegawa et al. “Neutron irradiation effects on the microstructural development of tungsten and tungsten alloys”. In: *Journal of Nuclear Materials* 471 (2016), pages 175–183. ISSN: 0022-3115.

[47] M. Klimenkov et al. “Effect of neutron irradiation on the microstructure of tungsten”. In: *Nuclear Materials and Energy* 9 (2016), pages 480–483. ISSN: 2352-1791.

[48] B. G. Butler et al. “Mechanisms of deformation and ductility in tungsten – A review”. In: *International Journal of Refractory Metals and Hard Materials* 75 (2018), pages 248–261. ISSN: 0263-4368.

[49] L. M. Garrison, Y. Katoh, and N. A. P. K. Kumar. “Mechanical properties of single-crystal tungsten irradiated in a mixed spectrum fission reactor”. In: *Journal of Nuclear Materials* 518 (2019), pages 208–225. ISSN: 0022-3115.

[50] J. Aldazabal et al. “A comparison of the structure and mechanical properties of commercially pure tungsten rolled plates for the target of the European spallation source”. In: *International Journal of Refractory Metals and Hard Materials* 70 (2018), pages 45–55. ISSN: 0263-4368.

[51] European Spallation Source (Y. J. Lee). *ESS Internal Document (ESS-0051742) - Integrity of spallation material in the target wheel during operation and accidents.* Technical report. 2016.

[52] European Spallation Source (U. Odén). *ESS Internal Document (ESS-0059414) - Justification of Tungsten Particles Production Estimate.* Technical report. 2016.

[53] H. Ullmaier and F. Carsughi. “Radiation damage problems in high power spallation neutron sources”. In: *Nuclear Instruments and Methods in Physics Research Section B: Beam Interactions with Materials and Atoms* 101.4 (1995), pages 406–421. ISSN: 0168-583X.

[54] K. Sjögreen. *Private communications.* 2019.

[55] European Spallation Source (J. Harborn). *ESS Internal Document (ESS-0135246) - Target Monitoring System (System Description Document - Solutions).* Technical report. 2019.

[56] European Spallation Source (K. Sjögreen). *ESS Internal Document (ESS-0052060) - Accident Analysis Report 5: global bypass and local blocking of target.* Technical report. 2017.

[57] European Spallation Source (J. Harborn). *ESS Internal Document (ESS-0028465) - ESS Materials Handbook.* Technical report. 2018.

[58] Y. J. Lee. *Private communications.* 2019.

[59] European Spallation Source (J. Harborn). *ESS Internal Document (ESS-0136661) - Target Monitoring System (System Description Document - Requirements).* Technical report. 2019.

[60] T. E. Peterson and L. R. Furenlid. "SPECT detectors: the Anger Camera and beyond". In: *Physics in Medicine and Biology* 56.17 (2011), R145. ISSN: 0031-9155.

[61] A. Sessler and E. Wilson. *Engines of Discovery: A Century of Particle Accelerators (Revised and Expanded Edition).* World Scientific, 2014. DOI: 10.1080/00107514.2014.999128.

[62] J. Islamian et al. "Advances in Pinhole and Multi-Pinhole Collimators For Single Photon Emission Computed Tomography Imaging". In: *World J Nucl Med* 14.1 (2015), pages 3–9. DOI: 10.4103/1450-1147.150505.

[63] J. L. Prince and J. M. Links. *Medical Imaging Signals and Systems.* Pearson Education, 2014. ISBN: 9780132145183.

[64] LANL RSICC. *CCC-740 MCNPX 2.7.0 (C00740MNYCP08).* 2011.

[65] D. Pelowitz (Ed.) *MCNPX User's Manual, Version 2.7.0.* Los Alamos National Laboratory LA-CP-11-00438, April 2011.

[66] W.B. Wilson et al. *RSICC Computer Code Collection - CINDER 1.05 - Code system for actanide transmutation calculations.* Oak Ridge National Laboratory LA-UR-07-8412, December 2007.

[67] Sóti, Zsolt, Magill, Joseph, and Dreher, Raymond. "Karlsruhe Nuclide Chart 10th edition 2018 ". In: *EPJ Nuclear Sci. Technol.* 5 (2019), page 6. DOI: 10.1051/epjn/2019004. URL: https://doi.org/10.1051/epjn/2019004.

[68] *Brookhaven National Nuclear Data Center - NuDat 2.7.* https://www.nndc.bnl.gov/nudat2/.

[69] V. P. Singh and N. M. Badiger. "Study of mass attenuation coefficients, effective atomic numbers and electron densities of carbon steel and stainless steels". In: *Radioprotection* 48.3 (2013), pages 431–443. DOI: 10.1051/radiopro/2013067.

[70] *Tool steel 1.1730 Specifications.* https://www.meusburger.com/EN/US/products/mold-making/quality/material-grades/11730-tool-steel.

[71] J. Y. S. Page, H. W. Bonon, and V. T. Bui. “Neutron and gamma radiation effects on the viscoelastic behaviour of poly (aryl etherether ketone)”. In: Canada, 1997, page 1122.

[72] D. J. Y. S. Pagé et al. “Mixed radiation field effects from a nuclear reactor on poly(aryl ether ether ketone): A melt viscosity study”. In: *Journal of Applied Polymer Science* 86.11 (2002), pages 2713–2719.

[73] N. Poolton. *Private communications.* 2016.

[74] W. Chewpraditkul et al. “Scintillation Properties of LuAG:Ce, YAG:Ce and LYSO:Ce Crystals for Gamma-Ray Detection”. In: *IEEE Transactions on Nuclear Science* 56.6 (2009), pages 3800–3805. ISSN: 0018-9499. DOI: 10.1109/Tns.2009.2033994.

[75] W. Chewpraditkul and M. Moszynski. “Scintillation Properties of Lu3Al5O12, Lu2SiO5 and LaBr3 Crystals Activated with Cerium”. In: *Physics Procedia* 22 (2011), pages 218–226. ISSN: 1875-3892.

[76] X. Chen et al. “Influence of cerium doping concentration on the optical properties of Ce,Mg:LuAG scintillation ceramics”. In: *Journal of the European Ceramic Society* 38.9 (2018), pages 3246–3254. ISSN: 0955-2219.

[77] R. Mao, L. Zhang, and R. Zhu. “Optical and Scintillation Properties of Inorganic Scintillators in High Energy Physics”. In: *IEEE Transactions on Nuclear Science* 55.4 (2008), pages 2425–2431. ISSN: 0018-9499. DOI: 10.1109/Tns.2008.2000776.

[78] S. Diehl et al. “Characterization and Applications of New High Quality LuAG:Ce and LYSO:Ce fibers”. In: *Journal of Physics: Conference Series* 587 (2015), page 012067.

[79] Y. Kuwano et al. “Crystal growth and properties of (Lu,Y)3Al5O12”. In: *Journal of Crystal Growth* 260.1 (2004), pages 159–165. ISSN: 0022-0248.

[80] M. Moszynski et al. “Properties of the YAG:Ce scintillator”. In: *Nuclear Instruments and Methods in Physics Research Section A: Accelerators, Spectrometers, Detectors and Associated Equipment* 345.3 (1994), pages 461–467. ISSN: 0168-9002.

[81] M. V. Derdzyan et al. “Radiation hardness of LuAG:Ce and LuAG:Pr scintillator crystals”. In: *Journal of Crystal Growth* 361 (2012), pages 212–216. ISSN: 0022-0248. DOI: 10.1016/j.jcrysgro.2012.09.046.

[82] C. Dujardin et al. “LuAG:Ce fibers for high energy calorimetry”. In: *Journal of Applied Physics* 108.1 (2010), page 013510. ISSN: 0021-8979. DOI: 10.1063/1.3452358.

[83] A. M. Frelin et al. “Scintillating fiber dosimeter”. In: *IEEE Symposium Conference Record Nuclear Science 2004.* Volume 4. 2004, 2221–2225 Vol. 4. DOI: 10.1109/Nssmic.2004.1462703.

[84] M. Korzhik et al. “Timing properties of Ce-doped YAP and LuYAP scintillation crystals”. In: *Nuclear Instruments and Methods in Physics Research Section A: Accelerators, Spectrometers, Detectors and Associated Equipment* 927 (2019), pages 169–173. ISSN: 0168-9002.

[85] A. G. Petrosyan et al. “A study of radiation effects on LuAG:Ce(Pr) co-activated with Ca”. In: *Journal of Crystal Growth* 430 (2015), pages 46–51. ISSN: 0022-0248. DOI: 10.1016/j.jcrysgro.2015.08.019.

[86] Y. Zorenko et al. “Influence of thermal treatment and γ-radiation on absorption, luminescence and scintillation properties of Lu3Al5O12:Ce single crystalline films”. In: *Radiation Measurements* 42.4 (2007), pages 557–560. ISSN: 1350-4487. DOI: 10.1016/j.radmeas.2007.01.073.

[87] P. Lecoq et al. *Inorganic Scintillators for Detector Systems.* Springer-Verlag, 2006. DOI: 10.1007/3-540-27768-4.

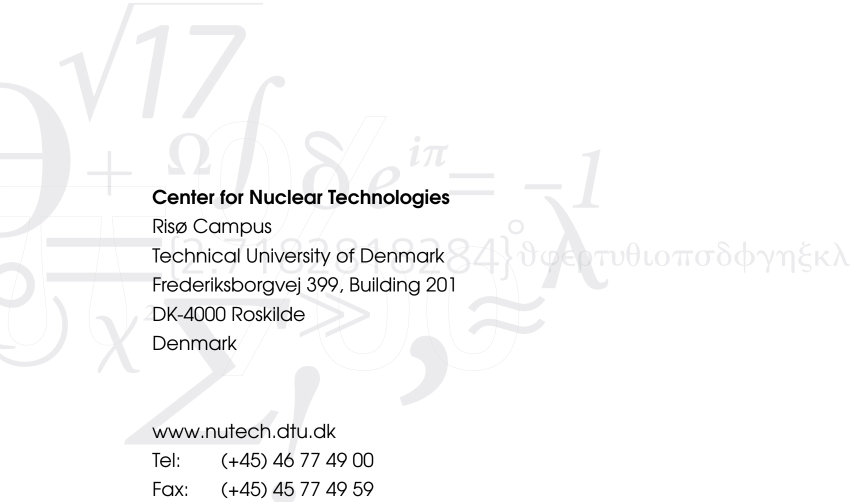

Center for Nuclear Technologies
Risø Campus
Technical University of Denmark
Frederiksborgvej 399, Building 201
DK-4000 Roskilde
Denmark

www.nutech.dtu.dk
Tel: (+45) 46 77 49 00
Fax: (+45) 45 77 49 59